

2014 | Faculty of Sciences

DOCTORAL DISSERTATION

Morphological characterization and electronic transport properties of aluminum-doped zinc-oxide films prepared by dc sputtering

Doctoral dissertation submitted to obtain the degree of doctor of
Science: Physics, to be defended by

Matthias Van Gompel

Promoter: Prof. Dr Patrick Wagner | UHasselt

Co-promoter: Prof. Dr Marlies K. Van Bael | UHasselt



D/2014/2451/35

Jury

Chair:	Prof. Dr. K. Coninx Dean Faculty of Science Universiteit Hasselt
Promotor:	Prof. Dr. P. Wagner Universiteit Hasselt
Co-promotor:	Prof. Dr. M. K. Van Bael Universiteit Hasselt
Members of the jury:	Prof. Dr. J. D'Haen Universiteit Hasselt
	Dr. P. Losada-Perez Universiteit Hasselt
	Prof. Dr. B. Partoens Universiteit Antwerpen
	Dr. J. Vanacken Katholieke Universiteit Leuven
	Prof. Dr. S. Turner Universiteit Antwerpen

Contents

Dankwoord	vii
Samenvatting	ix
Abstract	xv
I Introduction	1
1 Transparent Conductive Oxides	3
1.1 Materials and properties	3
1.1.1 History and examples	4
1.1.2 Applications	10
1.2 Physics of TCO's	12
1.2.1 The Drude model of electric conduction	14
1.2.2 Mott metal-insulator transitions	17
1.3 The ceramic material: Zinc Oxide	23
2 Thin film deposition	27
2.1 Sputter deposition	28
2.2 Chemical vapour deposition	35
2.3 Pulsed laser deposition	36

II	Methods and Materials	39
3	The sputtering reactor	41
3.1	Sputtering cathode	43
3.2	Substrate holder	45
3.3	Substrate preparation	48
3.4	Sputtering target	49
4	Electronic-, structural- and chemical characterization techniques	55
4.1	Van der Pauw setup	55
4.2	Hall setup	58
4.3	X-ray diffraction	64
4.4	Electron microscopy	66
4.5	X-ray photo electron spectroscopy	67
III	Results and discussion	69
5	Al:ZnO thin films with 2.4 % Al	71
5.1	Sample preparation	72
5.2	Structural and chemical characterization	74
5.3	Electronic characterization	76
5.4	Optical characterization	80
6	Al:ZnO thin films with 1 at% Al	81
6.1	Why dope with 1 at.% Al?	81
6.1.1	Deposition in Ar/O ₂ mixtures (Type I)	83
6.1.2	Film growth in pure Argon (Type II)	87
6.1.3	Deposition of layered films with selected gases (Type III)	89

6.2 Morphological characterization by scanning transmission-electron microscopy	92
6.3 Electronic transport measurements	94
6.3.1 Deposition in Ar/O ₂ mixtures	94
6.3.2 Film growth in pure argon	97
6.3.3 Deposition of layered films	99
6.3.4 Layer-by-layer Al:ZnO thin film from solution-based synthesized particles	102
6.3.5 Magnetoresistance effect	104
7 Conclusion and Outlook to further research	109
List of Figures	113
List of Tables	117
A Publications and Conference contributions	119
B Nomenclature	123
C Symbol list	125
Bibliography	127

Dankwoord

Nu dat ik op het einde ben gekomen van mijn PhD wordt het tijd om bepaalde mensen te bedanken zonder wiens hulp ik dit niet tot een goed einde had kunnen brengen. Allereerst wil ik mijn promotor, prof. dr. Patrick Wagner alias Paddi, bedanken. Al tijdens de bachelor heb je mij klaar gestoomd om in de materiaal fysica te duiken en om me na de master de kans te geven te doctoreren. Moedig, want toen ik op de eerste dag hier aankwam had ik nog nooit zelf gesputterd. Gelukkig had jij hier wel "enige" ervaring in. De basis voor dit werk is uiteraard het tot voltooiing brengen van een werkende sputter reactor. En hiervoor moet ik Johnny bedanken, de techneut/magiër op het IMO, zonder jou was dit nooit gelukt. Elke dag stond ik wel aan jouw kantoor om iets te vragen, om aan je mouw te trekken om mee te komen kijken, of gewoon om materiaal te lenen (dat ik uiteraard altijd terug bracht!). Ook zonder Johan Soogen was het bouwen van de kathode een stuk moeilijker geweest, dank u om elke keer weer alle onderdeeljes te frezen en aan te passen tot het perfect was. Sorry, dat ik zo'n lastige klant was Johan.

Zonder de expertise van prof. dr. Jan D'Haen en Bart Ruttens was de optimalisatie van mijn films onmogelijk geweest. Er zijn veel SEM beeldjes nodig geweest om de sputter parameters te tweaken, en als er een probleem was met de XRD diffractometer stond er altijd wel iemand paraat om me te helpen. Voor de elektrische karakterisatie heb ik veel hulp gehad van Stoffel, de uren die we samen hebben gependend om de Hall

setup weer aan de praat te krijgen nadat er voor de zoveelste keer weer iets mis was, waren altijd plezierige dagen. Verder zou ik mijn copromotor, Prof. dr. Marlies Van Bael willen bedanken voor de interessante en kritische input die ze altijd had voor mijn onderzoek. Gezien ik op dezelfde materialen werkte, was ik ook een klein beetje lid van jullie groep. De samenwerking tussen Hanne, Kevin en Anke was altijd zeer leerrijk voor mij, omdat we voor dezelfde uitdagingen stonden. Ook wil ik hier Umicore bedanken voor het ter beschikking stellen van het Al-Zano poeder dat ik heb gebruikt om targets te maken.

Rond kersttijd 2014 heb ik ook kunnen genieten van lekkere Nespresso en een gezellige babbel in Leuven bij dr. Johan Vanacken. De gepulste velden metingen hebben zeer mooie resultaten opgeleverd. Samen met de STEM beelden van dr. Stuart Turner gaat dit een mooie publicatie opleveren. Ook wil ik Prof. dr. Hans-Gerd Boyen bedanken voor de lessen in vacuüm techniek en de XPS metingen.

De sfeer op het IMO en daarbuiten was altijd op zijn best, tussen het werk door is er veel gelachen en als de resultaten wat tegen zaten kon je altijd bij iemand terecht om je verhaal te doen. Daarom: Kasper, Marloes, Lars, Jan, Rob, Bart, Andreas, Kathia, Yasin, Evelien, Patricia, Thys,..."it was legendary".

Als laatste zijn er ook natuurlijk ook de vrienden, familie en vooral mijn papa en mama, die mij ook buiten mijn doctoraat door dik en dun hebben gesteund en die de laatste maanden op hun tippen naast mij hebben gelopen, merci voor alles.

Matthias

Samenvatting

Momenteel is er een vernieuwde interesse in de ontwikkeling van transparante geleidende oxiden (TCO's). Op basis van hun lage weerstand ($10^{-4}\Omega\cdot\text{cm}$) en hoge doorlaatbaarheid van zichtbaar licht (85%) zijn deze materialen van bijzonder belang voor de industrie wegens hun gebruik in bijvoorbeeld zonnecellen, LCD-schermen en *smart windows*. Voor de meeste toepassingen is indium tin oxide (ITO) het standaard n-type halfgeleidende TCO materiaal. Echter, de beperkte voorraad en de zeldzaamheid van indium maken van ITO een duur materiaal. Bovendien is bewezen dat indium een toxisch metaal is, zowel voor het milieu als voor de mens. Daarom is in deze thesis gewerkt aan een veelbelovende vervanger van ITO, namelijk aluminium gedoteerd zinkoxide (AZO).

De voordelen van AZO ten opzichte van ITO zijn legio. In de eerste plaats is de kostprijs een stuk lager, vooral de prijs van indium, welke \$ 750 per kilogram bedraagt, weegt zwaar door. Voor AZO echter, zijn er geen dure basis materialen nodig. Ook is de winning van indium volledig afhankelijk van de mijnbouw van zink. Op dit moment is AZO één van de mogelijke vervangende materialen die de opto-elektronisch eigenschappen van ITO evenaren. De resistiviteitswaarden zijn laag genoeg ($10^{-4}\Omega\cdot\text{cm}$) en ook de transparantie evenaart die van ITO met een minimum van 85% over het zichtbare lichtspectrum. Om dunne films te groeien met deze optimale eigenschappen is de depositiemethode van groot belang. Met dc-sputteren, d.w.z. koudkathodenverstuiving in een zelfstandige gasontlading onder

gelijkstroom, is het mogelijk om AZO films te groeien van hoge kwaliteit. Ook heeft sputteren de voorkeur bij de industriële fabricatie van dunne films omwille van de mogelijkheid grote oppervlakken te coaten. Er zijn echter nog een aantal open vragen over het effect van zuurstof en het optimale Al-doteringsniveau van deze films.

Om dunne films te deponeren, behandelt het eerste deel van de thesis de ontwikkeling van een sputterreactor met een aantal technische kenmerken die van belang zijn voor de fabricage van hoogwaardige metaaloxide lagen. Het systeem moet in staat zijn om de reactorkamer af te pompen tot een druk die lager is dan 10^{-6} hPa, dit verlaagt de kans op een accidentele incorporatie van verontreinigende deeltjes in de AZO films. Creatieve oplossingen voor de elektrische vacuümdoorvoeren en voor de koeling moesten ontwikkeld worden. Ook werd er een optie ingebouwd om in de toekomst twee verschillende materialen simultaan te sputteren. Om meer controle te krijgen over de Al-dotering werd er besloten om zelf in te staan voor de productie van sputter *targets*, door het mengen van Al-Zano poeder (Umicore, België) met een dotering van 2.4 at.% Al met zuiver en ongedoteerd ZnO poeder. Hierdoor werd het mogelijk om het aluminium gehalte te variëren.

Als *proof of concept*, werden er eerst films gegroeid met een dotering van 2.4 atomaire procent aluminium op saffieren substraten. Voor het optimaliseren van de sputter parameters werden druk, gasmengsel, de afstand tussen *target* en substraat en de substraat temperatuur, gevarieerd. Een eerste kwaliteitstest voor de afgezette AZO lagen was de groei van een glanzende en homogene film als eerste indicatie voor de kristallijne kwaliteit. Ook is deze optische parameter relevant voor de meeste toepassingen van Al:ZnO. Om de eerste selectie van de gegroeide lagen uit te voeren in functie van de elektronische transport eigenschappen, werd de vierkantsweerstand (sheet resistance) gemeten in een van der Pauw meetopstelling. Lagen met een transparantie van 96% werden verkregen door

te groeien in een gasmengsel van 2 hPa Ar en een O₂ partiële druk van 10⁻² hPa, dit komt overeen met een O₂:Ar verhouding van 0.5%. De resistiviteit van deze films werd opgemeten met een Hall bar geometrie, deze was 20 mΩ·cm ($\rho(300\text{ K})$), wat hoog is vergeleken met optimale literatuur waarden van 0.1 mΩ·cm bij 300 K.

Om de elektronische eigenschappen van de films te verbeteren, werden er *targets* gemaakt die een lagere Al dotering hadden, 1% in plaats van 2.4%. Dit zou de verstrooiing door onzuiverheden doen afnemen, omdat deze doteringswaarde onder de oplosbaarheid van Al³⁺ ionen in het ZnO rooster zit. Als we veronderstellen dat elk Al³⁺ ion één ladingsdrager creëert, wordt er een ladingsdragersdichtheid geïntroduceerd van $4.1 \times 10^{20} \text{cm}^{-3}$. Tezelfdertijd worden de films dus gedoteerd boven het Mott criterium voor ZnO ($1.2 \times 10^{19} \text{cm}^{-3}$), dit verzekert een metaal-insulator overgang zodanig dat metaal-achtige elektrische eigenschappen worden verwacht. De lagen werden afgezet in een sputtergasmengsel van zuurstof en argon, met partiële drukkens van $P_{Ar} = 2 \text{hPa}$ en $P_{O_2} = 1 - 5 \times 10^{-3} \text{hPa}$. SEM beelden onthulden een betere morfologische oppervlakte van de afgezette lagen vergeleken met de films die een Al-dotering hadden van 2.4 at.%, met hexagonale ZnO kristallieten van 400 nm. X-stralen diffractie bevestigde dat de AZO werd afgezet in de (0002) kristalrichting. De resistiviteit op kamertemperatuur verbeterde tot 7 mΩcm. Dit kan verklaard worden doordat er een kleinere verstrooiing is door grote kristallen en omdat er met een lagere zuurstof druk is gesputterd. Dit stimuleert de vorming van zuurstofvacatures, welke een positief effect hebben op de elektrische eigenschappen van Al:ZnO. Ook deze dunne films hadden een uitstekende optische transmissie van 90.8% voor zichtbaar licht.

Aangezien de optimale elektronische eigenschappen kunnen worden bereikt door het aantal zuurstof vacatures verder te verhogen, werd er gekozen om met puur argon gas te sputteren. De elektrische eigenschappen van deze lagen evenaarden de beste literatuurwaarden. Voor resistiviteit op

kamertemperatuur verkregen we een minimum van $0.094 \text{ m}\Omega\cdot\text{cm}$, tesa- men met een elektronenmobiliteit van $40 \text{ cm}^2\text{V}^{-1}\text{s}^{-1}$. Echter, op de SEM beelden onthulde deze films een wanordelijk oppervlak met een kleinere gemiddelde kristallietgrootte van 100 nm . Ook de transparantie van deze lagen verslechterde tot een transmissiewaarde van nog maar 64.72% .

Om de oppervlakte morfologie en de optische eigenschappen van de lagen gegroeid in argon verder te verbeteren, werd er een tweelagen depositie techniek geïntroduceerd. De idee was dat de bovenste laag zou gegroeid worden in puur Ar, om de optimale elektrische eigenschappen te behou- den. Deze laag zou echter afgezet worden op een AZO laag, gegroeid in een gasmengsel van argon en zuurstof. Hierdoor zou de deklaag de morfologie van de eerste laag moeten overnemen.

Uit SEM-analyses werd deze veronderstelling bevestigd, ook was de trans- parantie van deze dubbellaag films terug zeer hoog, met een waarde van 86% . Tegelijkertijd werden de goede elektrische eigenschappen van de films gesputterd in puur argon behouden. De opgemete resistiviteit be- droeg $0.69 \text{ m}\Omega\cdot\text{cm}$, met een mobiliteit van $27.5 \text{ cm}^2\text{V}^{-1}\text{s}^{-1}$. Een compleet overzicht van de de vier verschillende Al:ZnO films die gedeponeed zijn of saffier kan u vinden in Table 1.

Tabel 1: Overzicht van de belangrijke eigenschappen van de vier soorten Al:ZnO films die gegroeid zijn door sputteren, op saffier.

Sputter medium	Al_x	$\rho(300)$	Transparantie
0.5 O ₂ :Ar	0.024	20 m $\Omega\cdot\text{cm}$	96%
0.05 O ₂ :Ar	0.01	7 m $\Omega\cdot\text{cm}$	91%
puur Ar	0.01	0.094 m $\Omega\cdot\text{cm}$	64%
O ₂ :Ar + puur Ar	0.01	0.69 m $\Omega\cdot\text{cm}$	86.6%

Verdere karakterisatie van de dubbellaag Al:ZnO dunne films gebeurde met een hoge resolutie transmissie electronen microscoop. Hier werd een

homogene spreiding van het aluminium in de zinkoxide lagen bevestigd. Er was geen enkele indicatie voor de aanwezigheid van een metallisch zink netwerk. Daarom kan worden aangenomen dat de lage resistiviteitswaarden en de hoge mobiliteit intrinsieke eigenschappen zijn van de ceramische Al:ZnO films. Tenslotte werd de magnetoweerstand bestudeerd in een temperatuurbereik van 10 tot 300 K, met gepulste magneetvelden tot 50 Tesla. Dit werd gedaan omdat er in de literatuur aanwijzingen waren van een negatieve magnetoweerstand. Dit terwijl Al:ZnO geen magnetische atomen bevat, en de concentratie van magnetische ionen zoals ijzer steeds onder de detectielimiet van verschillende analytische technieken lag. De negatieve magnetoweerstand werd waargenomen tot hoge magneetvelden van 10 Tesla, dit bij een temperatuur tussen 10 en 150 K. Deze negatieve magnetoweerstand werd beschreven door de theorie van Toyozama en verder uitgewerkt door R.P. Kohsla, die steunt op de aanwezigheid van lokale magnetische momenten.

Abstract

Currently, there is a renewed and substantial interest in transparent conductive oxides (TCO's). These materials are of special interest to the industry because of their use in e.g. photovoltaic devices, LCD screens and smart windows, based on their low resistivity ($10^{-4} \Omega\cdot\text{cm}$) and high transmittance for visible light (85%). At the moment indium tin oxide (ITO) is the standard n-type semiconductor for most applications demanding a TCO. However, limited resources of indium metal make it scarce and expensive. Moreover, it has been proven that indium is a toxic material both for the environment and for human beings. Therefore, this work reports on a promising replacement of ITO, namely aluminum doped zinc oxide (AZO).

The advantages of AZO over ITO are, first of all, the cost. Especially the price of indium, which costs 750 \$ for 1 kg is a large part of the costs of ITO. AZO, compared to ITO, does not contain any costly raw materials. Also, the mining of indium is completely dependent on the mining of Zn. This is because indium is a byproduct from Zn mining. For the time being, AZO is one of the few possible replacement materials that can match the optoelectronic properties of ITO. The resistivity values are low enough ($10^{-4}\Omega\cdot\text{cm}$) to be commercially valid as ITO alternative. Also, the transparency of ITO is matched by the values of AZO, which can exceed the technically defined minimum level of 85% for visible light. To grow thin films with these optimal properties, the choice of deposition method is

of significant importance. With dc-sputtering, it is possible to grow high quality AZO films, with a low level of trace impurities. Also, dc-sputtering is the preferred deposition method in industrial fabrication of thin films, which can facilitate implementation of AZO films in the production process. However, there are still some open questions on the effect of oxygen and of the optimal Al-doping level of these films.

To deposit the thin films, the first part of this thesis focused on the development of a dedicated sputtering reactor with some technical features, which are important for the fabrication of high-quality metal oxide films. First, the system should be capable to pump down to pressures below 10^{-6} hPa to minimize the chance of accidental impurity incorporation in the film. Also, the oxygen and argon flow should be controlled with high accuracy to understand the impact of oxygen partial pressure on the AZO film. Creative solutions for the electrical vacuum feedthroughs and cooling had to be found. To have the option to grow films with different Al-doping levels, we decided to fabricate the targets by mixing conductive Al-Zano powder (Umicore, Belgium) doped with 2.4 at.% Al, with ZnO powder. The use of this commercially available ZnO which was already doped with Al (Al-Zano), and thus conductive, simplified the target fabrication. By changing the ratio of the Al-Zano and ZnO powder we can change doping percentage of the Al:ZnO films.

As a proof of concept, films were grown with an atomic Al percentage of 2.4 % compared to Zn. For the sputtering of Al:ZnO, different deposition parameters were tested to obtain an optimal result. Pressure, gas mixture, distance between target and substrate, and the growth temperature were systematically varied. The preferred optical appearance is a *shiny* and *smooth* film as a first indication for crystalline quality. This parameter is relevant in most applications where Al:ZnO is used for reasons of its good optical transmittance. Second, the sheet resistance was measured with a van der Pauw setup in order to obtain a first indication for the conductive

properties. Films with a transparency of 96% were obtained with partial pressures of $P_{Ar} = 2$ hPa and $P_{O_2} = 1 \times 10^{-2}$ hPa, which corresponds to a 0.5% $O_2:Ar$ ratio. However, the room temperature resistivity of these films was 20 $m\Omega \cdot cm$, high compared to literature values which are around 0.1 $m\Omega \cdot cm$.

To further improve the electronic properties of the films, targets were prepared with 1 at.% Al. This should decrease impurity scattering because this value is on the safe side regarding the solubility of Al^{3+} ions in the ZnO lattice. Furthermore, assuming every Al^{3+} ion introduces 1 negative charge carrier in the ZnO lattice, then a doping of 1 at.% would introduce a charge carrier density of $4.1 \times 10^{20} cm^{-3}$. At the same time the films are thus doped above the Mott criterion for ZnO, ($1.2 \times 10^{19} cm^{-3}$), which ensures a metal-insulator transition. The films were grown in a gas mixture of oxygen and argon, with partial pressures of $P_{Ar} = 2$ hPa and $P_{O_2} = 1 - 5 \times 10^{-3}$ hPa. SEM images revealed a better morphological surface arrangement compared to the films grown with 2.4 at.% Al, with hexagonal ZnO crystallites of typically 400 nm diameter. X-ray diffraction and HR-TEM proved the film was predominantly grown in the (0002) direction. The room temperature resistivity of the films was improved to 7 $m\Omega \cdot cm$, this is partially explained by a growth in a lower oxygen partial pressure. This stimulates the creation of oxygen vacancies, which triggers a more metallic behaviour of the thin films. These films exhibited excellent optical transmittance of 90.8% in visible light.

Since the optimal electronic properties could be achieved by increasing the density of oxygen vacancies, we therefore sputtered Al:ZnO in pure Ar plasma. The electrical properties of these films were equally low as the best literature values. For the room temperature resistivity we obtained values down to 0.094 $m\Omega \cdot cm$, together with a high room temperature mobility of $40 cm^2 V^{-1} s^{-1}$. However, SEM micrographs unveiled a disordered surface morphology, with a small average crystallite size of 100 nm. Also,

the transparency of the films deteriorated to 64.7% in the visible spectrum, which is too low for any optical application.

To improve the surface morphology and optical properties of the films grown in pure Ar, we developed finally a bilayer deposition technique. The first layer is a 25 - 50 nm thick polycrystalline Al:ZnO film, grown in a mixture of argon and oxygen gas, serving as templates for the further film growth under absence of oxygen. Subsequently, this layer was capped with an Al:ZnO film of 110 nm thick, which was grown in pure Ar. The resulting film had an optimal combination of both the electronic properties of the films grown in pure Ar, with a high optical transparency of 86.60%. The room temperature mobility of the bilayer films was measured to be $27.5 \text{ cm}^2\text{V}^{-1}\text{s}^{-1}$, while the resistivity was $0.69 \text{ m}\Omega\cdot\text{cm}$ at room temperature. Further characterization on the bilayer Al:ZnO films was performed with high resolution transmission electron microscopy, which showed a homogeneous spread of the Al in the films. Furthermore, no presence of a percolating Zn network in the pure Ar films was detected. This means in the films grown in pure Ar and in the capping layer of the bilayer films, no evidence was found for metallic networks, indicating that the low resistivity and high mobility are intrinsic for the ceramic Al:ZnO films. A complete overview of the characteristics of the four distinct films that have been grown in this thesis can be found in Table 2.

Table 2: Main characteristics of the four different Al:ZnO thin films which have been grown in this thesis.

Sputter medium	Al_x	$\rho(300)$	Transparency
0.5 $\text{O}_2:\text{Ar}$	0.024	20 $\text{m}\Omega\cdot\text{cm}$	96%
0.05 $\text{O}_2:\text{Ar}$	0.01	7 $\text{m}\Omega\cdot\text{cm}$	91%
pure Ar	0.01	0.094 $\text{m}\Omega\cdot\text{cm}$	64%
$\text{O}_2:\text{Ar}$ + pure Ar	0.01	0.69 $\text{m}\Omega\cdot\text{cm}$	86.6%

Finally, the magnetoresistance was studied in the range from 10 to 300

K in pulsed magnetic fields up to 50 Tesla. This was done on evidence in literature for a negative magnetoresistance and because we had the opportunity to measure the magnetoresistance up to fields of 50 Tesla. The negative magnetoresistance was detected up to fields of 10 Tesla at a temperature between 10 to 150 K. This anomalous negative magnetoresistance was not the result of any magnetic impurity incorporation. Also, the underlying atomic species in Al:ZnO are not magnetic. Yet, we detect a negative magnetoresistance because of localized magnetic moments presumably due to magnetic trace impurities with a concentration well below the detection limits of various analytical methods. This behaviour can be described by a theory developed by Toyozama for degenerate semiconductors, which was further elaborated on by R.P. Kohls and J.R. Fischer.

Part I

Introduction

Chapter 1

Transparent Conductive Oxides

1.1 Materials and properties

Transparent conducting oxides (TCO's) have the unique combination of both being transparent and conductive at the same time. This can seem to be a very trivial occurrence in nature. However, the physical properties of these materials are complex and intriguing. Basic materials normally thought of when needing a good conductor are metals. The simplest theory that gives an explanation to why metals conduct electricity was given by Drude in 1900 [1]. The theory explains electrons kinetically as small free particles jittering around in the metal crystal lattice and bouncing against the larger immobile positive ions. In this model quasiparticles called plasmons arise. In simple terms, these are an oscillation of free electron density, with a definite resonance frequency called plasma frequency. These plasmons with their plasma frequency give metals part of their optical properties. If incident light has a frequency below the plasma frequency, light is absorbed and refracted, in this case the metal is not transparent. Light with frequencies above the plasma frequency can pass

through the metal. In most metals, the plasma frequency is around the frequency of ultraviolet light. Unfortunately this means metals are not transparent in the visible spectrum of light. In TCO's however, we find the rare combination of two properties giving rise to a complete new group of materials, a metallic - like conductivity and transparency in the visible spectrum. The transmission spectrum of a standard TCO film can be seen in Figure 1.1, which clearly shows the transparency in the visible light spectrum.

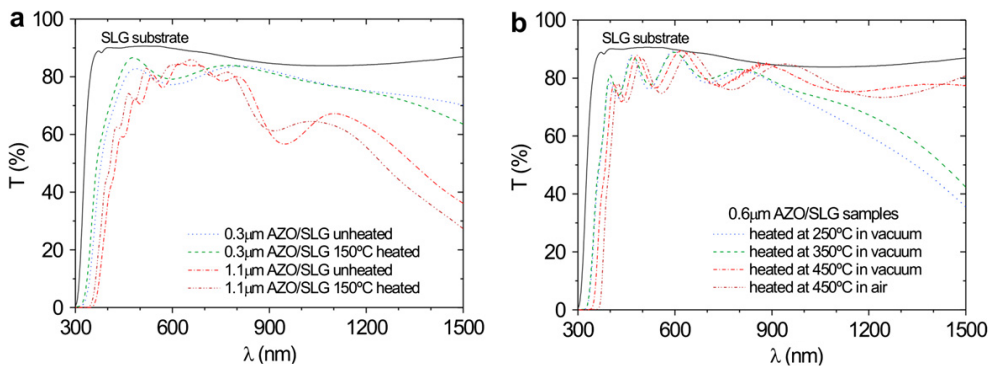


Figure 1.1: Optical transmission spectra, measured by C. Guillén, of AZO-coated soda lime glasses (SLG). The films are varied by thicknesses (a) and annealing atmosphere (b) [2]. This shows that the transparency of TCO's can be tuned to meet the specific requirements of an application. The solid lines are the transmission spectra of the SGL substrate. Resonance in the spectra are attributed to refraction of light when it passes from ambient air to the substrates. Since the bandgap of ITO is 4 eV, corresponding to a wavelength of 309 nm, the film is transparent for wavelengths above this value. Since the plasma frequency of ITO lays in the near infrared, the transparency value will diminish for incoming light with a smaller frequency [3].

1.1.1 History and examples

Transparent conductive oxides (TCO) have been known for over hundred years [4] and especially today they are a very attractive topic of research. The last ten years, the interest in the field of TCO materials has know a

large increase. This can be simply explained by an increase in the market demand for display technology, portable devices, flexible electronics, smart windows, photo-voltaic cells and most recently transparent transistors [5,6]. In all these applications, the combination of having a tunable optical transparent material, with a small resistivity ($< 10^{-4}\Omega\text{cm}$), is of utmost importance. Because of these new opportunities and applications in the field of TCO materials, there has been an increase in the search for new possible n-type and p-type TCO's [7,8]. Also the theoretical understanding and predicting the physical properties of TCO's has become an important research subject [9–11]. Especially since all basic physics research was empirical and aimed at Indium Tin Oxide (ITO), Zinc oxide and Tin Oxide. It is not only important to improve and tune the electronic, optical and structural properties of TCO's to the desired application, but also to use these materials in a wider range; gas sensing, ferro- and piezoelectric applications. Although the knowledge and research in the area of TCO's has a long history, there are still some fundamental gaps in the theoretical understanding of these materials and the predictability of their physical properties. For example, the conduction mechanism of amorphous Indium Zinc Oxide [12,13] is still under discussion. From Table 1.1 it becomes clear that over the last 100 years there was a steady incline in the number of TCO materials that were discovered, and therefore available for industrial applications. Although the standard production material ITO, was already discovered in 1947 [14], new materials are still needed and the research does not solely focus on metal oxide materials. There are other possibilities, which are particularly suited for flexible electronics. Among such materials are carbon nanotubes (CNT), graphene and conductive polymers [15–17].

There is also a more "moral drive" from society to develop new materials for overcoming the problems of global warming, by striving for a more intelligent way to cope with the energy requirements of humanity. In the last 30 years alone, the world wide energy consumption increased by more than 50%. Even former developing countries, are now industrializing with

Table 1.1: Selected historical TCO references from [18]. These give an overview of the first reference to different TCO's. Although Bädeker made the discovery of the first known TCO material as a thin film [4], the majority of the discoveries are situated after 1950.

Material	Year	Process	Reference
Cd-O	1907	Thermal Oxidation	[4]
Cd-O	1952	Sputtering	[19]
SnO ₂ :Cl	1947	Spray pyrolysis	[20]
SnO ₂ :Sb	1947	Spray pyrolysis	[21]
SnO ₂ :F	1951	Spray pyrolysis	[22]
SnO ₂ :Sb	1967	CVD	[23]
ZnO:Al	1971		[24]
In ₂ O ₃ :Sn	1947		[14]
In ₂ O ₃ :Sn	1951	Spray pyrolysis	[25]
In ₂ O ₃ :Sn	1955	Sputtering	[26]
In ₂ O ₃ :Sn	1969	Spray	[27]
TiO ₂ :Nb	2005	PLD	[28]
Zn-Sn-O			
Zn ₂ SnO ₄	1992	Sputtering	[29]
ZnSnO ₃	1994	Sputtering	[30]
a-ZnSnO	2004	Sputtering	[31]
Cd ₂ SnO ₄	1974	Sputtering	[32]
a-CdSnO	1981	Sputtering	[33]
Zn ₂ In ₂ O ₅	1995	Sputtering	[34]
a-InZnO			
InGaZnO ₄	1995	Sintering	[35]
a-InGaZnO	2001	PLD	[36]

an increasing energy demand as a consequence, see Figure 1.2.

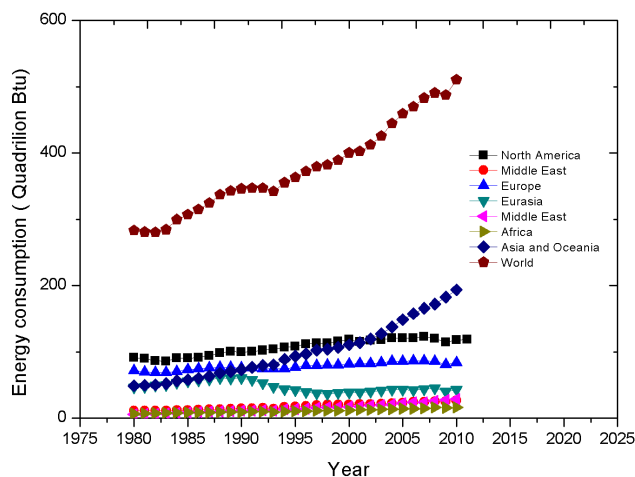


Figure 1.2: Energy consumption of the world. 1 m₃ natural gas yields ≈ 1000 BTU. Adapted from the U.S. Energy Information Administration (eia).

To achieve a greener society, sustainability is another important factor to take into account. Not only in the way we produce our new technological products, but also in design, delivery, and finally the end of life cycle. In all of these stages, the research and development of new TCO's can play a vital role. This is because TCO's are a crucial component in a wide range of technologies that strive to be carbon neutral. Namely they are used in low emissivity and smart windows, transparent electrodes for photovoltaics and OLEDs. These applications enable us to have new energy sources and to reduce our carbon footprint. The research and subsequent applications of TCO's have, in the past, been dominated by only a handful of metal oxide materials including In₂O₃, InSnO (ITO), SnO₂ and ZnO. Except for ITO, these are binary oxides. One advantage of this group of metal oxides is because of the comparatively simple composition which can be controlled during the fabrication of a thin film. These binary materials are degenerate semiconductors, their conduction is a consequence of high amount of impurity doping, both interstitial as substitutional. At a high concentration

CHAPTER 1. TRANSPARENT CONDUCTIVE OXIDES

of impurities, the individual doping atoms can form an impurity band. This system then has electronic characteristics as a metal; an increase in resistivity at increasing temperature. For example, high impurity doping as found in a degenerate semiconductor can lead to a Mott metal-insulator transition, which will further be discussed in 1.2.2.

The impurity doping of binary metal oxides can be achieved with a wide variation of dopants, a small list of possible TCO's with their respective dopants is given in Table 1.2. In this list we find ITO, which has the lowest measured resistivity of a TCO thin film with $\rho = 7.7 \times 10^{-5} \Omega \cdot \text{cm}$ and a charge carrier density of $2.5 \times 10^{21} \text{ cm}^{-3}$ [37]. Compared to copper which has a resistivity of $1.68 \times 10^{-6} \Omega \cdot \text{cm}$ [38] and silver with $\rho = 1.59 \times 10^{-6} \Omega \cdot \text{cm}$ [39], the conductivity is still 10 times lower.

AZO and GZO (gallium-doped zinc oxide) have comparable optical and electrical properties, but still, ITO is the record holder. Shallow donor levels are created when doping with a high concentration of metallic ions. This generates a large number of free charge carriers at room temperature. In ITO, for example, In_2O_3 is doped with Sn, a possible explanation is that the In^{3+} cations are substituted by Sn^{4+} , resulting in an increase of charge carriers [40]. Table 1.2 also contains some non-metallic dopants for metal oxides. ZnO can be doped with for example Ge and SnO_2 can also be doped with F (FTO), another commonly used TCO in industry [41–43].

Table 1.2: Binary TCO materials with different dopants [44].

TCO	Dopant
SnO_2	Sb, F, As, Nb, Ta
ZnO	Al, Ga, B, In, Y, Sc, F, V, Si, Ge, Ti, Zr, Hf, Mg, As, H
In_2O_3	Sn, Mo, Ta, W, Zr, F, Ge, Nb, Hf, Mg
CdO	In, Sn
Ta_2O_5	

In addition to simple binary TCO's, thin films with a mixture of different combinations of common binary oxides (MgO , ZnO, In_2O_3 and SnO_2) have

been investigated. These ternary metal oxide films are not just a mixture of the donor binary systems (binary-binary systems also exist), but are a complete new material with the typical properties for a TCO. For example, by making a mixture in the ZnO-In₂O₃ system, it is well known that materials are produced which have a stoichiometric composition Zn_mIn₂O_{3+m} where $m = 2 - 7$ [34]. If XRD is used to study the crystallographic properties of the system it clearly proves that a novel oxide was formed [45]. Some of these new TCO materials have remarkably good electronic properties that almost match the resistivity of ITO. Minami *et al.* have grown different films with a mixture of tin oxide and indium oxide. At a certain mixture of 40% SnO₂ and 60% In₂O₃, a new TCO In₄Sn₃O₁₂ was produced. This new TCO had a resistivity of $2 \times 10^{-4} \Omega \cdot \text{cm}$ and was very inert to etching and oxidizing at high temperatures [45]. A wide range of ternary TCO compounds has been discovered, and research still continues [46–50].

All the TCO materials that have been discussed until this point are n-type semiconductors. In order to have fully see-through screens in tablets, TV's and windows, there is one gap in the practical knowledge we have today of TCO's. This is a p-type semiconductive TCO, that is stable under atmospheric conditions and has matching electronic and optical properties compared to their n-type counterpart. The first successful synthesis of a p-type TCO was achieved by Kawazoe and Hosono in the 1990's with Cu based complex oxides, namely SrCu₂O₂ and CuAlO₂ [51, 52]. However, one of the disadvantages of these materials was the high resistivity and low mobility ($\mu < 1 \text{ cm}^2 \text{ V}^{-1} \text{ s}^{-1}$). This will further be explained in the next section, where it is derived that the mobility depends on the effective mass m^* of the charge carriers. For p-type TCO's this causes a problem, since only a limited materials with a low effective hole mass have been found [53]. Another problem are the oxygen vacancies, when a low energy intrinsic donor compensates the formation of holes by acceptor doping. In this way, the oxygen vacancy acts as a "hole-killer" [54, 55]. Recently there has been an increased effort in making ZnO a p-type material by

doping with Mg, Cd or Co. Unfortunately these materials have not proved to be stable [56–60]. Even if there was a breakthrough in the research and for example, Cd doped ZnO would prove to be a promising and stable material. It would go against the general philosophy of TCO materials research, to search for a non-toxic and environmental friendly alternative for ITO. Cadmium itself is very toxic and is therefore not suitable as a dopant to obtain a p-type TCO compound.

1.1.2 Applications

One of the most important applications for TCO thin films is their use in photovoltaic cells [61,62]. In conventional solar cells, a network of copper electrodes is used to close the circuit so that current can be extracted from the solar cells. However applying a electrode network causes light blocking, because the metallic materials that are currently used for this purpose are not transparent and thus block a small fraction of the incident light. For this reason, the use of a transparent material, with sufficiently low resistivity can have an advantage on the power output of the solar cell. Another advantage of using a thin film as electrode is the ease of modification of the film surface to suit special needs. Several surface modifications can be beneficial to enhance the generated photo-current of a solar cell. Reflexion at the front electrode can diminish the incident light on the active layer, which converts photons in an electron and hole pair. By using a thin film as front electrode, the surface of the film can be made rough, so any reflexion is minimized. Also, a rough surface at the front of a solar cell can induce light scattering. This way, the path length of the incident photons is elongated and the chances of absorption in the cell are increased [63]. The difference between a conventional solar cell with copper contacts and a thin film solar cell can be distinguished in Figure 1.3.

TCO materials are crucial in the fabrication of flat panel displays [66, 67]. At the moment, ITO is the most commonly used electrode because it is

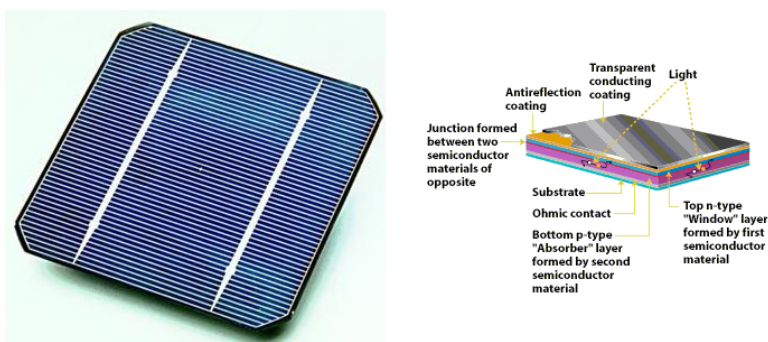


Figure 1.3: Left: A Conventional amorphous silicon solar cell, where the contact grid is clearly distinguishable [64]. Right: With a thin film solar cell, the contact grid is replaced by an n-type *window* layer, in our case a TCO film [65].

chemically stable and provides excellent electronic properties. Also for OLED (organic light-emitting diode) screens, ITO is widespread. This is because the work function of ITO, 4.4 eV [68], ensures efficient injection of holes into the organic layers [69, 70]. In the future there will be an increased use of TCO materials compared to now. It is getting more conventional to coat every window for specific purposes. Two possible applications that could be transferred to normal glass windows are solar cells and LEDs. This will lead to an increase in usable surface for energy creation by the sun, and it will be possible to have efficient lighting of rooms at night through the windows which are in turn coated on the inside with a layered thin film OLED. Another possible application is the coating with an electrochromic material [71, 72]. When a current is applied to a thin film of vanadium pentoxide, the color of the window can be regulated through the applied current [73, 74]. On small surfaces electrochromic mirrors are already used in the automotive industry with automatic dimming electrochromic rear-view mirrors. Further optical applications include low thermal emissivity windows and see-through displays. In case of thermal emissivity windows and solar control windows, a TCO coating is used as a thermal isolation layer for windows which . This works by reflecting infrared light. In the summer, solar control windows reflect IR from the sun,

this way it stays cool inside. When it is colder outside than inside, the heat will be kept inside by using thermal emissivity windows [75,76]. See-through displays were first introduced in science fiction films such as Star Trek and are extensively used in Minority Report. They are however not science fiction any more. Both Samsung and Planar Systems have already demonstrated prototypes of these see-through screens. In Figure 1.4, a prototype of Samsung's smart window is shown.



Figure 1.4: The Samsung Smart Window ©, is a transparent LCD screen which can act both as a display and as a window [77].

1.2 Physics of TCO's

Some important aspects of the basic physics of TCO's have yet to be explained. In this chapter we will briefly discuss the optical and electronic nature of TCO materials and try to understand the basic laws that govern these two interconnected properties. Firstly, the Drude model will be discussed starting with a uniform and constant \mathbf{E} -field, in practical terms: dc-conductivity. This is also needed to derive the formulas for describing the Hall-effect in Chapter 4.2. Another aspect of the conductive properties of these transparent films is the transition from a nonmetallic insulating material to a metallic, highly conductive material. This transition is discussed in reference to the Mott criterion.

To describe the basic optical properties of a TCO, the Drude model can be used again to derive the plasma frequency (ω_p), which is a first parameter in understanding the optical transparency of TCO's. The optical spectra of a typical doped TCO, such as ZnO, can be seen in Figure 1.5.

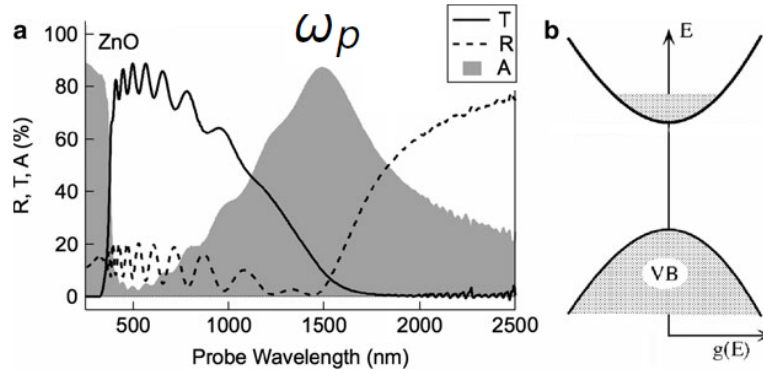


Figure 1.5: a) Optical spectrum of a commercial ZnO TCO material, deposited on glass. The solid line is the transmission spectrum, the dashed line indicates the reflection spectrum. The shaded area gives the absorption, where the plasma frequency ω_p , is indicated at a wavelength of 1500 nm. b) Simplified electronic structure of a TCO material. adapted from Ginley et al. [18].

As in Figure 1.1, oscillations in the transmittance and absorption are present in the transparent part of spectrum. Like before, this is the result of refraction of light when it passes from ambient air to the thin film substrates. The optical band gap of the ZnO thin film can be estimated by looking at the transmission. Due to the excitation of electrons from the valence band to the conduction band through incident photons, as shown in the right panel of Figure 1.5, the film is only transparent for light with wavelengths above 375 nm for ZnO films. The energy needed for the excitation from valence band to the conduction band is thus 3.3 eV and we can conclude that ZnO is a wide band gap material [18]. In the visible region (390 nm to 700 nm), the transparency of the film is around 80%. Because of plasma oscillations, the transmittance starts to decline at wavelengths above 1000 nm. Together with the decline of the transmission, the films

reflectance has a large increase for wavelengths above 1500 nm, this is again due to plasma oscillations. The plasma oscillations, also called plasmons, have a large impact on the absorbance of the material as well, with a maximum around the plasma frequency ω_p . The plasma frequency will be further discussed in section 1.2.1.

1.2.1 The Drude model of electric conduction

Paul Drude was the first who tried to find an explanation for the conductivity of metals, only three years after J.J. Thompson and his colleagues discovered the electron experimentally. In his model, Drude made some simplified assumptions, e.g. it is wrong to assume that the charged particles can be described as an ideal gas with no interaction between the particles. However, it is possible to theoretically introduce plasmons in combination with a plasma frequency, which partly gives insight in the transmission spectrum of a TCO thin film shown in Figure 1.1. Drude imagined that metals consist of a rigid mass of positive ions firmly attached into their crystal structure. Valence electrons move freely in between these positive charged ions. These valence electrons are assumed to be solid spheres which behave like the balls during a billiard game, constantly colliding with the bigger and more massive ions in the crystal lattice. Drude assumed that the electrons move in a straight line, when no electromagnetic field is present. The mean free time or relaxation time between the collisions is denoted as τ . After a collision the electrons travel in a random direction with a thermal velocity, dependent on the temperature of the bulk material. This random motion of the electrons has large similarity with the kinetic theory of ideal gases.

To start with, it is important to estimate the velocity of valence electrons in a metal. If we treat the electrons as a gas, we can calculate the thermal velocity (v_t) by the equation 1.1.

$$\frac{1}{2}m_e v_t^2 = \frac{3}{2}k_B T \quad (1.1)$$

Here m_e is the mass of an electron, k_B is Boltzmann's constant and T is the temperature. Next we define the mean free path ℓ , which is the average distance between collisions and the relaxation time τ , which is in turn the average time between electron-electron collisions. Both these physical concepts can be related as $v_t = \frac{\ell}{\tau}$. With this information about the system, we go to the following step, that is to introduce a constant electrical field \mathbf{E} which yields a force on each electron of $e\mathbf{E}$. Using Newton's second law we can derive the acceleration of every electron in the field, which is given in Equation 1.2.

$$\mathbf{a} = \frac{e\mathbf{E}}{m_e} \quad (1.2)$$

This acceleration produces a change in velocity of the electrons, more precisely $\mathbf{v} = \mathbf{v}_t - \frac{e\mathbf{E}t}{m_e}$, where t is the time since the last collision. The average velocity can now be calculated by Equation 1.3.

$$\langle \mathbf{v} \rangle = \langle \mathbf{v}_t \rangle - \frac{e\mathbf{E}\langle t \rangle}{m_e} = -\frac{e\mathbf{E}\tau}{m_e} \quad (1.3)$$

The average thermal velocity $\langle \mathbf{v}_t \rangle$ equals 0 since the direction of movement is random. Consider now a cylindrical conductor with a cross-sectional area of A , where the electrons are moving with a velocity \mathbf{v} . The number of electrons passing the area in a certain time dt equal to $n\mathbf{v}Adt$, where each electron has charge $-e$ and n is the number of valence electrons per unit volume, the charge carrier density. This way, we arrive at an expression for the current density \mathbf{J} .

$$\mathbf{J} = -ne\langle \mathbf{v} \rangle = \frac{ne^2\tau}{m_e}\mathbf{E} \quad (1.4)$$

where the conductivity σ equals

$$\sigma = \frac{ne^2\tau}{m_e} \quad (1.5)$$

Clearly we have derived Ohm's law here $\mathbf{J} = \sigma\mathbf{E}$. Another important property which has an impact on the movement of charge carriers through a material is mobility, denoted μ . It is a measure of how quickly an electron (or hole) can travel in a metal or semiconductor when an electrical field is exerted on the charged particles. So in this aspect we can define the mobility as in Equation 1.6.

$$\langle \mathbf{v} \rangle = \mu \mathbf{E} \quad (1.6)$$

If we combine the Equations 1.3 and 1.6, we get 1.7

$$\mu = \frac{e\tau}{m_e} \quad (1.7)$$

In his model, Drude also derived a general equation of motion for electrons under a force $F(t)$. The momentum of a particle, an electron in this case, is $\mathbf{p}(t)$ at any time t . When looking to the time $t + dt$, two different things can occur; 1) the electrons have a probability of $\frac{dt}{\tau}$ to undergo a collision. In this case they will lose all momentum and will regain a random momentum plus $F(t)dt$. So they contribute to the total momentum of the system with a fraction of $\frac{dt}{\tau}F(t)dt +$ random component; 2) The chance of not having a collision is given by the probability $(1 - \frac{dt}{\tau})$. After the time they will have gained some momentum $F(t)dt$, so the additional total momentum to the system is $(1 - \frac{dt}{\tau})(\mathbf{p}(t) + F(t)dt)$. Combining these two possibility's yields the net momentum after a time dt : $\mathbf{p}(t + dt) = (1 - \frac{dt}{\tau})(\mathbf{p}(t) + F(t)dt) + F(t)\frac{(dt)^2}{\tau} +$ random component.

By neglecting higher order terms in dt and reasoning that a random component to the momentum in turn averages out to 0, we get the equation of motion of an electron under a given force $F(t)$.

$$\frac{d\mathbf{p}}{dt} + \frac{\mathbf{p}(t)}{\tau} = \mathbf{F}(t) \quad (1.8)$$

Starting from the equation of motion of an electron under a given force, the Drude model can also predict the plasma frequency (ω_p) of a metallic material, which can predict if a an electromagnetic wave (light) can pass

through a metal or is dissipated by the metal. Since the plasma frequency is dependent on the mass of an electron m_e , we have to introduce the effective mass of a charged particle (in this case an electron), which takes into account the interaction between electrons and the crystal structure. This is an extra parameter which highly influences electronic properties of materials, since the mobility is also dependent on the mass of an electron. So we will define the effective mass of the charge carrying particle as m_e^* . The equation for the plasma frequency is now given by [78]:

$$\omega_p = \sqrt{\frac{ne^2}{m_e^* \epsilon_0 \epsilon_r}} \quad (1.9)$$

If the incident light wave has a frequency ω , light will be reflected if $\omega < \omega_p$. If however, the frequency of the incident light is $\omega > \omega_p$, then the metal or metallic material will be transparent [18]. For all TCO materials, also Al:ZnO, the measured plasma frequency lies in the near infrared region of the wavelength spectrum, meaning that they are transparent for visible light.

1.2.2 Mott metal-insulator transitions

It is basic knowledge that a semiconductor will be insulating below a given temperature, and will start to conduct when the temperature rises above a certain value. With some imagination we could explain this as follows. At low temperature, each site in the material contains a certain amount of electrons, this is equivalent with the scenario we had in the derivation of the Drude model. However, the difference is that the electrons are bound at their site. Every site has a total charge of zero. When an electron wants to escape the site, a restoring force is created and the electron will be pulled back by the positively charged site it left behind. An electron has to gain a sufficient amount of thermal energy, $\frac{1}{2}k_B T$, to escape. The energy of the electrons is described by Boltzmann statistics and if the energy (temperature) is high enough, a significant amount of electrons will have

gained sufficient energy to leave there bounded state, this is commonly called the band gap. These electrons leave an electron hole behind and are now free charge carriers that are able to conduct current. At high temperature, the non-conducting material becomes conducting.

The Mott model explains the phenomenon of the transition from an insulating material to metallic conductivity, and back. The physical mechanism for this transition from an insulator to a metallic conductor happens when the electron density changes, due to heavy impurity doping [79]. When the electron density changes, the electron screening of the Coulomb potential is also affected. When the electron density in the material reaches a certain critical value, the screening of the Coulomb potential increases to such a level, that there are no more bound states available for the charge carriers. At this moment, the material behaves like a metal. In semiconductor literature, such a heavily-doped semiconductor with metallic conductivity is called a degenerate semiconductor [80]. An example for the Mott transition is Silicon which is doped heavily with Phosphorous [81]. Experimental data on the existence of nonmetallic to metallic transition of a material can be seen in Figure 1.6.

To describe a Mott transition and estimate the number of charge carriers needed to induce the transition, Kittel [80] uses the model of an isolated hydrogen atom which can be seen as an individual impurity state because of the large Coulomb screening. This can be done because the solution of the appropriate Schrödinger equation has a similar result to the one for a hydrogen atom. The differences are that the mass of the free electron m_e is replaced by an effective mass m_e^* , and the hydrogen radius (a_0) is replaced by an adapted Bohr radius a_H^* . From P.P. Edwards et al. [78], we know that the same result is applicable to ITO and other TCO's. The mean Bohr radius of the first eigenvalue is

$$a_H^* = \frac{\hbar^2}{m_e^*(e^2/\epsilon_r)} = \frac{a_0 \epsilon_r}{m_e^*/m_e} \quad (1.10)$$

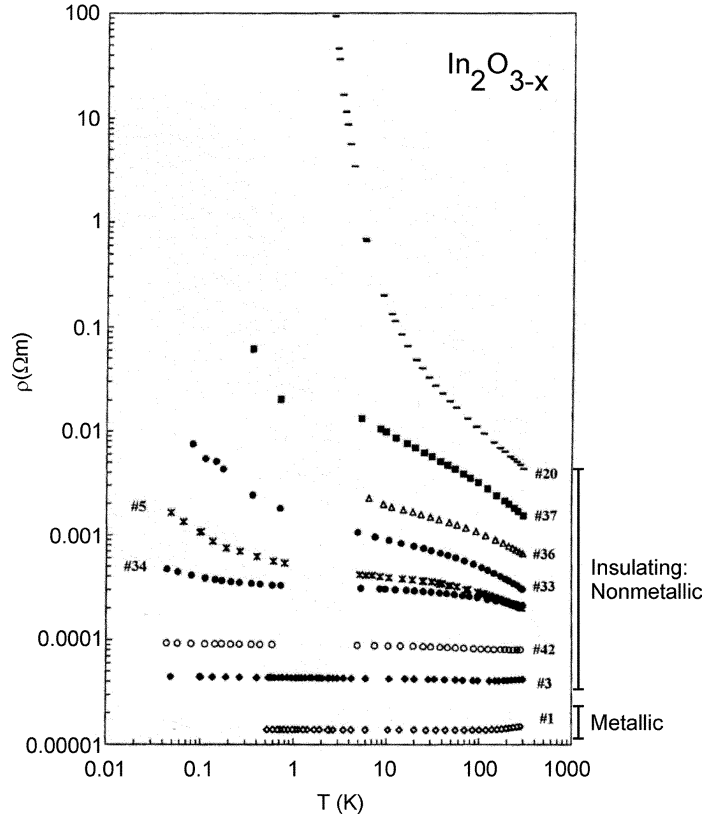


Figure 1.6: Measuring the resistivity dependency on temperature for several amorphous indium oxide thin films clearly demonstrate the transition from semi-conductive to metallic behaviour. Sample # 1 (lowest curve) is metallic, all other thin films are nonmetals, which can be clearly seen by a decreasing resistivity with temperature. the data and graph are adopted from [78, 82].

If we insert literature values for ITO taken from [78, 83, 84] where $m_e^* \simeq 0.35m_e$ and $\epsilon_r \sim 4$, we get a mean Bohr radius of $a_H^* \simeq 6.05 \text{ \AA}$. It is an experimental fact that if a semiconductor like Si is doped with a high enough number of donor atoms, so with a small inter-donor distance, the semiconductor will behave like a metal concerning its conductive properties. We can extrapolate this to the following: At absolute zero temperature, such a semiconductor (in a metallic state) still has a finite conductivity. At the other end of the spectrum we can have a semiconductor with a low

amount of donor atoms, so with a large inter-donor distance. This material will be an insulator and will have a zero conductivity at an absolute temperature of zero Kelvin. With this knowledge, we can have the following definition of a metal and an insulator [85,86].

$$\begin{aligned}\sigma(T = 0K) &\neq 0 && \text{Metal} \\ \sigma(T = 0K) &= 0 && \text{Insulator}\end{aligned}$$

Mott also concluded that the transition of the insulator state (localized electrons) to the metallic state (delocalized electrons) occurs at a critical concentration of charge carriers n_e delivered by the donors. This means that the neighboring donor sites start forming a percolating network via overlapping of their respective Bohr radii. This critical number of charge carriers is called the Mott criterion, given in Equation 1.11 [85,87].

$$n_c^{1/3} a_H^* = K \quad (1.11)$$

Where a_H^* is the Bohr radius of the donor and n_c is the critical charge carrier density. The factor K varies between 0.18 and 0.376 depending on the theoretical model [88,89]. If we again take Equation 1.10, and fill in the values of ZnO $m_e^* \simeq 0.29m_e$ and $\epsilon_r \sim 8.65$, we can find values for n_c ranging from $1.33 \times 10^{18} \text{ cm}^{-3}$ to $1.21 \times 10^{19} \text{ cm}^{-3}$ [88].

The Mott metal - insulator transition must also be discussed in regard to the electronic density of states and band structure [90]. As mentioned before, at an absolute temperature of zero Kelvin, a semiconductor will have zero conductivity. At $T = 0$, the Fermi level μ_F is located in between the valence- and conduction band. When impurities are added to the semiconducting material (doping), localized defects are created inside the forbidden zone between the valence- and conduction band. These impurities in turn can create donor centers or capture electrons. When the semiconductor is now heated, free charge carriers are created. The number of created

free charge carriers is therefore dependent on the ratio between the ionization energy of the donor- or acceptor centers and temperature. The ionization energy of the donor centers is indicated in Figure 1.7.a by E_d , the acceptor centers by E_a . After doping, the band structure is in between that of an insulator and a metal and the conductivity will be activated by temperature. When the number of impurities is further increased, their energy levels fuse together into an impurity band. However, Figure 1.7.b clearly shows that the wave functions of the impurities are still localized. At this stage, adding more impurities to the impurity band can cause an overlapping in their respective wave functions which leads to delocalization. This delocalization leads to metallic-like behaviour at $T = 0$ K, where the Fermi level μ_f is now located inside the impurity band.

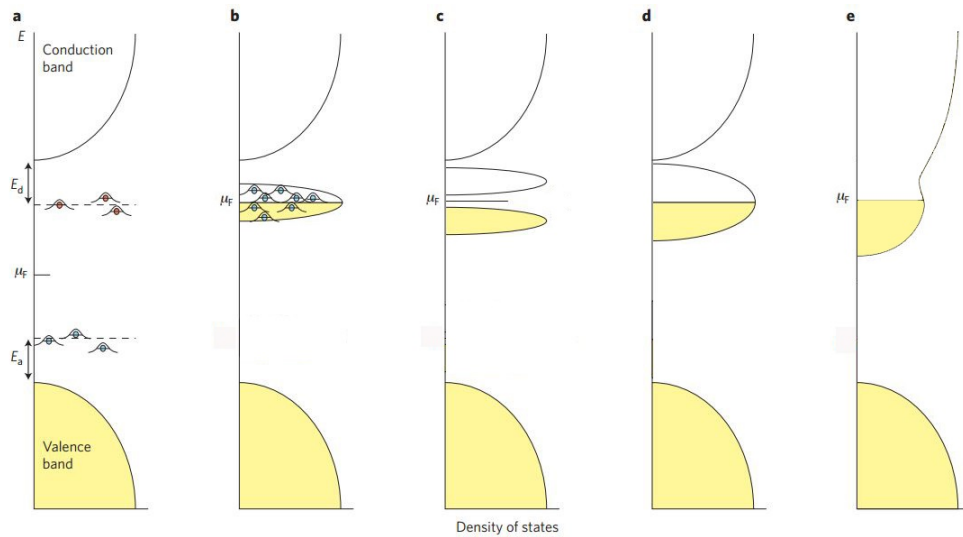


Figure 1.7: Evolution of band structure in a metal - insulator transition. The n-type doping ratio increases from **a** to **e**. Adapted from [90].

Mott proposed moreover that, because of strong on-site correlations, the spin-degenerate half-filled impurity band splits in an empty band and a full band [85,90]. This situation can be seen in Figure 1.7.c. When the doping ratio of the semiconductor is further increased, the two separate bands

from Figure 1.7.c start to overlap, and a metal - insulator transition takes place as indicated in 1.7.d. At such a high doping level of the semiconductor, Coulomb screening of the impurities will occur, as mentioned in the beginning of this section. On adding one more impurity to the critical concentration will extend all states and their energies are now within the band of delocalized states [90].

We can use the metal - insulator criterion, derived by Mott also as a guideline for optimizing current TCO materials: we know that in order to have a high conductivity of a TCO thin film, the number of charge carriers has to exceed a certain number defined by the Mott criterion in Equation 1.11. On the other side, from the Drude model, we have learned that increasing the number of charge carriers also has an effect on the optical transparency of the thin film. Another aspect not previously mentioned is that of electron scattering. If the material is doped with an impurity, for example Al in ZnO, impurity scattering will occur. Because of impurity scattering, the mobility will decrease. This can be detrimental for certain applications, for example solar cells. This will be further discussed in Chapter 4.2, where a detailed description of the Hall effect and the measurement of mobility will be given. We have shown that there are several mechanisms in play that have an effect on the optical and electrical properties of the film. As previously mentioned in Section 1.1, these two physical phenomena set a lower limit for the charge carrier concentration to achieve metallic-like conductivity (Mott criterion) and an upper limit to still guarantee high optical transparency in the visual spectrum (Drude model for plasmon excitation). A balance has to be found between the required conductivity (and in extent, the mobility) and the number of charge carriers. When using a film for applications, we have to ensure that we are above the critical charge carrier density predicted by Mott, but the charge carrier density also has to be minimized in order to maintain optimum transparency to visible light.

1.3 The ceramic material: Zinc Oxide

Currently, indium tin oxide or more precisely, tin-doped indium oxide (ITO) is the prevalent n-type TCO used in consumer technology owing to its good optical transmittance and low resistivity as discovered in the 1950's [91]. According to the U.S. Geological survey however, indium is expensive and costs \$ 750 per kg (May 2014). Recent studies also prove that indium is a hazardous material for both environment and humans [92–95]. In Figure 1.8, the costs of raw In and Zn are compared from 1990 to 2012, it shows that the price of indium is almost 200 times the value of Zn. One could argue that we are dealing with thin film applications for both ITO and Al:ZnO and the amount of material needed is thus relative small and does not outweigh other costs. However, from Figure 1.8, we can clearly deduce a dependence between the two price graphs. Both have a large rise in costs per weight in the year 2007. This can be explained by the fact that there are no indium mines, but only zinc mines. The sharp peak in price between zinc and indium, is due to a mining incident in the largest zinc mine in China. The Price of zinc and indium are correlated with each other because raw indium is a byproduct from mining zinc and the processes used to extract the indium from zinc ore are hazardous to the local environment.

Replacing ITO with a sustainable and cost effective alternative is therefore inescapable. Because Zn is an abundant element and is less toxic than In, doped-zinc oxides are promising to replace ITO [96]. ZnO is a wide band gap material, with a direct band gap of 3.3 eV and with n-type semiconducting properties resulting from oxygen vacancies and zinc interstitials [7]. The electrical properties of ZnO are further enhanced by substituting Zn with group-III elements such as Al, Ga and In [97]. From these possibilities, aluminum-doped zinc oxide (AZO) is a very promising candidate because of the low achievable resistivity, high carrier mobility, and due to the fact that aluminum is less expensive than indium and gallium. Several deposition techniques have been used to deposit Al:ZnO,

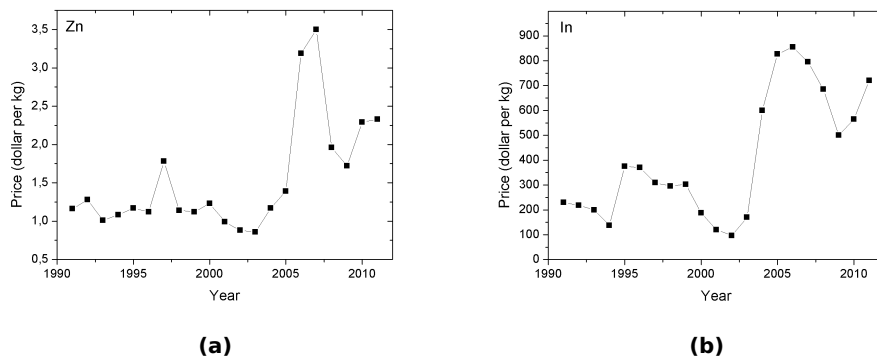


Figure 1.8: (a) Price of a kilogram Zn in dollar, per year. (b) Price of a kilogram In in dollar, per year.

including dc- and rf-sputtering [98–100], chemical vapour deposition techniques (CVD) [101], electron beam evaporation [102], cathodic arc deposition [103], sol-gel deposition [104], and laser ablation [105]. Since sputtering deposition, be it rf or dc, is commonly used by the semiconductor industry to deposit thin layers, and because sputtering produces high quality films, this work will focus on reactive dc sputtering in argon-oxygen mixtures. In Table 1.3, a compendium is given of growth methods and the resulting electrical properties of Al:ZnO films. The possible structures of ZnO can be found in Figure 1.9, where three different crystal forms can be ; cubic rocksalt, cubic zinc blende, and hexagonal wurtzite. The hexagonal crystal structure is thermodynamically the most stable of these three allotropes [106]. The lattice constants of hexagonal zinc oxide are $a = 0.3249$ nm and $c = 0.5207$ nm [107]. When sputtering ZnO either doped or undoped, the wurtzite structure will be grown.

There are three different doping places in the hexagonal ZnO crystal structure of the Zn^{2+} atoms by Al^{3+} . To ensure optimum electronic properties and free carrier generation, Al^{3+} should be substituting the Zn^{2+} at the tetrahedral site [108, 109]. Two other possibilities however exist, doping in an empty tetrahedral site or interstitial doping. The three different dop-

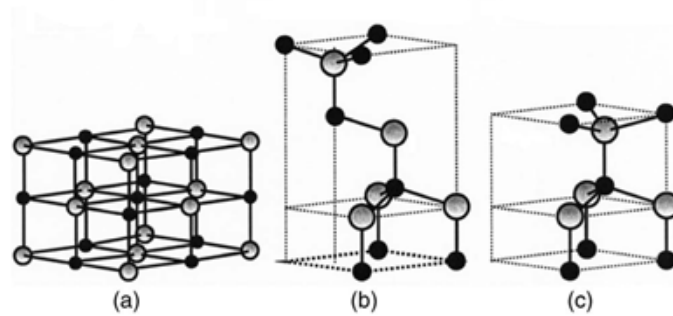


Figure 1.9: The stick and ball representation of the three polymorphs of ZnO; a) cubic rocksalt, b) cubic zinc blende and c) hexagonal wurtzite. The black spheres denote the oxygen atoms and the shaded grey sphere are the zinc atoms. [7].

ing positions can be seen in Figure 1.10.

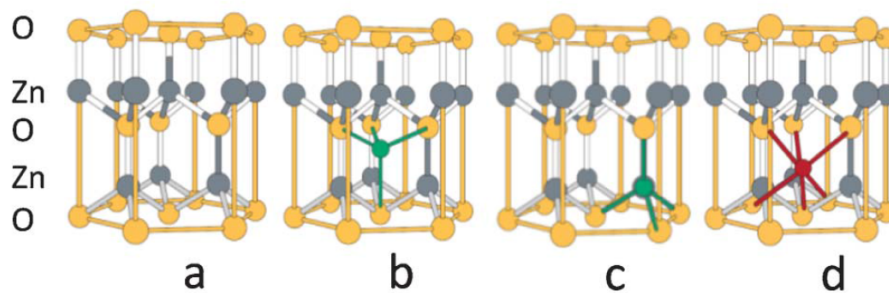


Figure 1.10: a) A ball and stick representation of the hexagonal wurtzite ZnO crystal structure. The three possible doping sites of Al^{3+} are: b) at the empty tetrahedral site, c) substitutional for the Zn^{2+} atom at the denoted position and d) interstitial [110].

Table 1.3: Deposition methods and electric properties of Al:ZnO thin films at room temperature. ρ : resistivity; n : majority charge-carrier density; μ : majority charge-carrier mobility. DCMRS: dc magnetron reactive sputtering; RFMRS: rf magnetron reactive sputtering; ACMRS: ac magnetron reactive sputtering; LPCVD: low pressure chemical vapor deposition; PLD: pulsed laser deposition.

Deposition method	ρ ($10^{-4}\Omega \cdot cm$)	n ($10^{20}cm^{-3}$)	μ ($cm^2V^{-1}s^{-1}$)	Reference
Pulsed DCMRS	7.33	5.84	14.6	[111]
DCMRS	4.2	2.6	57	[112]
DCMRS	18	0.19	1.8	[98]
DC+RFRMS	5	9	20	[100]
ACMRS	4	4	32	[112]
RFMRS	14.3	4.25	10.3	[113]
RFMRS	2.86	7.59	30	[114]
RFMRS	3.7	4	± 40	[99]
RFMRS	10	2.5	6	[115]
LPCVD	35	3.5	± 5	[101]
PLD	21	0.69	10	[105]
Sol-gel	80	40	25	[116]

Chapter 2

Thin film deposition

The fundamental research in TCO materials focuses on understanding the optical and electrical properties. This part of the research is needed to control both the optical and electrical properties separately and to think of new ways to optimize these materials for their appropriate application. But the fundamental work on how different parameters have an effect on the material is not the only important factor to consider when designing a perfect TCO system. The morphological structure, both in bulk and of the surface, also plays an important role in the development of superior TCO materials. The structure of a thin film can change because of the interaction between substrate and deposited material. Also, stress in the crystals and grains, that can be introduced during the growth process, can have an influence on the transparency and electronic properties of the film. Understanding this on both a fundamental- and practical level is paramount in order to deliver a quality product [97]. For the practical work of depositing thin film TCO films, I will summarize different possible techniques that are used for thin film deposition. The technique that will be used further within the experimental work of the thesis will be dc sputtering without using magnetrons. However, also characterization was performed on solution deposited films by means of the sol-gel technique. This can give an indication how important the choice of deposition technique can

be. Apart from one (solution deposition), all techniques described in the following sections have one thing in common: vacuum. The etymology of the word, contains its physical meaning. Vacuum comes from the Latin "vacua", which means empty. So, a vacuum chamber would translate to an "empty chamber", and this is exactly one of the main reasons we need vacuum in order to produce qualitative films. First, there is a smaller chance of contamination of the film if there are only gas atoms present of the material one wants to grow on the substrate. Secondly, the impact velocity of the particles on the substrate is determined from the energy they gain during the growth process. If the pressure is high, the molecules or atoms that are accelerated in the direction of the substrate can have multiple collisions with other particles, thus reducing their velocity. In more physical terms this means that the mean free path of the particles in the vacuum chamber is lower when the pressure is higher. Vacuum deposition is divided into two different "families", namely Physical Vapour Deposition (PVD) and Chemical Vapour Deposition (CVD). In PVD the driving processes for the growth of the film are physical in nature, a solid is converted to a gas. The gas of the target material is transported and deposited onto the substrate. There, it condenses into a solid of usually different stoichiometry and physical morphology. In CVD, chemical reactions occur where volatile precursors react and decompose on the substrate, forming a different compound than the original precursors.

2.1 Sputter deposition

The first technique of Physical Vapour Deposition (PVD) was the simple process of evaporation where a target material is heated until the point of evaporation. At high vacuum the atoms or molecules are thus transported to the substrate by a ballistic flow and deposited. But, in evaporation the uniformity of a film can be a problem and also the evaporation of alloys is in many cases not feasible. In sputtering, instead of using heat

to eject material from the target, it is bombarded with high speed ions, which transfer energy to the target material. In return, neutral atoms or molecules from the target can escape, and are ejected in a straight path until they collide with other particles or preferably a substrate. To accomplish this, a plasma is used in the vacuum chamber. In short, plasma is sometimes called the fourth state of matter, it is an electrically neutral medium composed of positive and negative particles that interact with each other by means of electromagnetic fields and it can be created by ionizing a gas. In sputtering the plasma is used to create the particles to bombard the target. Since the sputtering technique was used for the majority of my work, a detailed description will be given.

The sputtering mechanism is regulated by a momentum (energy) exchange between the atoms and ions in the target material by collisions of incident ions. These ions start a cascade of collisions that can recoil to the surface of the target with an energy exceeding the surface binding energy. In this instance we can speak of sputtering. The ejected ion moves in a straight path where it can collide with the substrate material which is placed in front of the target [117]. The basic setup of a sputter system can be seen in Figure 2.1. To start a sputter deposition the plasma has to ignite, which is shown in 2.2. The plasma formed in a sputter deposition is a glow discharge plasma, which is formed by the passage of an electrical current through a low-pressure gas. When a voltage of several hundred Volts is applied between the cathode and anode, a small part of the gas atoms are ionized. This is due to random processes, for example thermal collisions. In sputtering the cathode has a negative potential, while the anode is connected to the ground, together with the vacuum chamber. When the voltage increases further to values above the ionization voltage, Townsend discharge occurs and the plasma starts to glow visibly [118]. The now positive ions are attracted to the negative potential of the cathode, and the electrons are attracted to the anode. Further collisions between ions, electrons and neutral atoms increase the fraction of ions in the gas. When the number of charged particles is increased, the

conductivity of the plasma increases, therefore a lower voltage is needed to sustain the glow discharge plasma.

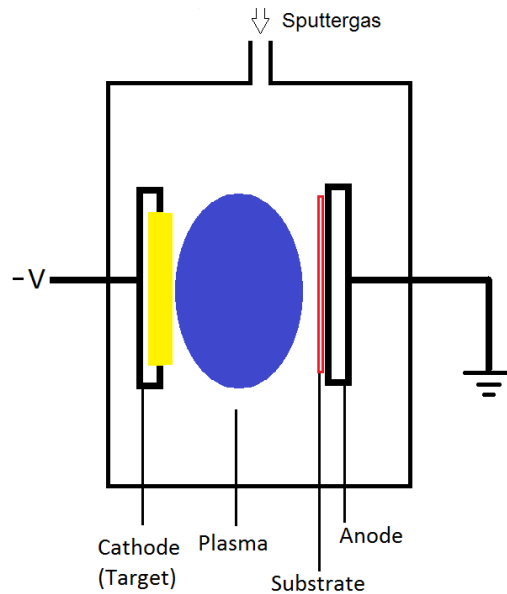


Figure 2.1: A basic sputtering system setup. The potential over the anode and cathode starts at a couple of hundred of Volts, which is needed to initiate and sustain a plasma.

In Figure 2.2 the basic deposition operation of sputtering is explained graphically. Positive Ar^+ ions are accelerated to the cathode because of the potential over anode and cathode. In the collision of the Ar^+ ions with the target, target atoms are ejected and electrons are created. The created electrons feed the formation of Ar^+ ions and help sustain the glow discharge plasma. The choice of gas is important to maximize the momentum transfer from the gas ions to the target material, the atomic mass of the gas ions should be comparable to the mass of the target atoms. An inert gas is preferred for sputter deposition to reduce any reactive processes. The most prevalent gas is the noble gas Ar, which is suitable for sputtering most metals and ceramics. For lighter target materials, Ne is used. Another important sputter parameter besides the current, voltage

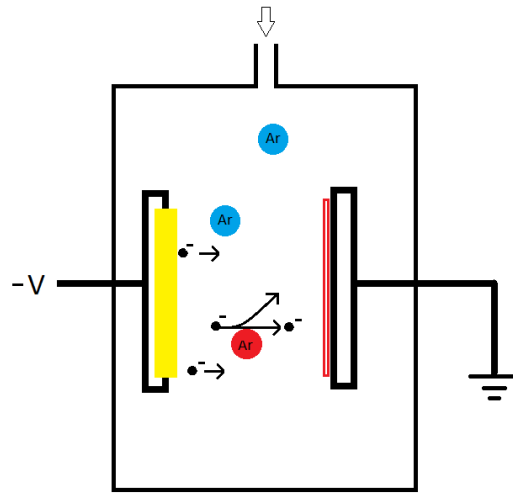


Figure 2.2: Free electrons are accelerated to a grounded anode. Neutral gas atoms, here Ar, are ionized and accelerated to the negatively charged cathode.

and sputter gas choice, the sputter pressure plays an equally important role. With low sputter pressure (10^{-2} to 10^{-1} hPa), the ejected target material follows a ballistic trajectory from target to substrate, and the impact material has a high energy. On the other end of the gas pressure spectrum, with high pressures (>1 hPa), the ejected ions collide with the gas atoms numerous times. The mean free path-length diminishes, the target material moves in a diffusion based manner, and will undergo a random walk. Finally, the ejected target material will reach the substrate at diminished speeds. This deposition ensures a slower and thermal growth process [119]. This can be mitigated by decreasing the distance between the target and the substrate. Finding optimal parameters of the complete sputter process is a difficult task, but it has the advantage of having a wide control on the process. As a consequence, the deposited film characteristics can be tweaked to their desired parameters.

In Figure 2.3, the basic principle of the glow of the plasma in sputtering is explained graphically. An electron can be absorbed by an Ar^+ ion. The gained energy is released by a photon with a defined energy. Another possibility is when a free electron collides with a Ar atom in the plasma. The electron can bring another electron into an exciting state, thus creating an excited Ar atom Ar^* . Afterwards the excited electron decays to its normal state, releasing a photon with discrete energy. The energy radiated from the atoms and ions in the plasma is discrete, meaning only photons with a certain energy are emitted. Each gas has several distinct spectral lines, an Ar plasma glows in a lilac or violet color. Other reactive gases can be added to the sputter gas mixture, for example O_2 and N_2 , to grow ceramic materials. A chemical reaction of the reactive gas with the target material gives control over the film composition [120].

The basic process of sputtering described above, is called diode sputtering. There are, however, other technological advances that have been made to the thin film deposition by sputtering. For example, in magnetron sputtering, a magnet with a field between 10 to 500 mT is placed behind the target. This way the charged particles in the plasma are enclosed by the field lines of the magnetic field created by the magnets. The collision rate of ions into the target can be intensified, which gives the possibility to sputter under lower pressure. This, without diminishing the sputter rate of the deposition system. Different setups of magnetrons can give even further control on the morphology of the deposited film. The introduction of conventional "balanced" magnetron's took place in 1970. They were an important innovation, and solve some fundamental needs in thin film deposition by sputtering [121]. In a balanced magnetron, the magnetic field lines are fully confined to the region strictly above the sputtering target at the vacuum side of the cathode. The invention of the unbalanced magnetron, with a wider spreading of magnetic-field lines, at the end of the '80, and the further development to what is now known as multi-source "closed-field" sputtering systems at the beginning of the '90, dramatically increased the possibilities of sputtering and the control of deposited film

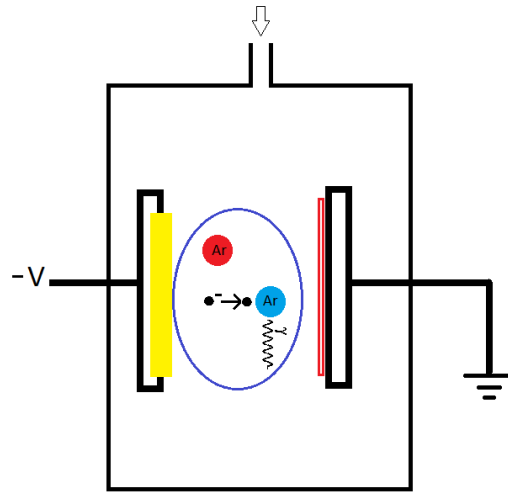


Figure 2.3: An Ar^+ ion returns to its neutral ground state when an electron fills one of the outer orbitals. In return, the energy gained, is lost by radiation (γ).

morphology. Closed-field unbalanced magnetron sputtering (CFUBMS) for example, is an exceptional versatile technique with a broad range of commercially viable deposition rates [121].

The design differences between conventional- and unbalanced magnetron are rather small, however the difference in resulting film characteristics can be significant. In a conventional magnetron, the plasma is strongly confined in the target area and expands outward. Substrates placed close to this area will be exposed to different impacts of ions of the plasma which can strongly influence the film properties. Substrates which are placed further away from the plasma, in an area with lower plasma density will not show this effect. The ion-current (typically $<1 \frac{\text{mA}}{\text{cm}^2}$) on the substrate will be too low to have a significant effect on film properties [122]. This system however has the disadvantage that it is difficult to produce homogeneous and dense films this is one of the reasons why regular diode sputtering was preferred in this thesis. Another solution to this problem would be to

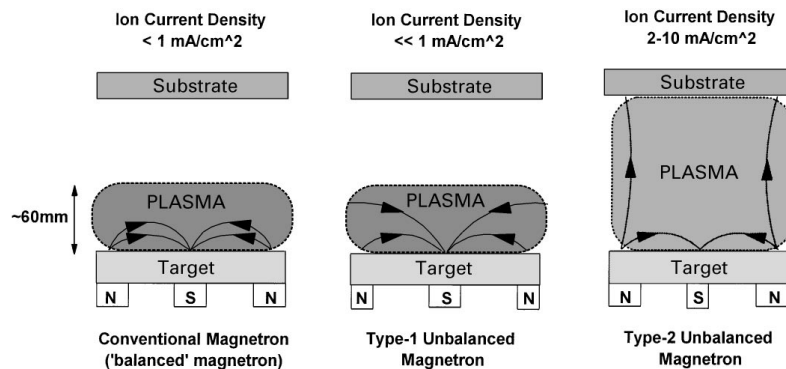


Figure 2.4: Schematic representation of the plasma confinement in conventional and unbalanced magnetron's. The surface size of the N and S magnet denotes the field strength. Adapted from [121]

adapt the magnet strengths of the magnetron to achieve a high ion flux and low energy (<100 eV), this will again facilitate the growth of dense films [123]. These conditions are provided by an unbalanced magnetron, where the outer magnet ring is stronger than the central pole magnet. This configuration was later called type-2 unbalanced magnetron by Window and Savvides who described the different effects of the used magnet configuration in magnetrons [124–126]. A schematic representation of plasma confinement in different magnetron setups is shown in Figure 2.4.

Almost one in three articles published to date use a variation of sputtering to deposit TCO films. Recently, research was focused on enhancing the deposition rate and more homogeneous film growth onto large substrates. An up-to-date overview of TCO films sputtered in recent years can be found in the review article of G.J. Exarhos [97]. He mentions the following interesting n-type TCO's: $\text{In}_2\text{O}_3\text{:Mo}$ [127, 128]; ITO [129–131]; ZnO [132]; $\text{In}_2\text{O}_3\text{:ZnO}$ [133, 134] ZnO:Ga [135, 136]; and ZnO:Sc/Y [137]. Further examples of deposited Al:ZnO by means of sputtering can be found in Table 1.3.

2.2 Chemical vapour deposition

Chemical vapour deposition (CVD), is a means of deposition a thin film by use of a chemical process. A substrate is exposed to chemical precursors which can react or decompose on the surface of the substrate to form the desired composition of the thin film. Different types of CVD are in use, for example atmospheric pressure CVD (APCVD), low pressure CVD (LPCVD), and plasma enhanced CVD (PECVD). Clearly most modern techniques use vacuum techniques for the deposition to mitigate any undesired trace material pollution. To enhance the rate of chemical reaction, a plasma can be used to facilitate the breaking of chemical bonds in the precursors (PECVD). This means the substrate temperature can be lowered to achieve the same chemical reaction as non-plasma enhanced CVD, which can be vital in the processes used by the semiconductor industry. A disadvantage of CVD can be the stability of certain precursors under the vacuum used for PECVD. Low vapor pressure of the precursor can be a problem for the delivery of precursor to the substrate. Another disadvantage is the fact that numerous precursors are toxic. Also, CVD has the possibility to contaminate the deposited film with trace atoms which are present in the precursor molecule. However, certain materials can hardly be processed to a high quality thin film in another way but CVD, a well-known example is doped diamond [138]. In principle, a CVD reactor is not very different from a sputter reactor. A target is not necessary because the film material is delivered by the precursor source gases which are added to the carrier plasma gas. A schematic view of a PECVD reactor can be seen in Figure 2.5. TCO are usually grown by metalorganic CVD (MOCVD), which makes use of organometallic precursors that can decompose to metal oxides. The deposition of thin films by MOCVD does not need an ultrahigh vacuum environment, which is a cost effective advantage compared to sputtering. However, this advantage does not outweigh the costs associated with the needed organometallic precursors. The use of MOCVD in the field of TCO technology thus limits itself to the research into p-type TCO

thin films [97, 139, 140].

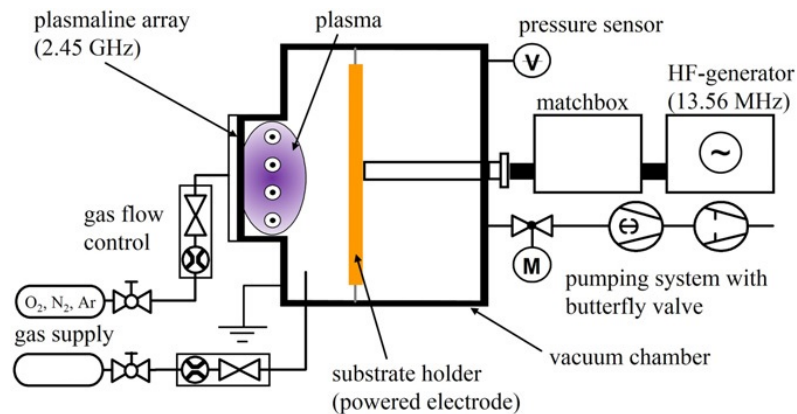


Figure 2.5: Schematic representation of a PECVD reactor, adapted from [141].

2.3 Pulsed laser deposition

Pulsed laser deposition is a PVD technique for thin film deposition processes. PLD uses a high-power pulsed laser (Nd:YAG, KrF or ArF), which is focused on a target in a high vacuum chamber. Upon collision, the target material is vaporized and a plasma plume is formed, this happens irrespectively whether the target material is electrically conducting or insulating. The energy of the incident laser is first converted to electron excitation of target atoms. Afterwards, this energy is converted to thermal, chemical and mechanical energy. Consequently target material is ejected in the direction of the substrate and deposited. A schematic of a PLD deposition system can be seen in Figure 2.6.

Although the quality of thin films grown with PLD is outstanding, it has some drawbacks. PLD is not used as a widespread production technique due to costs and the difficulty to grow films on wafer size substrates. Also, due to the high direction dependence of the plasma plume, films can have a pronounced thickness variance across the substrate. The physical process behind the deposition mechanism of PLD is still not perfectly under-

CHAPTER 2. THIN FILM DEPOSITION

stood, meaning that optimizing parameters can be a difficult and a time consuming task [97]. All of this makes PLD a perfect technique for the research sector in thin film deposition and general material science. PLD definitely lacks some important properties needed in a commercial and industrial setting, up-scalability is one of the largest drawbacks, that prevent the commercial use of PLD due to the very small substrate surfaces. Nevertheless, it is applicable for the deposition of a wide variety of materials including TCO's [97, 142–144]. High quality, epitaxial Al:ZnO on (0002) sapphire substrates have been produced [145]. However, the electronic properties of the films are not improved compared to sputtered films [114]. Other recent articles on n-type TCO's grown with PLD are: Al:ZnO [146, 147]; AZO/Ag/AZO multilayers [148], ZnO [149], IZO (Indium Zinc Oxide) [150], InGaZnO [151] and ITO [152]. For p-type TCO's, SrCu₂O₂ was grown with PLD [153]. But the usual problems concerning p-type TCO films remained, the films were not stable in air, and even after annealing conductivity was low. Also, CuAl₂O was grown with PLD, but again low conductivity (0.3 S/cm) compared to n-type materials is reported [154].

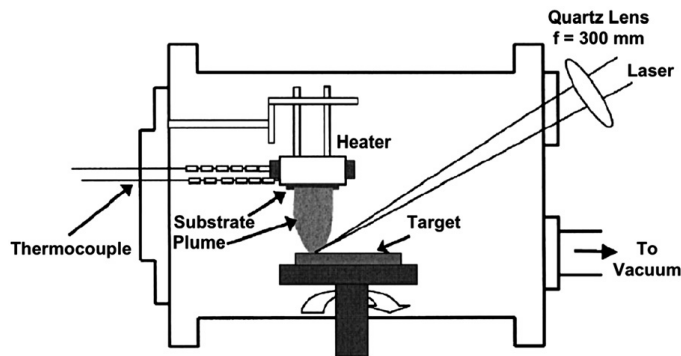


Figure 2.6: Schematic representation a PLD deposition system. [97, 155].

Part II

Methods and Materials

Chapter 3

The sputtering reactor

For the deposition of the chosen TCO material Al:ZnO, we developed a dedicated sputtering system for high pressure sputtering of Al:ZnO films. The base vacuum chamber of the system was recycled from an old analytical system and thoroughly refurbished before use. The system was designed with some essential features, which were of vital importance for the fabrication of high quality metal oxide films.

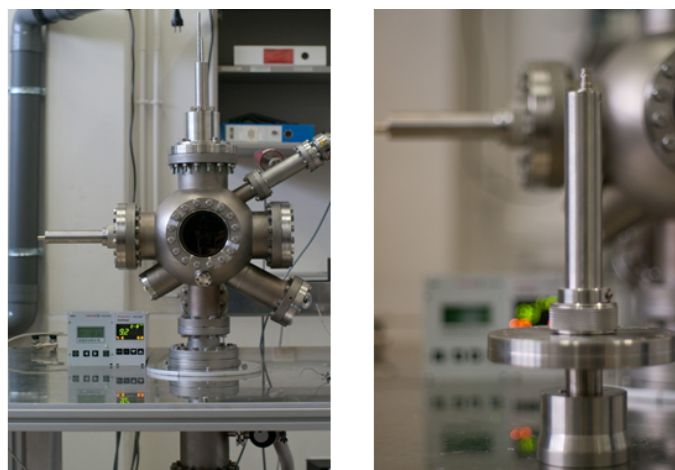


Figure 3.1: Photograph of the assembled sputter reactor (left), and of a cathode with vacuum flange (right).

CHAPTER 3. THE SPUTTERING REACTOR

First, a low base pressure should be achieved to ensure the chemical purity of the films. The base pressure of the sputtering system before the start of the deposition was usually around 10^{-6} hPa. Otherwise there is a possibility that trace elements still present in the chamber pollute the growing film, and therefore deteriorate the properties of the thin film. From literature, most Al:ZnO films are grown with Ar as sputter gas. O_2 was sometimes added in low partial pressures (0.1% to 1%) to affect crystallite sizes and the number of grain boundaries [105]. Because ZnO is

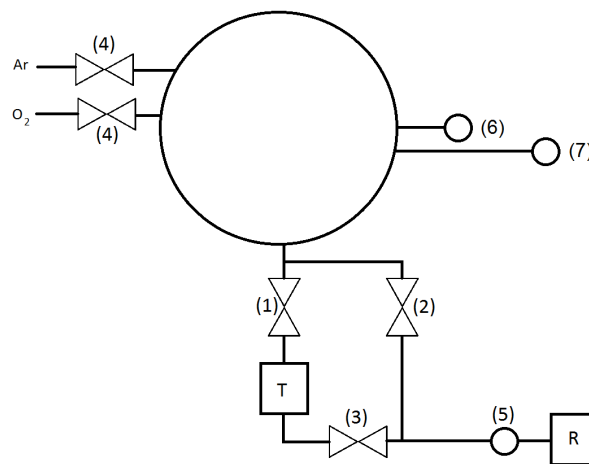


Figure 3.2: Technical drawing of the vacuum system. (1) UHV CF-100 gate valve; (2) ISO-KF 40 angle valve; (3) ISO-KF 40 inline valve; (4) all-metal gas dosing valve; (5) condensation trap to mitigate fomblin oil [®] contamination of the chamber; T turbomolecular pump; R rotary vane pump; (6) capacitive gauge; (7) compact full range gauge.

a material that is very sensitive to the presence of oxygen gas, it must be possible to regulate the partial pressure of O_2 with high precision. To achieve this, two manually operated all-metal gas dosing valves (Pfeiffer, PF I52 035) were added, one for argon and one for the inlet of oxygen. In our case, both gases had a purity of 99.9999%. To control the pressure via all-metal gas dosing valves we installed two different pressure gauges. First, we installed a compact full range gauge (Pfeiffer, PT R26 252), with

a measuring range from 1000 hPa down to 5×10^{-9} hPa. This broad range can be achieved by the combination of both a Pirani sensor and a cold cathode gauge. This sensor was used to monitor the base pressure of the system before the start of the growth process. To measure the pressure during the deposition process precisely, we opted for a capacitive vacuum gauge (Pfeiffer, PT R24 622). This gauge is capable of measuring pressures between 10^{-3} hPa and 11 hPa with an error between actual and indicated pressure of only 0.2 %, independent of the gas type. The pressure value of both sensors was read out with a gauge controller which could display the pressure for both gauges at the same time (Pfeiffer; PT G28 280). To achieve the base pressure, the chamber is pumped down with a turbomolecular pump with a CF-100 mount (Pfeiffer, TMU 261 P) . As backing pump for the turbo pump, we chose a Duo line 5 MC (Pfeiffer, PK D61 727) with a flow rate of 5 m³ per hour. This rotary vane pump is especially designed to withstand corrosive gases, such as oxygen and was therefore equipped with fomblin oil ®, a fluorinated lubricant. The technical drawing of the complete vacuum system can be seen in Figure 3.2.

3.1 Sputtering cathode

The sputtering cathode was designed according to a layout that was originally developed for the deposition of thin films of high temperature superconductors [156]. The main modifications to the original design refer to the overall size, water-cooling solutions and electrical connections outside and inside the cathode. We chose to miniaturize the cathode and sequentially the target, to ensure film homogeneity and to keep the possibility to grow under stable plasma conditions at high pressure up to ca. 5 hPa. In order to ensure a maximal experimental flexibility, a possibility to connect not only a DC sputter-current source but also an RF generator was foreseen. Because the cathode operates under high voltage and is water-

CHAPTER 3. THE SPUTTERING REACTOR

cooled, careful consideration was given to shielding of the various parts at high potential and of parts that are in contact to the chamber, which is at a grounded potential. Also, the water-cooled area behind the copper target holder is shielded carefully with viton O-rings to separate it from the vacuum. Because shielded parts are in contact with vacuum, Teflon was chosen for these parts. The out gassing of teflon parts is negligible and because of its high dielectric strength (60 MV/m) it is an ideal material for this application.

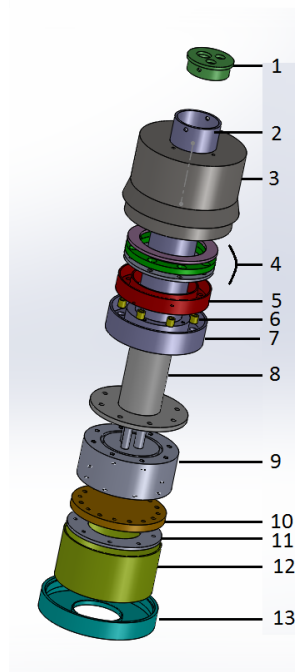


Figure 3.3: Technical drawing of the sputtering cathode optimized for high-pressure sputtering in oxidizing atmospheres. The function and material of the different parts is explained in Table 3.1. Designed with Solidworks 9.1.

The maximum target size is 1.5 inch (38.1 mm) in diameter. The target-holder and the cathode shield can be adjusted to fit smaller and thicker targets, but the thickness should be between 1 and 4 mm. Inside the cathode head, the possibility to insert ring magnets to initialize magnetron

sputtering is foreseen. The front cathode shield must not have an electrical contact with the target and the inner part of the cathode because it is connected to the ground. However, the distance between the target holder and the cathode shield can be adjusted because it is attached to the cathode by a screw-thread. A schematic view of the cathode with its inner parts is shown in Figure 3.3. Before building in the cathode and pumping down, the water cooling has to be checked for leaks and the electrical contact between the inner- and outer cathode parts should be measured. Otherwise there is a chance of contamination and of water residues between the different parts in the cathode. When the water cooling of the cathode is active, the resistance between outer- and inner cathode parts should be in the order of $1.5 \text{ M}\Omega$, corresponding to the resistance of the water in the coolant hose. For lower resistance values than $1.5 \text{ M}\Omega$, short-cuts and plasma arcing can become a problem during growth.

3.2 Substrate holder

The substrate holder consists of a heater, which is suspended in an inox box. This minimizes any lost thermal energy, only a small amount is lost due to radiative energy. This can be seen in Figure 3.4. The copper heat shield can also be distinguished in this photograph. The most important part of this substrate holder is the heater itself. An Inconel wire (Thermocoax, France) with a length of 1 m and a diameter of 1 mm was used as heater element. The resistance of the wire is $12.5 \text{ }\Omega$ and it can carry a maximum current of 4 A, which yields a total power of 200 Watt. The heater element was coiled up in the form of a Fermat spiral to ensure a minimal magnetic field. Afterwards, it was firmly clamped in between two inox discs (diameter 36 mm) and welded together. In vacuum it can be heated up to $900 \text{ }^\circ\text{C}$. The current is supplied by a Delta Electronics power source, which is controlled by a Eurotherm PID module. The temperature of the heating element is measured by a K-type thermocouple which was

CHAPTER 3. THE SPUTTERING REACTOR

Table 3.1: Different parts of the sputtering cathode.

Part	Function	Material
1.	Feedthrough for cooling and coaxial BNC bus	inox
2.	Central tube, connected to the ground	inox
3.	upper cathode body, screw-thread ended	inox
4.	Rings to isolate the bolts, which are at high potential	inox and teflon
5.	U-body which fits the rings of part 4	teflon
6.	Isolation for the bolts	teflon
7.	Fits part 4, 5 and 6	inox
8.	Isolation for the central tube	teflon
9.	Central cathode body with water and electric feedthrough, Top and bottom are equiped with a viton O-ring. Hollow for magnetron inserts.	inox
10.	Target holder	Copper
11.	Target holder ring, covers the edge of the target and the epoxy glue.	aluminium
12.	Isolation between part 3 (ground potential) and 9,10 and 11 (high potential)	teflon
13.	Cathode hood, at a grounded potential	inox

firmly attached in the rear inox disk of the heater. This way, the heater temperature is measured at an equivalent position as compared to the substrate, which is situated on the front disk. The filament-type copper connections inside the vacuum chamber were completely shielded from the chamber wall and from the substrate holder by Macor (Corning inc., U.S.) and with ceramic pearls. These electrical connections were made with twisted wires of silver coated copper to ensure bend constancy and to reduce oxidation under oxygen partial pressure.

As mentioned before the target inside the cathode is water cooled, but there is also a heat shield surrounding the target holder. This diminishes any radiative heating of the chamber wall, keeping in mind that the heat-

CHAPTER 3. THE SPUTTERING REACTOR

able substrate holder is designed for temperatures up to 900 °C. If the wall heats up, it can become a problem to maintain a stable sputter pressure during the growth process. The heat-shield is made of copper to ensure a good thermal conductivity and a meander of tubing is present in the copper heat-shield to keep it cool. The shield can be seen in Figure 3.4, together with the substrate holder and heater. Because the substrate holder and heat shield are welded together, a rotatable and hollow vacuum feed through had to be used. In this system we opted for a ferro-fluidic hollow feedthrough (Metallic flex; Germany) with a hollow shaft of 30 mm diameter. In the future, it is even possible to attach an electro-motor to the rotatable feedthrough, which gives options to sputter composite materials and multilayer films by alternating deposition from the two cathodes.



Figure 3.4: The substrate holder of the sputter system. The front part of the radiation shield is removed for better visibility. The heat shield and steel box (radiation shield) are clearly visible. One (0002) sapphire (Al_2O_3) substrate and four additional sapphire platelets to ensure homogeneous heat spread, are glued directly on top of the inox heater disk.

3.3 Substrate preparation

Films were grown on two kinds of substrates. For research purposes, 10×10 mm sapphire (0002) substrates with a thickness of 1 mm were used (CrysTec GmbH, Germany). The substrates were cut with an orientational precision of < 0.3° meaning that the c-axis plane faced up. An XRD spectrogram was performed initially on all sapphire samples to test the crystal orientation before their use. A typical θ -2 θ scan of the substrates can be seen in Figure 3.5.

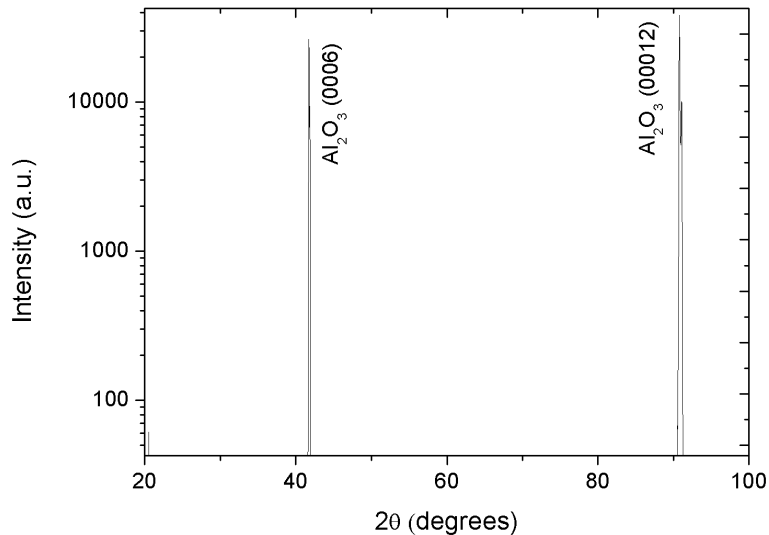


Figure 3.5: XRD spectrogram of a blank (0002) oriented synthetic sapphire (Al_2O_3) substrate.

Since the sapphire substrates were unpolished at the backside, we opted for a second substrate material to test the transparency of the Al:ZnO films. These borosilicate substrates had a dimension of 25× 25 mm and a thickness of 1 mm.

Before the growth process, samples undergo a standard cleaning procedure. First, to remove any residue, the samples were put in nitric acid,

HNO₃, with a concentration of 1:2 HNO₃: H₂O. This was done for 20 minutes in an ultrasonic bath. After this step, the samples were thoroughly rinsed with distilled water and put in isopropyl alcohol a temperature of 80 °C for 20 minutes. The samples were blown dry with nitrogen. To provide an excellent thermal contact between the samples and the heater, we made use of a thin layer of colloidal silver to attach the substrates to the heater. Therefore, we used E-Solder 3021 (Epoxy Producte GmbH, Germany). The A and B component of the silver epoxy glue were thoroughly mixed in a Petri dish and applied on the heater, the substrate was pressed in and any epoxy residue was removed with a scalpel. Four additional sapphire substrates were glued on each side of the (0002) sapphire substrate and again, any left over silver epoxy was removed. This way, a virtually larger substrate area is achieved, providing better homogeneity of the deposited films. The substrate holder was placed in a vented aluminium box and the power supply for the heater was connected. To evaporate the epoxy solvents, the substrate holder was heated up to 500 °C with a rate of 1 °C per 3 seconds. At 500 °C the white silver epoxy turned black due to the decomposition and evaporation of the solvents. After 5 minutes, only the white colloidal silver is left and the substrates are cooled down to room temperature. The final result can be seen in Figure 3.4. The front heat shield was put on top of the heat shield to seal of the box completely besides the substrate on which a film had to be grown. Finally the complete substrate holder was placed into the vacuum chamber which is pumped down to its base pressure well below 10⁻⁶ hPa.

3.4 Sputtering target

To foresee the option to do a doping-percentage study on the Al:ZnO thin films, the decision was made to make all the targets in-house. This can be done by mixing ZnO and Al-Zano powders, pressing the powder into a disk-shaped target and finally sintering the target: of which the result can

be seen in Figure 3.6. Until now, two different target types were used, the first one with the original Al percentage of 2.4 % at. Al compared to Zn and a second one with 1 at.% Al compared to Zn. The base material for the targets is a Zano-Al powder (Umicore; Belgium), which contains 2.4 wt.% Al compared to Zn. In order to lower the doping ratio, the Al-Zano powder was mixed with ZnO powder (99.99 % trace metals basis, Sigma-Aldrich, USA). Zano-Al powder has the advantage over a purely powder mixed target of Al_2O_3 and ZnO that sputtering from an already conductive target is more convenient than using a non-conductive target for which rf-sputtering has to be used. Although the cathode design does allow rf-sputtering, for simplicity and cost efficiency it was preferred to sputter in dc-mode. It is possible to make a conductive target from two non-conductive oxide materials (ZnO and Al_2O_3). However this process was found to be not straightforward, since the maximum temperature of our vacuum oven is 1100 °C, which is not sufficient to have a full solid-phase reaction necessary to incorporate the Al atoms in the ZnO crystal structure [157]. Since the Zano-Al powder was already conductive, it would save time and efforts, and would leave more time to optimize the grown films. Also, the aluminium percentage in the target can be adjusted by other means. In order to produce a target with a lower amount of aluminium, it is possible to mix pure ZnO with the Zano-Al powder. The other way round, a higher amount of aluminium can be incorporated in the film by mixing the target Zano-Al powder with pure Al_2O_3 powder. However, this was not necessary, as described in Chapter 6.1.

To press a target with a pneumatic press with a pressure of 10 tons of weight, a special stamp had to be made. The stamp was made from hardened steel to ensure it can withstand the needed force to press the target. It is capable to press targets with a diameter of 1.5 inch (38 mm), and targets can have a thickness of up to 5 mm. Usually, a thickness between 2 and 3 mm was preferred, this is a trade-off between mechanical strength and brittleness compared to the maximum thickness that can be fitted

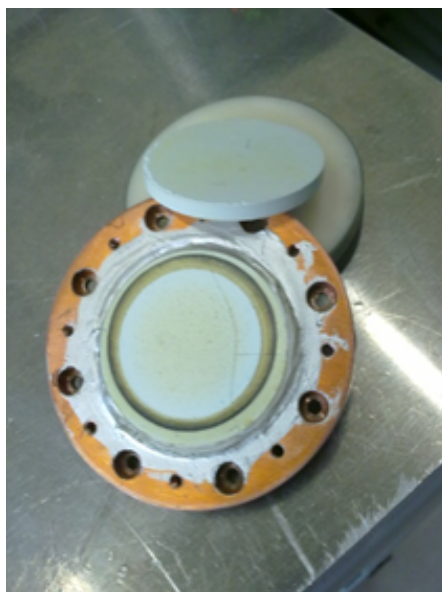


Figure 3.6: The target is glued onto a copper target holder by conducting silver-epoxy paste. On top of it lies a freshly sintered Al:ZnO target.

technically in the target holder of the cathode. In the case of the 1 at.% Al target, the Zano-Al had to be mixed with ZnO powder. To achieve a target thickness of 2 mm, 10 grams of powder had to be used. Therefore we mixed 4.167 grams of Zano-Al powder and 5.883 grams of ZnO powder. This was mixed in Planetary Micro Mill pulverisette 7 premium line (Fritsch; Germany). To mitigate the formation of cracks in the target during baking, a drop of saturated solution of distilled water and polyvinyl alcohol, with a molecular weight of 88000 g/mol, was added and mixed into the target just before pressing. This ensured a better adhesion between different grains present in the target. With heat treatment in the vacuum oven, the carbon content of the polymer will be completely removed.

As mentioned before, the pressing was done with a weight of 10 tons. Considering the surface of 1.5 inch, this means a pressure of 8.6×10^7 hPa. The last step in the fabrication process of the sputter target is to sinter the pressed disk. To fuse the particles together, a high temperature is needed. We used a vacuum oven with a base pressure of 1×10^{-7} hPa

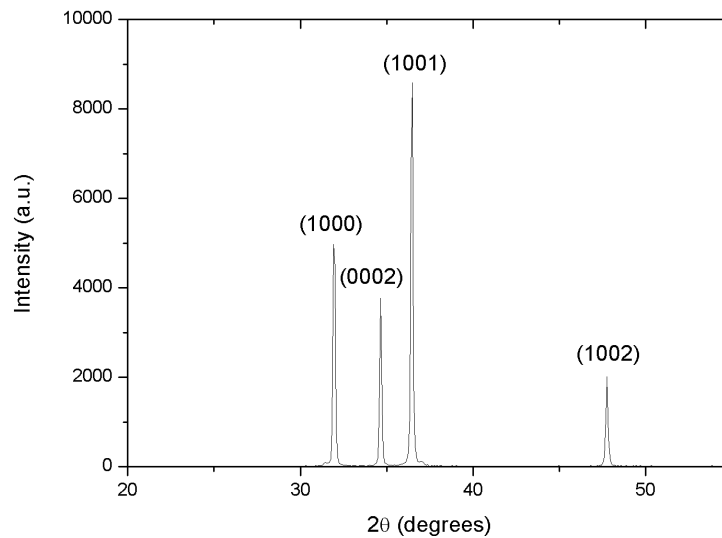


Figure 3.7: XRD spectrum of the Zano-Al powder after sintering at 900 °C for 1 hour.

at a temperature of 900 °C. The temperature rise is programmed with a rate of 100 °C per hour. The maximum sintering temperature of 900 °C is maintained for 1 hour, after which it cools down to room temperature within 8.75 hours.

The efficiency of the sintering treatment was controlled by XRD. Using the Debye-Scherrer (see equation 4.30 in paragraph 4.3) , the average crystal size can be calculated. Averaging the crystal size over the different orientations yields 25 nm before the sintering process and 59 nm after the sintering process ,proving the sintering of the target. The XRD scan in Figure 3.7 proofs that the Zano-Al is pure ZnO, no other crystal structures were detected. The incorporated aluminium is not detected in the form of Al_2O_3 .

At the bottom of Figure 3.6, a target is shown which is mounted on the reusable copper target holder. To remove an older target, a small chisel

CHAPTER 3. THE SPUTTERING REACTOR

and hammer are used to remove the larger parts. Next, the inside is polished and the last remains of the target material is removed with a Dremel multitool (Dremel, U.S.). To ensure a good adhesion between the target and copper, the now polished surface will have to be rougher. Therefore scratches are made in the copper surface of the target holder with a cutter knife. After this, the target holder has to be cleaned and prepared to be inserted in vacuum again. For this a 30 minutes cleaning step in a ultrasonic bath with isopropyl alcohol followed by blow drying with nitrogen flow, is sufficient. To fix the target on the target holder, the same E-solder silver glue (Epoxy Producte GmbH, Germany) for substrate mounting is used. For mounting one target, 1.5 grams each of the A and B component are mixed and applied on both the target and copper. The target is pressed onto the copper firmly and rotated until a good adhesion is supplied everywhere underneath the target. This is done to ensure a good thermal and electrical contact between the target and the cathode. Any excess silver epoxy is removed carefully, as to not contaminate the target with silver. A weight of 5 kg is placed on-top of the target for 2 hours, afterwards it is heated for 30 minutes at 100 °C. The electrical resistance between the target and the holder was found to be 10 Ω .

Chapter 4

Electronic-, structural- and chemical characterization techniques

4.1 Van der Pauw setup

For the electronic characterization, two different techniques were employed. After growth, the resistivity of the samples was measured with the van der Pauw method. This way, a large number of samples could be screened in a time efficient way. In contrast to measuring electronic properties with a Hall bar setup, the van der Pauw method does not require sample patterning. However, to achieve a large accuracy in measuring the Hall signal of the films, a Hall bar sample preparation was performed on selected samples. This way, the samples could be measured in a Hall bar geometry, which allows for an accurate quantification of the charge-carrier density (n) and mobility (μ). In his original work, Van der Pauw

CHAPTER 4. ELECTRONIC-, STRUCTURAL- AND CHEMICAL CHARACTERIZATION TECHNIQUES

proved that resistivity, charge-carrier density and mobility of a random flat surface can be calculated if a number of conditions are met: contacts have to lie on the circumference of the samples, contacts must be small compared to the sample area, the sample should be of uniform thickness, be isotropic and not contain isolated holes [158]. The possible geometries of a van der Pauw sample layout are shown in Figure 4.1. Due to the square shape of our sapphire substrates, we used the rectangular geometry. For measuring, we used a 2400 SourceMeter (Keithley, USA) in the 4-lead setting. This way, the current could be simultaneously applied while measuring a voltage over the contacts.

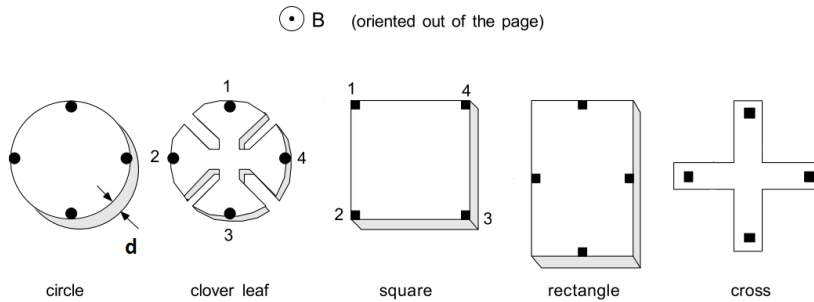


Figure 4.1: Possible van der Pauw geometries which can be used. To minimize sample preparation, the rectangle shaped geometry was employed. The figure is adapted from Lake Shore 7500/9500 Series Hall System User’s Manual [159].

The sheet resistance R_S can be calculated by Equation 4.1. However, the formula is only valid when the resistances R_{12} , R_{23} , R_{34} and R_{14} are equal. For instance, R_{12} is the resistance between points 1 and 2 as indicated in the square geometry in Figure 4.1.

$$R_S = \frac{\pi R}{\ln 2} \quad (4.1)$$

Here $R = R_{12}$, R_{23} , R_{34} or R_{14} . In the other case however, when Equation 4.1 is not valid, the resistance of Equation 4.5 has to be numerically solved by iteration. As a starting value, the estimated R_S , resulting from equation

CHAPTER 4. ELECTRONIC-, STRUCTURAL- AND CHEMICAL CHARACTERIZATION TECHNIQUES

4.1 has to be used. If for example, I_{12} is the positive DC current between points 1 and 2, as indicated in the square geometry in Figure 4.1. V_{43} is the DC voltage measured between the contacts 4 and 3 or $V_{43} = V_4 - V_3$. We can calculate the resistance of this example by Ohm's law as follows: $R_{12,43} = V_{43}/I_{12}$. Knowing this, 8 different measurements have to be done to define the resistance R_A equation 4.2, and resistance R_B equation 4.3.

$$R_A = \frac{R_{12,34} + R_{12,43} + R_{43,12} + R_{34,21}}{4} \quad (4.2)$$

$$R_B = \frac{R_{32,41} + R_{23,14} + R_{14,23} + R_{41,32}}{4} \quad (4.3)$$

$$(4.4)$$

With these two values, we have enough parameters to solve 4.5 by iteration for the value of R_S .

$$e^{-\pi \frac{R_A}{R_S}} + e^{-\pi \frac{R_B}{R_S}} = 1 \quad (4.5)$$

Now the resistivity ρ can be calculated by $\rho = R_S \times t$, where t is the thickness of the film. It is possible to measure the Hall coefficient R_H with the same setup. Therefore, two sets of measurements have to be performed, one where the direction of the magnetic field \mathbf{B} is directed into the plane, a second one where it is oriented out of the plane. For all the measurements the applied current must be kept constant. For one set of measurements (constant \mathbf{B}), we end up with four distinct voltages. When the measurements are performed for the positive and negative magnetic field \mathbf{B} , the Hall voltage V_H can be calculated. Since the values for the thickness (t) of the thin film, applied current (I) and magnetic field (B) are known, R_H can be calculated with Equation 4.6

$$R_H = \frac{V_H t}{IB} \quad (4.6)$$

4.2 Hall setup

For the Hall setup, a bridge shaped structure called a Hall bar, was used. The Hall bar is shown in Figure 4.2, where contacts 1 through 6 are the pads where an electrical contact can be made. The small contacts in the bridge geometry give an advantage compared to the bar shaped which was used before by van der Pauw [158]. In a bar shaped test specimen, point contacts can cause a large contact resistance when measuring at low temperatures such as in liquid nitrogen. The contacts of the bridge shaped Hall bar pattern have larger contact pads to ensure a small contact resistance.

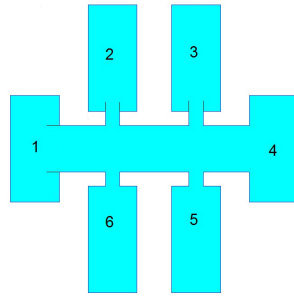


Figure 4.2: The Hall bar pattern used has a length and width of 3 mm. The width (w) of the bar where the current flows during measurement is 0.475 mm. The length (l) between contacts 2 and 3 or 5 and 6 is 0.870 mm.

A constant current is applied between the contact point 1 and 4. Meanwhile, the voltage difference (V_ρ) is measured between points 2 and 3 or 5 and 6. To compensate for any thermoelectric voltage effects [160–162], the current is switched for every voltage measurement and V_ρ is the average of those measurements. From these values, it is possible to calculate the resistivity ρ by Ohm's law as in equation 4.7 when the width (w), length (l) and thickness (t) is:

$$\rho = \frac{V_\rho t w}{I l} \quad (4.7)$$

The Hall measurements were carried out after patterning the thin films

CHAPTER 4. ELECTRONIC-, STRUCTURAL- AND CHEMICAL CHARACTERIZATION TECHNIQUES

laterally by UV lithography and wet-chemical etching in 1:1000 HNO₃:H₂O solution into 6-terminal Hall bar structures. Contacting was based on wire-bonding with silicon-doped Al-wires and conductive silver paint. To compensate for a misalignment- or offset voltage, the current was kept constant at 1 mA, and the magnetic field was alternated between -2 T and +2 T. After 15 alternations, an average Hall voltage for one current directions was calculated. In a next step, the current direction was changed to - 1 mA to compensate for thermal voltages, and the magnetic field was again alternated between -2 T and +2 T. Resistivity- and Hall measurements carried out on samples with a 48 μm wide and 87 μm long current path measured between the transverse and longitudinal voltage leads. By using a liquid nitrogen cooled cryostat, we are able to measure the electronic properties of thin films in a wide temperature range: from 77 K to 400 K. This setup can be seen in Figure 4.3. Both, resistance and Hall effect are measured with the Hall bar pattern. By using a liquid nitrogen cooled cryostat, we are able to measure the electronic properties of thin films in a wide temperature range: from 77 K to 400 K. This setup can be seen in Figure 4.3.

In metals, at high temperatures, the charge carriers will predominantly collide with phonons present in the lattice with a relaxation time τ_l . However, when the temperature drops to liquid helium temperature (4 K), the phonons extinguish. Now other scattering mechanisms can be detected, charge carriers colliding with mechanical defects in the crystal lattice and with impurities in the material (τ_i). This combination of different scattering effects was empirically formulated by Matthiessen's rule in Equation 4.8:

$$\frac{1}{\tau} = \frac{1}{\tau_i} + \frac{1}{\tau_l} \quad (4.8)$$

Here τ is the average relaxation time between collisions. If we use Ohm's law from equation 1.5, we can rewrite Equation 4.8 to express it in terms of resistivity (ρ). Matthiessen's rule is not universally valid, meaning that,

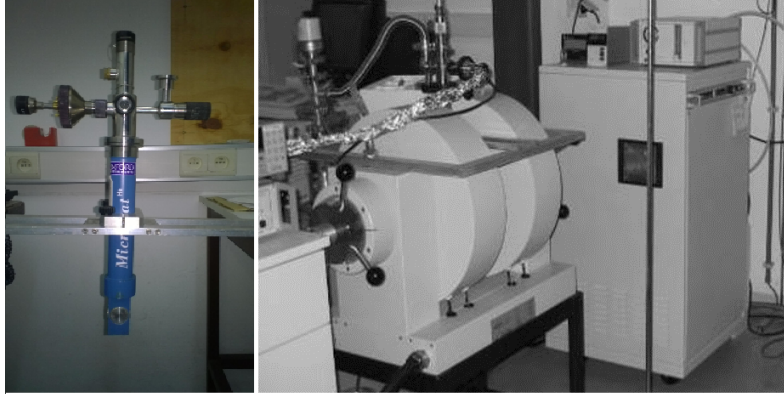


Figure 4.3: Left: The Microstat He cryostat (Oxford Instruments, UK) which contains the substrate can be cooled down to 4 K with liquid He and to 77 K with liquid N₂. A PID controller is attached to regulate the temperature. Right: The cryostat is placed between a tapered pole electromagnet (Bruker B-E 15 v, Germany) with magnetic field strengths of up to 2.07 T.

if the relaxation times of the different scattering effects are dependent on each other, Equation 4.8 does not hold.

$$\rho = \rho_i + \rho_l \quad (4.9)$$

Here ρ_i is the resistance resulting from collisions with impurities in the material, and ρ_l is the resistance resulting from collisions with lattice vibrations (e.g. phonons). This empirical observation made by Matthiessen in 1864 shows that in a resistance measurement, the contributions of different scattering mechanisms can usually be independently added to calculate the total resistance of a material.

We now define the conductivity of a semiconductor as in Equation 4.10

$$\sigma = \frac{1}{\rho} = q(\mu_p p + \mu_n n) \quad (4.10)$$

Where n is the density of negative charge carriers and p is the density of the positive charge carriers. Since we are working with ZnO doped with negative charge carriers, and since we know that in general most

ZnO materials are negatively doped semiconductors we can assume the density of positive charge carriers p to be negligible. This gives us:

$$\mu_n = \frac{1}{ne\rho} \quad (4.11)$$

Since according to equations 1.7 and 1.5 $\rho \sim \frac{1}{\tau} \sim \frac{1}{\mu}$ we can write

$$\frac{1}{\mu} = \frac{1}{\mu_l} + \frac{1}{\mu_i} \quad (4.12)$$

Again, μ_l is the mobility attributed to lattice phonon scattering and μ_i is a contribution of the scattering of impurities.

While studying the nature of the force that is exerted on a current carrying conductor by a magnetic field \mathbf{B} , Edwin Hall discovered the Hall effect in 1879 [163]. For the derivation of the Hall effect we can use the principles that we used to describe the Drude model of electronic conduction in section 1.2.1. In Figure 4.4, a simplified presentation of a Hall bar structure is drawn to derive the equations needed to calculate the electron mobility μ_e and density of negative charge carriers n from a Hall measurement.

In the illustration a current I is injected through a thin plate with a thickness t and a width w . We define the current density through the Hall bar as $J = \frac{I}{tW} = qnvd$. A magnetic field B , which stands perpendicular to the direction of the current, exerts a Lorentz force on the moving charge carriers, in our case electrons. If the charge carriers are positive holes, the same effect occurs, in the sense that also holes, moving in the opposite direction, are deflected to the same side of the Hall bar. We can write the total force, consisting of the Lorentz force and Coulomb force, on the charge carriers as in equation 4.13.

$$\mathbf{F} = q(\mathbf{E} + \mathbf{v} \times \mathbf{B}) \quad (4.13)$$

Here, \mathbf{E} is the electric field, perpendicular to it is the magnetic field \mathbf{B} and \mathbf{v} is the drift velocity of the charged particles. Because we define \mathbf{v} , as the drift velocity, we are calculating the net Lorentz force on the particles.

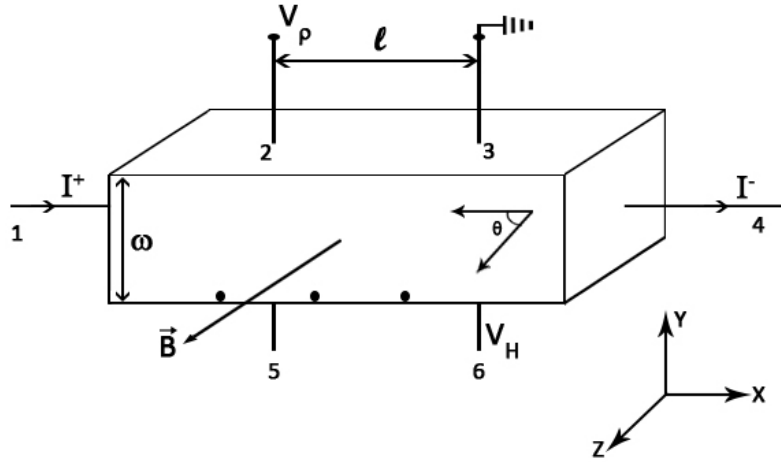


Figure 4.4: A schematic illustration (adapted from [164]) of the Hall effect in a n-type conductive sample. The contact points are numbered in the same manner as with the Hall bar schematic in Figure 4.2.

Equation 4.13 is valid for both electrons and holes. We can write the force for both separately as follows:

$$F_{ey} = -q(E_y + v_{ex}B_z) \quad (4.14)$$

$$F_{hy} = q(E_y - v_{hx}B_z) \quad (4.15)$$

Here, v_{ex} is the velocity of the electrons along the x-direction and v_{hx} is the velocity of the holes along the x-direction. If we now take the total current density in the y-direction of the Hall bar, we get the following expression:

$$J_y = J_{ey} + J_{hy} = qn v_{ey} = qp v_{hy} \quad (4.16)$$

When the Lorentz force and the Coulomb force are in equilibrium, a steady state situation is reached where there is no net current and force in the y-direction.. This gives us the following expressions:

$$E_y = -v_{ex}B_z \quad (4.17)$$

$$E_y = v_{hx}B_z \quad (4.18)$$

$$pv_{hy} + nv_{ey} = 0 \quad (4.19)$$

If we assume that the mobility of the charge carriers is independent of the direction, we can substitute the following drift velocities in the last three equations by $v_{hy} = \mu_h E_y, v_{hx} = \mu_h E_x, v_{ey} = \mu_e E_y, v_{ex} = \mu_e E_x$. This leads to the following expressions:

$$E_y = -\mu_e E_x B_z \quad (4.20)$$

$$E_y = \mu_h E_x B_z \quad (4.21)$$

$$p\mu_h E_y + n\mu_e E_y = 0 \quad (4.22)$$

Next, we can substitute Equation 4.20 and 4.21 in 4.22, which results in:

$$(p\mu_h^2 - n\mu_e^2)E_x B_z = (p\mu_h + n\mu_e)E_y \quad (4.23)$$

If we write down the total current density which flows through the Hall bar along the direction of the x-axis we get equation 4.24.

$$J_x = q(pv_{xh} + nv_{xe}) = qE_x(p\mu_h + n\mu_e) \quad (4.24)$$

If we further define the Hall coefficient as $R_H = \frac{E_y}{J_x B_z}$ and substitute E_y for Equation 4.23 and J_x for Equation 4.24 we get the following relation:

$$R_H = \frac{p\mu_h^2 - n\mu_e^2}{q(p\mu_h + n\mu_e)^2} \quad (4.25)$$

From Equation 4.25 it is clear that the Hall effect is a compensation effect: if $p=n$ and $\mu_n = \mu_p$, no Hall voltage should be detected [165]. The Hall coefficient R_H is dependent on the Since Al:ZnO is a n-type semiconductor we can neglect the hole concentration p since $p \ll n$. If this is taken into consideration, Equation 4.25 simplifies to:

$$R_H = -\frac{1}{qn} \quad (4.26)$$

In an experimental setup, as in Figure 4.2, a constant current I is applied between the contact points 1 and 4. When the magnetic field is turned on, the Hall voltage V_H is measured between contact points 3 and 5. Together with the thickness t of the film, we can calculate the Hall coefficient by $R_H = \frac{V_H t}{IB}$. The value is usually expressed in units of $\frac{m^3}{C}$. From R_H and the already measured resistivity one can calculate the charge carriers density n and the mobility μ as is shown in Equation 4.27 and 4.28.

$$\mu = -\sigma R_H \quad (4.27)$$

$$n = \frac{-1}{qR_H} \quad (4.28)$$

The complete, step by step measurement procedure is described in Chapter 5.2 of the PhD thesis of S. Janssens [166].

4.3 X-ray diffraction

The spectroscopic technique of x-ray diffraction is derived from Bragg's law for crystalline materials. Bragg states that, when there is scattering of x-rays from a crystal lattice, the incident angle (measured between the substrate plane and the source) equals the reflectance angle. Each layer of atoms in a crystalline substrate material reflects a small intensity fraction of the incident x-ray beam. Through a process of constructive and destructive interference, a diffraction pattern is formed. For example, under certain incident angles constructive interference occurs where the path-length difference of wavelets scattered at adjacent crystal planes equals an integer multiple n of the wavelength λ . At these certain angles (θ), a peak can be seen at the XRD spectrogram. An illustration of Bragg's law can be seen in Figure 4.5. The mathematical description is formulated

CHAPTER 4. ELECTRONIC-, STRUCTURAL- AND CHEMICAL CHARACTERIZATION TECHNIQUES

in Equation 4.29, where λ is the wavelength, d is the distance between the crystal planes, and θ the incident and reflectance angle.

$$2d \sin \theta = n\lambda \quad (4.29)$$

The XRD measurements performed in this thesis were carried out with a D5000 diffractometer (Siemens, Germany) in locked-coupled θ - 2θ or rocking-curve geometry around the ZnO peaks. In rocking-curve geometry, the incident angle θ , and the detector angle 2θ are fixed at the Bragg angle. Next, the sample orientation is *rocked* along its equilibrium position. The x-rays, generated by an x-ray tube, are filtered using a germanium single crystal monochromator. The $\text{Cu-K}\alpha_2$ and $\text{Cu-K}\beta$ wavelengths are filtered by the monochromator, leaving the $\text{Cu-K}\alpha_1$ line (1.5406 \AA) to illuminate the sample. The acceleration of the electrons in the x-ray tube was 40 kV with a current of 40 mA. The spectra were taken with a θ - 2θ range from 10° to 100° , a step size of 0.05° and a detection time of 1 s per step size. Four slits were placed in the XRD spectrometer, two for the incident ray (0.6 mm and 1 mm) and two for the reflected ray (1 mm and 0.2 mm). The substrate was fixed onto the sample holder with plasticine. This way, when pressing on the sample, we ensured that the substrate was placed perfectly horizontal.

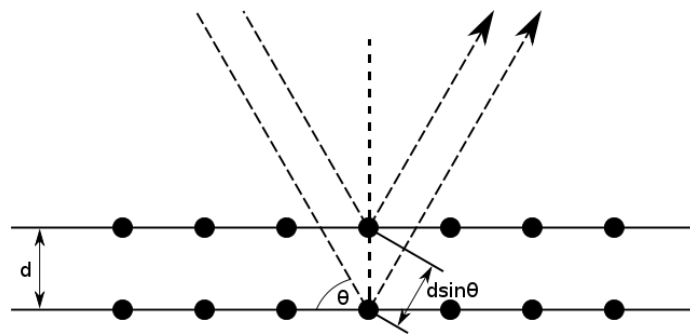


Figure 4.5: A schematic illustration of Bragg's law.

Besides the structural verification of the grown thin films of Al:ZnO, and to compare the crystal quality of the thin films, XRD can also be used

to extract information the crystallite size. For this, the Debye-Scherrer formula is used. In Chapter 3.4, we already used the Debye-Scherrer formula to compare the difference in sintered and non-sintered targets. The Debye-Scherrer formula gives a means to calculate the minimum size of the crystallites in the substrate material. It can also be used on Al:ZnO films, although with a thin film, the estimated crystal size will be a value measured along the z-axis. The Debye-Scherrer Equation 4.30 is formulated as follows:

$$t = \frac{K\lambda}{B \cos \theta} \quad (4.30)$$

Where t is the lower boundary size of the crystallites; λ is the wavelength of the incident x-ray; B is the line broadening of the diffraction peak at the half maximum intensity (FWHM); θ is the Bragg angle. The constant K is a shape factor, which takes in to account the shapes of the crystallites presumed to be in the sample material. The shape factor lies between 0.89 and 1.39. For an unknown crystallite shape however, commonly $K = 0.9$ is assumed [167].

4.4 Electron microscopy

To analyse the surface morphology and structure of the grown Al:ZnO films, Scanning Electron Microscopy (SEM) micrographs were taken from several films which were grown in different sputter gas mixtures. The SEM micrographs can clearly distinguish between the films which were grown in a mixture of Ar and O₂ and those grown in a pure Ar sputter gas. Further discussion on these results is given in Chapter 6, where the different Al:ZnO thin films are compared. The SEM that was used was a FEI Quanta 200 FEG-SEM. Most SEM micrographs of the Al:ZnO films were taken with an electron acceleration of 15 kV. In this energy range, after absorption, secondary electrons and light-quanta are produced. Also, due to the limited acceleration, the majority of the electrons are absorbed in the upper

layers of the substrate material.

A possible solution to these inherent drawbacks of using SEM in visualizing the structure and morphology below the surface of the thin film, to give information on the crystal structure and to quantify the doping of the Al:ZnO, is transmission electron microscopy (TEM). With TEM, the acceleration voltage is increased to hundreds of kV. The sample thickness of a TEM substrate is limited to a few hundred of nanometers. The TEM measurements were performed by the EMAT group (Electron Microscopy for Materials Science, University of Antwerp). For the Al:ZnO thin films, sample preparation was done by a focused ion beam (FIB) lift-out procedure, in a FEI Helios FIB-SEM system. A large range of different characterization techniques were performed including high-angle annular dark field (HAADF) images and energy-dispersive X-ray (EDX) mapping. Experiments were carried out on an aberration corrected FEI Titan 60-300 "cubed" microscope, operated in scanning transmission electron microscopy (STEM) and equipped with a Bruker four quadrant, large solid angle EDX detector. The microscope was operated at 200 kVolts, using a convergence semi-angle of 22 mrad. The inner detection semi-angle for HAADF-STEM imaging was 64 mrad, for ADF-STEM imaging it was 22 mrad, and the angular detection range for ABF-STEM imaging was approximately 11-22 mrad. High resolution TEM imaging was carried out on an aberration-corrected FEI Titan 80-300 "cubed" microscop, operated at 200 kVolt acceleration voltage.

4.5 X-ray photo electron spectroscopy

X-ray photo electron spectroscopy (XPS) is a quantitative spectroscopic technique which is able to measure with high accuracy (parts per thousand) the electronic-, chemical state and composition of the elements of a target material or thin film. XPS spectroscopy relies on the photo-electric effect, first explained by Einstein in 1905. When a material is irradiated by an X-ray beam, free electrons are created at the surface of a substrate

(0 - 10 nm depth) and accelerated to an electron energy analyzer. By measuring the specific amount of electrons and the kinetic energy of the electrons, an XPS spectrum is created and the required information can be extracted. To achieve a high accuracy, the electrons that are accelerated to the detector must not be scattered by gas particles and ions. This means that XPS is a technique which requires a high (10^{-8} hPa) to ultra high vacuum (10^{-9} hPa). Also, XPS can be used to extract information about the complete thickness of thin films by sputter etching through the film layer by layer to obtain an in depth profile. This technique was not utilized on the grown Al:ZnO thin films in this thesis. Because the etching process is a plasma etch, metallic zinc ions will be created by etching away layers of the ZnO film. Since zinc is known for its low vapour pressure (10^{-2} hPa at 300 K) [168], free zinc atoms and ions will contaminate the walls of the vacuum chamber, and this contamination is permanent. For an in depth chemical analysis to quantify the Al doping in the samples, Inductive coupled plasma spectroscopy (ICP) and EDX were performed. However, no difference in Al content was found between the surface and the bulk film. Furthermore, XPS was used to search for trace elements of metallic zinc at the surface of the grown Al:ZnO thin films. The XPS measurements were performed on a commercial PHI 5600 LS photo-emission system (Physical Electronics, Germany) in order to analyze the elemental distribution within the samples. For that purpose, core-level spectra were acquired using monochromatized Al-K X-rays (1486.6 eV, spot size about 1 mm^2) for photoexcitation. These analyses were performed by the Nanos-structure Physics Group withing the IMO institute of Hasselt University.

Part III

Results and discussion

Chapter 5

The growth and properties of Al:ZnO thin films with 2.4 at.% Al

The following chapter is based on the results which are partially published [169] in *Physica Status Solidi a*, volume 210, issue 5, pages 1013-1018 (2013), with the title:

"Preparation of epitaxial films of the transparent conductive oxide Al:ZnO by reactive high-pressure sputtering in Ar/O₂ mixtures" by M. Van Gompel, B. Conings, K. L. Jiménez Monroy, J. D'Haen, K. Gilissen, M. D'Olieslaeger, M. K. Van Bael and P. Wagner.

5.1 Sample preparation

The films grown with an atomic Al percentage of 2.4 % compared to Zn, were used as a proof of concept to test the design of the sputtering setup. As mentioned in Chapter 3, where the sputter target fabrication was discussed, the first targets which were used to optimize the sputter process were made with as delivered Zano powder . No other ceramic materials were added. This made sure we did not start with too many variables in the complex process of thin film deposition.

For the sputtering of Al:ZnO, different deposition parameters were tested to obtain an optimal result. Pressure, gas mixture, distance between target and substrate, the growth temperature were varied. The guideline to determine whether the chosen parameters improve film quality, were the optical appearance and sheet resistivity. The preferred optical appearance is a *shiny* and *smooth* film as a first indication for morphological quality. This parameter is relevant in most applications where Al:ZnO is used for its high optical transmittance. Second, the sheet resistance was measured with a van der Pauw setup in order to obtain a first indication for the conductive properties. The optimization of the first two sputter parameters, total pressure and gas mixture, were done simultaneously. The total pressure was varied between 1×10^{-1} hPa and 3 hPa, above 3 hPa, arcing became unavoidable. Especially, sputtering in a pure O₂ plasma did not give a stable discharge due to arcing, which occurred already at currents of just 15 mA. The formation of a thin, insulating oxide layer on the ceramic target is a possible explanation [120]. For the growth of the thin film in an oxygen rich sputter-gas environment, the optimal mixture between O₂ and Ar was found to be $P_{Ar} = 2.0$ hPa and $P_{O_2} = 1 \times 10^{-2}$ hPa, which corresponds to a 0.05 O₂:Ar ratio. Increasing the amount of O₂ above 0.5 % leads to an unstable growth process. To remove a possible excess of adsorbed oxygen, resulting in enhanced resistivity values, the films were post-annealed at growth temperature under an Ar pressure of

2.0 hPa for 30 minutes.

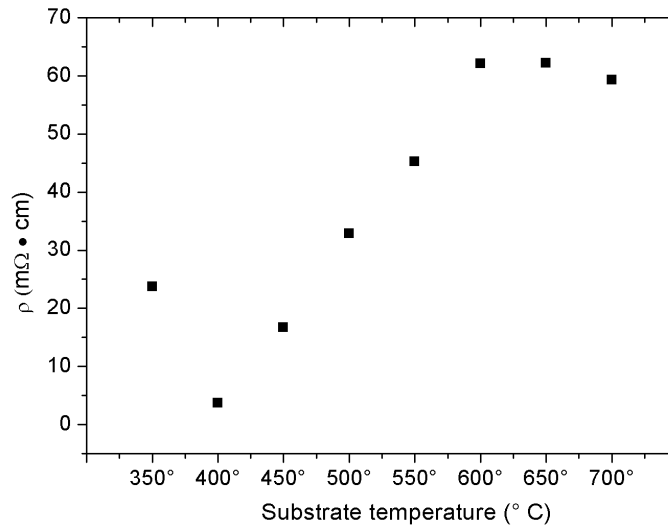


Figure 5.1: Optimizing the resistivity of Al:ZnO films as a function of the growth temperature. All films had a thickness of 90 nm and were sputtered under Ar and O₂ partial pressures of 2 hPa and 1×10^{-2} hPa respectively.

In Figure 5.1, the resistivity is plotted as a function of the growth temperature for the films grown in the Ar/O₂ mixture. We note that growing in pure argon at the mentioned temperatures in Figure 5.1 did not result in a stable and homogeneous film. In the next generation of films, with a lower Al doping percentages, we will focus on lowering the temperature to the utmost minimum. This is done by growing films with a homogeneous thickness in pure Ar sputter gas. Also, this means that for practical applications, one of the disadvantages of growing with vacuum techniques, namely the need of high deposition temperatures, is brought down to a minimum

As a result, for the first generation of thin films, all samples were deposited in the standard atmosphere of the argon-oxygen mixture under continuous gas flow. Films grown at around 400 $^{\circ}C$ exhibit the lowest resistivity; deposition temperatures above 500 $^{\circ}C$ resulted in opaque films and the

optical transmittance diminishes. Below 300 °C, the resistivity increased for these highly doped films and did not have a *shiny* and homogeneous appearance.

5.2 Structural and chemical characterization

In Figure 5.2, the XRD 2θ -scan of an Al:ZnO film grown on sapphire is shown. The characteristic Al_2O_3 peaks of the substrate at $2\theta = 41.6^\circ$ and $2\theta = 90.7^\circ$, the (0006) and the (00012) plane respectively, are clearly visible. The XRD 2θ -scan of the Al:ZnO thin film with optimal transparency

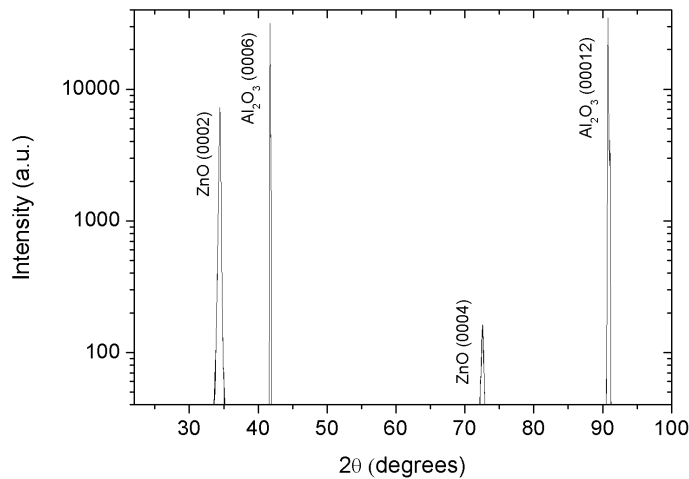


Figure 5.2: XRD 2θ -scan of a 90 nm thick Al:ZnO film deposited at 400 °C under Ar and O_2 partial pressures of 2 hPa and 1×10^{-2} hPa respectively. The Al:ZnO film has a strong c-axis orientation while the peaks at $2\theta = 41.6^\circ$ and $2\theta = 90.7^\circ$ originate from the sapphire substrate.

and low resistivity grown at 400 °C, shows the (0002) peak of c-axis oriented ZnO at $2\theta = 34.34^\circ$ and the (0004) peak at $2\theta = 72.58^\circ$, while no other phases or crystalline orientations are visible. Although the lattice mismatch between c-axis sapphire ($a = 0.4758$ nm and $c = 1.299$ nm) and ZnO ($a = 0.3249$ nm and $c = 0.5207$ nm) is large, epitaxial growth of ZnO

on sapphire still seems to be feasible according to literature [170–172]. However, final conclusions on the in-plane orientation of the ZnO lattice with respect to the underlying substrate can not yet been drawn.

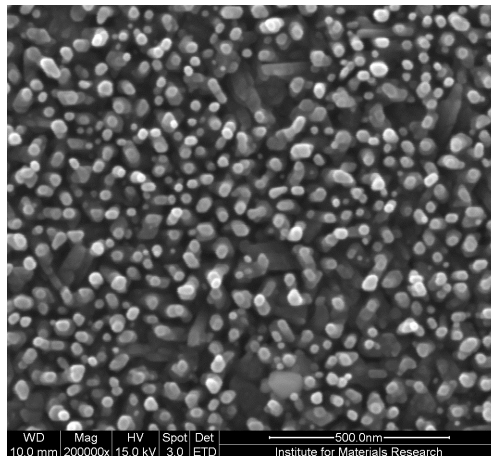


Figure 5.3: SEM micrograph of an Al:ZnO film grown at 400 °C. The scale bar has a length of 500 nm.

Figure 5.3, reveals that the film is composed of closely packed, wire shaped crystallites. The typical grain size of crystallites in the substrate plane is ± 40 nm. The AFM image in Figure 5.4, shows a roughness of approximately 10 nm (root mean square) for the film while the substrate roughness was 3 nm (rms), both determined over an area of $45 \times 45 \mu\text{m}^2$. This roughness may be attributed to the fact that the film is grown as a composition of densely packed crystallites with a preferred growth direction along the c-axis. Also, growing

Although the ratio of Al and Zn atoms in the target is 2.4 at.% Al/Zn, the ratio of Al- and Zn-atoms in the films is not known beforehand. This ratio can be measured with XPS using the Shirley algorithm, giving an indication of the overall aluminum content. We note that there are in principle three possible doping sites available as shown in Figure 1.10. The XPS spectrum in Figure 5.5 is measured at the surface of the Al:ZnO film and the information depth is 5 nm. The spectrum shows that the amount of Al

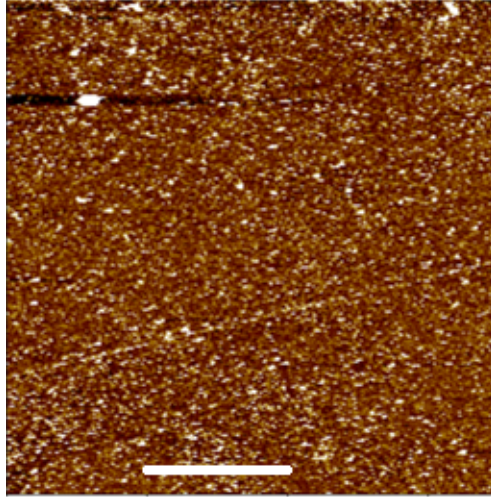


Figure 5.4: AFM image of an Al:ZnO film grown at 400 °C. The scale bar has a length of 10 μ m.

present in the film is equivalent to the 2.4 at.% Al/Zn ratio already present in the sputtering target. This way, we can conclude that the stoichiometry of the target and the film are identical within the experimental resolution. No major pollutants or adsorbates were detected in the XPS spectrum.

5.3 Electronic characterization

Resistivity (ρ), mobility (μ) and the density of charge-carriers (n) were measured using a Hall-bar configuration. Both measurements were performed on the same Al:ZnO film which was grown at a temperature of 400 °C, at a pressure of 2.0 hPa Ar and 1.5×10^{-1} hPa O₂. The temperature dependence of the resistivity, shown in Figure 5.6, indicates a semiconducting behaviour. The temperature dependence of the resistivity was fitted empirically with the equation $\rho(T) = \rho_0 - \alpha T$. This fit yields $\rho_0 = 0.027 \Omega \cdot \text{cm}$ and $\alpha = 2,1 \times 10^{-5} \frac{\Omega \cdot \text{cm}}{\text{K}}$ with $R^2 = 0.99252$. We note that this fitting function for ρ is applicable because we measured in the linear part of the temperature dependency of ρ . If the temperature is further increased to

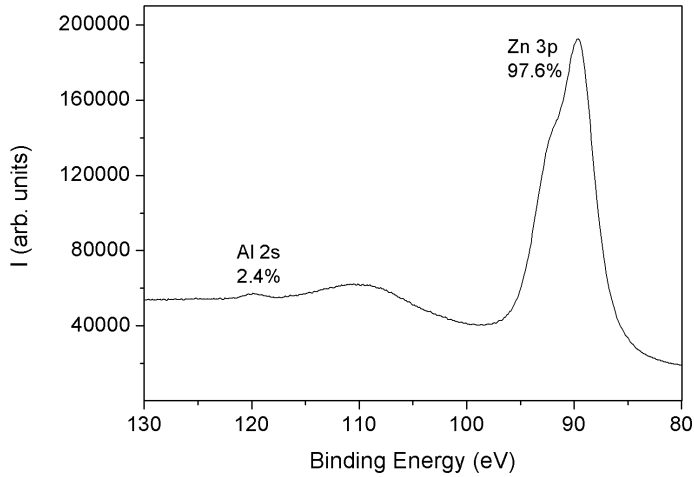


Figure 5.5: XPS spectrum with the binding energy of the Zn 3p and Al 2s orbitals.

above 400°C, the exponential relation $\rho \propto e^{\frac{-E_g}{2kT}}$ can be used to fit $\rho(T)$. This way it is possible to estimate the electronic bandgap E_g of the semiconductor [80]. Although Al:ZnO films with lower resistivity have been achieved (see Table 1.3), the values are comparable to previous work, when taking the high doping level into account [173]. A possible explanation is the formation of the aluminum-rich ZnAl_2O_4 spinel phase which has a large resistivity and in turn also decreases the carrier mobility [174]. However, we point out that there are no indications for the spinel phase in the x-ray scan shown in Figure 5.2. Also, the number of charge carriers $n = 4.8 \times 10^{19}$ per cm^3 is close the calculated Mott criterion in Section 1.2.2. This can explain why these films are having semiconducting characteristics.

The mobility data and charge-carrier density results are presented in Figure 5.7 and the mathematical relation $\mu_n = (Nq_n\rho)^{-1}$ was used to calculate n . The number of charge carriers is widely constant within a broad temperature range from 75 K to 400 K. This indicates that there are no structural- or electronic phase transitions present. The absolute density of carriers

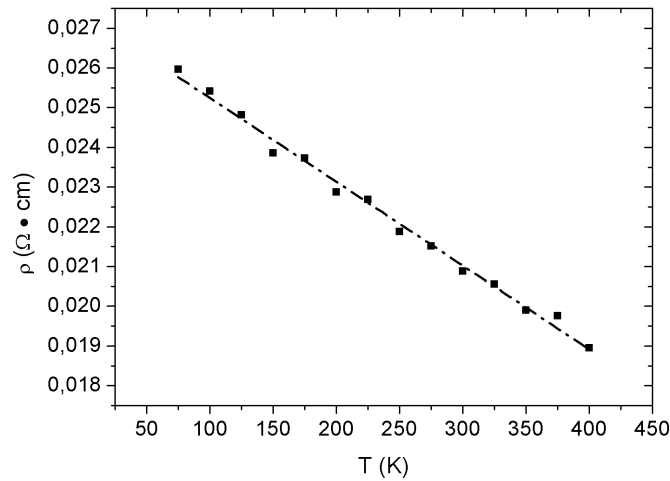


Figure 5.6: Resistivity measurement on an Al:ZnO film grown under optimized sputtering conditions. The dashed line is a linear fit with $\rho_0 = 0.027 \text{ } \Omega\cdot\text{cm}$, $\alpha = 2.1 \times 10^{-5} \text{ } \Omega\cdot\text{cm}/\text{K}$ with an R^2 value of 0.99.

is lower compared to reference values summarized in Table 1.3: With a doping percentage of 2.4 at.% Al, we estimate the number of Al atoms to be 9.97×10^{20} per cm^3 . This number, together with the experimentally determined charge carrier density of 4.8×10^{19} per cm^3 yields to a doping efficiency of 4.8%. This low efficiency can be attributed to either the formation of inclusions such as the Al-rich spinel phase or to a trapping of charge carriers at grain boundaries visible in SEM micrograph in Figure 5.3. However, it is noteworthy that the electron mobility of the Al:ZnO thin film rises with increasing temperature. According to Matthiessen's rule [175] which was discussed in Chapter 4, the mobility is dependent on phonon scattering and impurity scattering. The impact of phonon scattering on the mobility is proportional to temperature, while the contribution of impurity scattering should be temperature independent. Due to the high doping, the effect of phonon scattering is probably too small in comparison to the effect of impurity doping. Therefore, measurements in extended temperature ranges would be needed to distinguish clearly between these possi-

ble scattering mechanisms. The highest mobility found with our samples is $6.8 \text{ cm}^2\text{V}^{-1}\text{s}^{-1}$ at 400 K, being in the same range as literature data for the same doping level (see Table 1.3). A similar, unusual increase of the mobility with increasing temperature has been reported earlier for organic conductors and was explained in a model where charge transport is governed by trapping and thermally-induced release of carriers at localized states in grain boundaries [176]. Further investigation in this mechanism can be done by growing films which are, according to literature mentioned in Chapter 1, in an Al doping level of 1 at.% and grown in pure argon. In principle this should result in films which show the complete metallic behaviour expected from standard TCO layers.

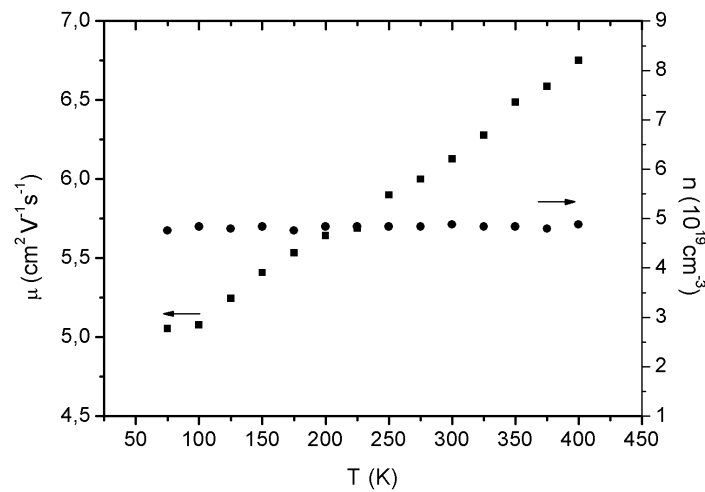


Figure 5.7: Hall measurement of an Al:ZnO film grown under optimal sputtering conditions. The solid squares indicate the mobility (left axis) while the carrier concentration is given by solid dots (right-hand axis).

5.4 Optical characterization

Transparency measurements by UV-Vis absorption spectroscopy, see Figure 5.8, were done on Al:ZnO films grown on borosilicate glass. Measurements on films grown on sapphire were not possible due to the unpolished backside of the sapphire substrates. These results reveal a transparency of up to 96% at 430 nm, which is equivalent compared to literature, where values of 85 % 90% are measured, but with a larger film thickness of 250 nm [177, 178]. Nevertheless, this result is promising for future applications of the sputtered Al:ZnO film in devices such as organic LEDs and solar cells.

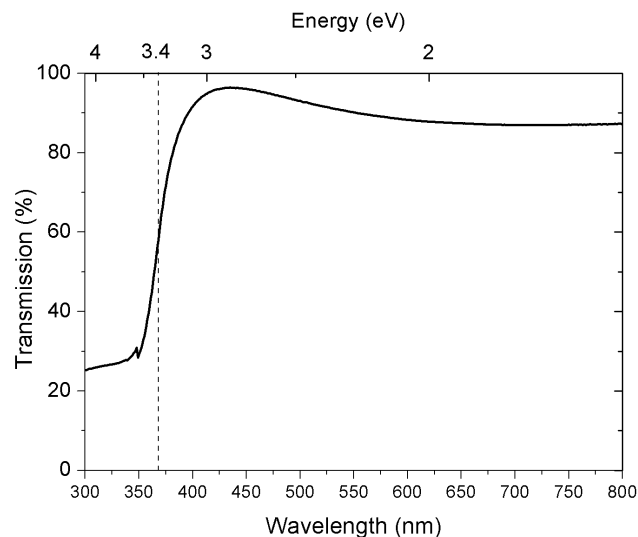


Figure 5.8: Optical transmission measurement of an Al:ZnO thin film with a thickness of 100 nm grown on glass at 400 °C. The optical bandgap is estimated to be approximately 3.4 eV. After a maximum transparency at a wavelength of 430 nm, it decreases marginally in the near infrared (NIR) due to free carrier absorption. In collaboration with K. Gilissen IMO-ONE₂

Chapter 6

The growth and properties of Al:ZnO thin films 1 at.% Al

6.1 Why dope with 1 at.% Al?

As mentioned in Chapter 1, the preferred substitution of Al in the ZnO crystal structure is the tetrahedral position where it substitutes Zn. However, this substitution can be difficult to achieve due to the large difference in ionic radius (88 pm for Zn^{+2} and 67,5 pm for Al^{3+} [179], the different oxidation state and the preference of coordination [109]. Because of this, the solubility level of the Al^{3+} in the ZnO crystal structure is very low. There are several techniques which can be used to characterize the maximum solubility of Al in powdered ZnO. The prevalent techniques are detection by X-ray diffraction where the solubility limit was estimated at 2 at.% Al [180]. A higher doping percentage resulted in a $ZnAl_2O_4$ spinel peak in the XRD scan. Another method which can be used on powdered Al:ZnO is electron diffraction: Kim et.al detected the spinel phase through the use of TEM imaging at a doping level of 1 at.% Al [181]. This value

disagrees with the results obtained by XRD, where ZnAl_2O_4 was not detected up to a doping level 2 at.% Al or higher [180]. This means that the solubility limit of 2 at.% Al as determined by x-ray diffraction might be an overestimation. The use of Nuclear Magnetic Resonance (NMR) on isotope ^{27}Al , is a more direct characterization technique to detect the local Al at the atomic level, compared to XRD and electron diffraction. Tsubota [182] gives an Al^{3+} solubility limit of 0.005 at.% Al, considerably lower than the previously mentioned methods. The large statistical spread of measured values of solubility of Al in ZnO makes it difficult to estimate an optimum doping value for sputtering a thin film. The values given are all for ZnO powder, correctly quantifying the Al percentage present in a doped ZnO thin film will be substantially more difficult. There is however a more indirect way to estimate the limit of solubility in Al:ZnO thin films. When Al replaces a Zn atom at the tetrahedral position in the ZnO wurtzite structure, a free charge carriers (electron) is created.

The ultimate goal is to find the doping limit upon which the films undergo the Mott transition, as explained in Chapter 1 and have metallic behaviour in respect to $\rho(T)$. When overdoping the ZnO thin films with Al, the measured values of mobility and conductivity will be influenced adversely because of the increase in impurity scattering and occurrence of isolated regions associated with the spinel phase. Also, increased lattice stress could influence the crystallite size, and have an indirect deteriorating effect on the electronic properties due to the enhanced scattering at more numerous grain boundaries. Several groups report an optimum Al content of 1 % at, which is clearly higher compared to the direct characterization of the solubility limit in powders by ^{27}Al NMR [183–185]. A possible explanation could be that parameters which are important for thin film growth raise the solubility level of Al in ZnO. This can be attributed to the high energy used during the growth process (either heat or plasma) or for example a low or almost vanishing oxygen partial pressure during growth [109]. Another advantage to keep the level of Al doping in a the range of 1 at.

%, is a decrease of IR absorption in thin films compared to higher doping levels. When a ZnO thin film is doped with a lower at.% of Al, the number of charge carriers also diminishes slightly. The higher mobility which can be obtained in films with a lower doping level also reduces the IR absorption [186]. This is an important factor when the thin film is used in solar cells, where it is crucial to maximize the bandwidth which can be absorbed from the solar spectrum by the photoelectric material [183]. In case of our thin film samples, see Table 6.1, two analytical techniques confirm that the aluminium percentage is indeed close to the expected value of 1 at.%. The measurement of the Al presence by ICP was performed on Al:ZnO films that were deposited on Si, otherwise Al contamination from the sapphire substrate could not be avoided.

Table 6.1: Measuring Al content in doped ZnO thin films. The films measured with ICP were grown on Si instead of sapphire.

Target	Film	Technique	Measured doping level
2.4 at.%	Ar/O ₂	XPS	2.4 at.%
1 at.%	Ar	ICP	0.7 at.%
1 at.%	Ar/O ₂	ICP	0.9 at.%
1 at.%	Ar	EDX	1.4 at.%
1 at.%	Ar/O ₂	EDX	1.4 at.%

6.1.1 Deposition in Ar/O₂ mixtures (Type I)

In Chapter 5, we described the growth the first Al:ZnO films with a doping percentage of 2.4 at.% as a proof of principle of the performance of the sputter reactor. As mentioned above, we are now focusing on ZnO films with a lower doping rate of 1 at.%. From Chapter 5 we have also drawn the conclusion that the sputtering process with the homemade targets is very sensitive to oxygen. This was deduced by the substantial increase in

the voltage of the current upon increasing the partial pressure of oxygen in the deposition chamber. A possible explanation is the formation of an undoped oxide layer on the target, which in turn increases the resistance of the target surface [120]. To compare films which have been sputtered in an Ar/O₂ mixture as the previous chapter, and films which have been grown in a pure Argon sputter gas we have to change the growth temperature. This is because growing a film in pure Argon did not result in a film at a substrate temperature of 400 °C. To concentrate on the difference in film properties with respect to the applied sputter gas, we choose a growth temperature of 250 °C. The optical properties of the films are, to the naked eye, still *shiny* and *smooth*. Also, minimizing the growth temperature has other advantages beside the possibility to grow in pure Ar. Alternative substrate materials can be used in the future. For example, plastic materials with a high melting temperature, such as teflon, can become an option.

The sputter parameters of the films produced in Ar/O₂ mixtures, are shown in Table 6.2. After the chamber is pumped down over night, the pressure is below 1×10^{-6} hPa. This is enough to ensure pure films without trace amounts of impurities. Both, current and Ar pressure, have to be increased in small steps to ensure a stable plasma. A large power increase can damage the target when it has not yet reached a stable temperature. Since the target was in contact with ambient atmosphere in between the growth of two films, contamination of the target surface is a possibility. Therefore, we performed these pre-sputtering step to achieve a stable plasma at growth parameters for at least 30 minutes. This way, contamination at the target surface is removed. When a stable plasma is reached at a current of 80 mA and and Ar pressure of 2 hPa, the power supply maintains a voltage of 380 ± 20 V, producing a power of 30.4 W. Controlling the amount of oxygen that is added to the sputter gas was done by monitoring the voltage variation of the power supply. This was necessary due to fluctuations in pressure measured by the capacitive gauge. Oxygen was added until the power supply had an output of 80 mA at ± 440 V. On av-

erage this amounts in an addition of $1 - 5 \times 10^{-3}$ hPa measured by the capacitive gauge. We point out that such small pressure changes are at the limit of the gauge's precision. The substrate can now be turned towards the plasma and the sputter deposition starts. By means of AFM, the thickness of the films is measured to be 110 nm for a deposition time of 2 hours. This results in an average sputter rate of 55 nm/h. After growth, the films are annealed in an Ar atmosphere at growth temperature for 30 minutes, After which there are cooled down to room temperature within 60 minutes.

Table 6.2: Deposition parameters for the deposition in Ar/O₂ mixtures: type I films.

Starting pressure	$<1 \times 10^{-6}$ hPa		
Growth parameters			
P_{Ar}	2.000 hPa		
P_{O_2}	$1-5 \times 10^{-3}$ hPa		
P_{total}	± 2.001 hPa		
Substrate temperature	250 °C		
Current	80 mA	Voltage	380 V → 440 V
Time	2h	Deposition rate	55 nm/h

After growth, both SEM micrograph and XRD scans were used to characterize the quality of the grown Al:ZnO thin films. From XRD, the same conclusions could be drawn as with the films doped with 2.4 at.%. Only the (0002) peak of ZnO and the peaks of the sapphire substrate are observed. Figure 6.1 depicts a micrograph with a magnification of 20000×. The image shows a crystalline and homogeneous film, and compared to the films with a higher Al-doping percentage, the film now consists of larger crystallites, compared to the wire-shaped growth that was seen in Figure 5.3. A larger magnification, focused on the hexagonal crystallites, is shown in Figure 6.2. Here, the average size of a single crystallite is estimated to be around 400 nm. In the center of each hexagonal crystallite, a seeding

point for growth is visible. However it is clear that the film is polycrystalline.

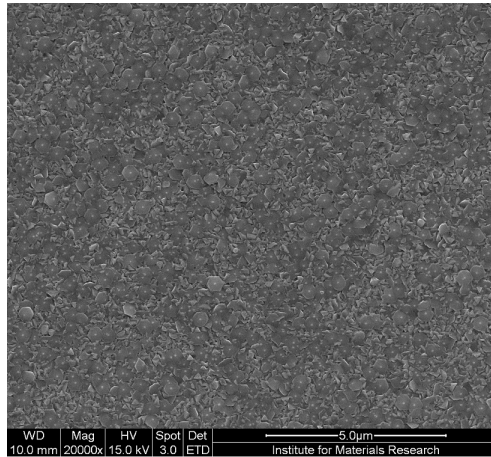


Figure 6.1: SEM micrograph of a film grown in an Ar/O₂ gas mixture and with an Al-doping percentage of 1 at.%.

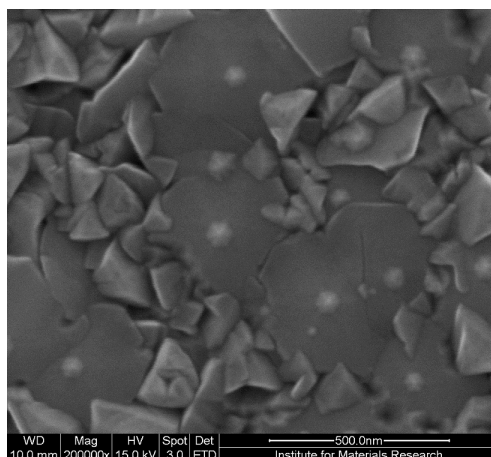


Figure 6.2: SEM micrograph of a film grown in an Ar/O₂ gas mixture and with an Al-doping percentage of 1 at.%. The magnification is 200000x. Seeding points for growth of the crystal are seen in the center of the hexagonal crystallites.

6.1.2 Film growth in pure Argon (Type II)

As mentioned in the Chapter 1, the presence of oxygen has a major effect on both the structural, optical and electronic properties of Al:ZnO thin films. In literature, an increase of the oxygen pressure during film deposition has a profound negative effect on the maximum value of the mobility and conductivity [187,188]. And an ideal range between 10^{-4} hPa to 10^{-3} hPa has been reported [105]. However, this ideal value strongly depends on the method of deposition and on how the O_2 partial pressure is determined. Others report high mobility and conductivity for films sputtered in pure Argon [183]. The films grown in an Ar/ O_2 mixture with a doping percentage of 2.4 at.% Al and 1 at.% Al still have non-metallic electronic behaviour, which is mentioned in Section 5.3 and Section 6.3. When growing in pure Ar, the stoichiometry of the Al:ZnO film, should in principle be identical to the Al:ZnO target, since the oxygen atoms and ions do not originate from the gas which has a very high purity. However, a small deficiency of oxygen must be anticipated.

Table 6.3: Deposition parameters for the deposition in pure Ar: type II films

Starting pressure	$<1 \times 10^{-6}$ hPa		
Growth parameters			
P_{Ar}	2.000 hPa		
P_{O_2}	0 hPa		
P_{total}	± 2.000 hPa		
Substrate temperature	250 °C		
Current	80 mA	Voltage =	380 V
Time	2h	Deposition rate =	110 nm/h

In Table 6.3, the growth process of the thin film deposition for growth in a pure Ar medium is shown. As before, the starting pressure is below 1×10^{-6} hPa. The deposition parameters are retained compared to the

Ar/O₂ mixture thin films. We mention that by not adding oxygen, the supplied current can be sustained at a lower constant voltage of 380 V. After growth, the films are annealed in an Ar atmosphere at 250 °C for 30 minutes. Next, the substrates are cooled down to 50 °C before exposing the Al:ZnO films to ambient air.

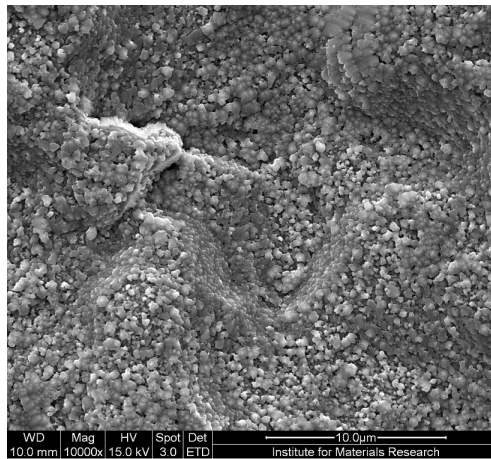


Figure 6.3: SEM micrograph of Al:ZnO films grown in pure Ar and with an Al-doping percentage of 1 at.%. The films grown in pure Ar do not show any hexagonal structures at this magnification.

Since these Al:ZnO films are grown with a possible stoichiometric deficiency of oxygen, care has to be taken that there is no metallic Zn present to form a coalescent conducting network in the thin film. This would mean that, when performing the electronic characterization, we would also measure the metallic network, instead of the electronic properties of the ceramic thin film itself. Also, if metallic zinc is present, the Al:ZnO film would lose transparency and would show a green hue [7]. At least optically, no green hue was detected. Further imaging with EDX mapping could be indispensable in detecting the possible presence of an undesired coalescent Zn network. These will be analyzed in Section 7.2. The SEM micrographs of the films grown in pure Ar, look distinctly different compared to Figure 6.1 and 6.2. Instead of the hexagonally shaped crystals we detected in abundance before, the film surface is now much more erratic. Also in

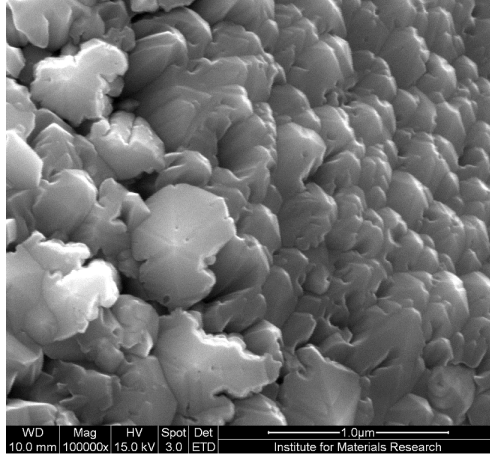


Figure 6.4: SEM micrograph of Al:ZnO films grown in pure Ar and with an Al-doping percentage of 1 at.%, at a larger magnification the films show hexagonal shaped crystallites compared to Figure 6.3.

Figure 6.3, the film roughness appears to be larger compared to the film grown in the Ar/O₂ mixture. If we take a larger magnification, see Figure 6.4, we can still distinguish some smaller hexagonal shaped crystals. This proves that the film is indeed polycrystalline and not amorphous. Further information on the crystallinity of the film can be extracted with XRD. The XRD θ -2 θ scan in Figure 6.5 clearly indicates only the (0002) growth direction of the ZnO crystals as with Ar/O₂ mixture films.

6.1.3 Deposition of layered films with selected gases (Type III)

To mitigate the "chaotic" structure of the films grown in pure Ar, but keep the potentially better electronic properties of these films compared to the films grown in an oxygen-containing gas mixture, a bilayer film can be a solution. This idea is as follows: first, a thin Al:ZnO layer is deposited in a mixed Ar/O₂ atmosphere to obtain a base layer with well-defined crystalline order. Second, a thicker capping layer is prepared by sputtering in pure argon. This layer, with advantageous electronic properties is ex-

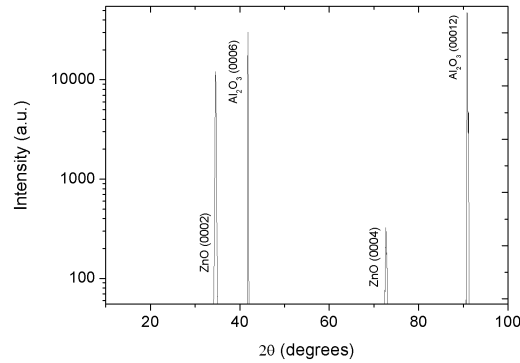


Figure 6.5: θ - 2θ scan of Al:ZnO films grown on sapphire, in pure Ar and with an Al-doping percentage of 1 at.%. No traces of other growth directions than the (0002) orientation were detected.

pected to take over the high crystalline order of the base layer. The growth parameters of such a layered film can be seen in Table 6.4.

Again, the same pre-sputtering procedure is followed to increase the Ar partial pressure to 2 hPa with the power supply delivering a constant current of 80 mA at a voltage of 380 V. When P_{Ar} and V are stable, we lower the current to 60 mA. This means that we can keep the voltage at a maximum value of 420 V during growth. This way the voltage difference during growth between the layers is minimized. A side effect is the lower sputter rate, 50 nm/h compared to 55 nm/h. The growth of the Ar/O₂ seeding layer lasts for 30 minutes. After this, the oxygen flow is reduced gradually until the all-metal dosing valve is closed. The supplied current of the power supply is now increased again to 80 mA and the film growth continuous for 1 hour in pure Ar. The surface of the resulting film in Figure 6.6 is, compared to the film grown in pure Ar, clearly more homogeneous. Also in Figure 6.6, the hexagonal crystallites are more pronounced and thus compare favorably to Figure 6.4. Electronic characterization will give more information on the differences in the resistivity and mobility values of these layered films.

CHAPTER 6. AL:ZNO THIN FILMS WITH 1 AT% AL

Table 6.4: Deposition parameters for the thin film growth in selected gases. The first layer is an Ar/O₂ mixture seeding layer, followed by a layer grown in pure Ar: type III films.

Starting pressure =	1×10^{-6} hPa
Growth parameters	
P_{Ar}	2.000 hPa
P_{O_2}	5×10^{-3} hPa
P_{total}	± 2.005 hPa
Substrate temperature	250 °C
Current	80 mA \rightarrow 60 mA \rightarrow 80 mA
Voltage	380 V \rightarrow 420 V \rightarrow 380 V
Time	0.5h \pm 1 h
Deposition rate	50 nm/h \rightarrow 110 nm/h

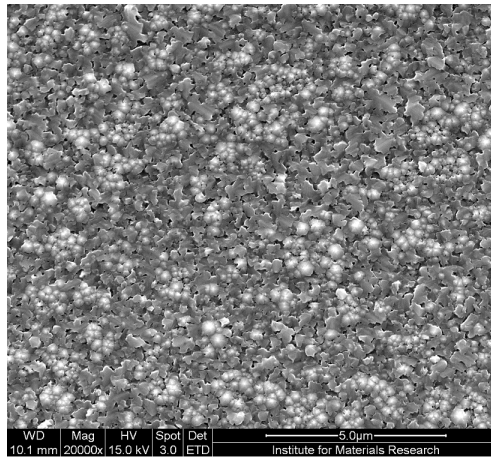


Figure 6.6: SEM micrograph of bilayer Al:ZnO films, with an Al-doping percentage of 1 at.%. Compared to Figure 6.3, the films appears less rough. This could be an explanation for the better transparency of the bilayered Al:ZnO thin films as shown in Table 6.5

Another important parameter for device fabrication with TCO layers, is

their optical transparency. In Section 5.4, an optical transmission spectrum is shown for a film grown in pure oxygen. When we compile the data of the films grown with a doping percentage of 1 at. % we can make a comparison between the films grown in an Ar/O₂ mixture, in pure Ar and layered growth Ar/O₂ ± Ar. The transparency of the layered films (86%) is almost as high as with the samples deposited in Ar/O₂ mixture (96 %) and considerably better than in case of the films deposited in pure argon, which achieve a transparency of less than 65 %. The data in Table 6.5 clearly show the large advantage of the layered films compared to the films grown in pure Ar.

Table 6.5: Average transparency in percent, measured over the visual light spectrum (390 - 700 nm). All three films were grown on a transparent borosilicate substrate with a film thickness of 100 nm.

Sputter gas	Average transparency
Ar	64.7%
Ar/O ₂	90.8%
Ar/O ₂ → Ar	86.0%

6.2 Morphological characterization by scanning transmission-electron microscopy

Since the type II film is grown in pure argon, and the bilayered type III film has a top layer sputtered with pure argon gas, it is necessary to verify that there are no metallic zinc networks present in these film. We noted in Chapter 4.4 that high resolution transmission electron microscopy is an ideal method to search for any presence of metallic zinc in the film. A bilayered film was grown, with a seeding layer of 50 nm thick, and an Ar grown capping layer of 150 nm, yielding a film thickness of 200 nm. The samples were prepared for TEM and STEM analyses by FIB milling. A

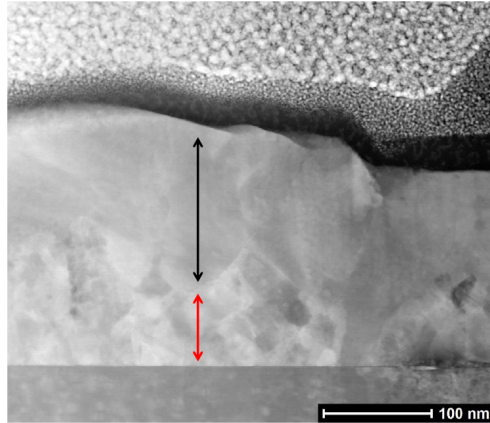


Figure 6.7: The bilayer growth of an Al:ZnO thin film is clearly seen in the Cross-sectional ADF-STEM image (annular-dark field scanning transmission-electron microscopy) micrograph. The first layer (red arrow) was grown in a mixture of Ar and O₂ as sputter-gas. The capping layer (black arrow) was grown with a pure Ar plasma.

clear separation between the two different layers can be seen in the ADF-STEM micrograph in Figure 6.7. Here, the thickness of the layer grown in an oxygen-argon mixture is 55 nm, with a top-layer of 150 nm, in good agreement with the estimated growth rates of both film types. However, it is clear from Figure 6.7, that the average grain size of the seeding layer is smaller compared to the average grain size of the capping layer.

In Figure 6.8, an epitaxial layer of Al:ZnO, deposited on a (0002) oriented sapphire substrate is shown. Small crystal defects can be detected, a grain boundary is visible. To investigate any indication of metallic zinc agglomerates or the formation of a metallic network, an EDX mapping was performed on a type II film that was deposited in pure Ar gas, resulting thus theoretically in an insufficient oxidation of the metallic elements

From the EDX mapping in Figure 6.9, a homogeneous distribution of Zn atom species is identified. This rules out any indication of Zn conglomerates or networks, which could mask or falsify the intrinsic electronic transport properties characterization in Chapter 6.3. Another important

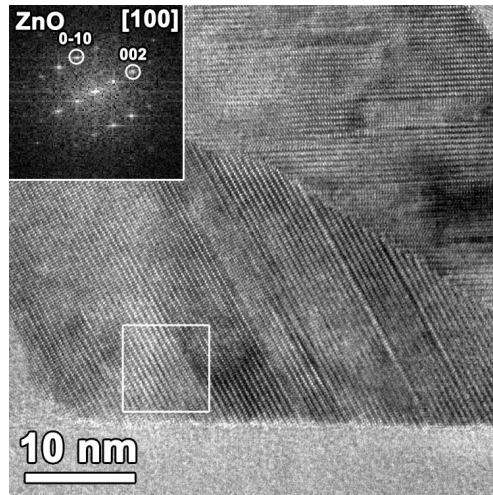


Figure 6.8: HR-TEM micrograph of an Al:ZnO thin film grown in pure Ar sputter-gas, with 1 at.% Al.

result from Figure 6.9, is that no clear Al enrichment was found in any part of the layer. This is due to the low doping level of 1 at.% and the homogeneous distribution of the Al atom species in the film. If this would not be the case, it could be possible that we would see Al enrichment along the grain boundaries of the Al:ZnO film. Doping with 1 at.% Al is still below the solubility limit for the ZnO lattice, as discussed in 6.1 and now also confirmed by our data. Therefore, we can safely assume that the aluminium is homogeneously distributed over the lattice although we can still not conclude that the aluminium is substituted on Zn sites.

6.3 Electronic transport measurements

6.3.1 Deposition in Ar/O₂ mixtures

The resistivity of the films grown in an Ar/O₂ mixture is shown in Figure 6.10 for a representative sample and the resistivity decreases with rising temperature, this semiconductive behaviour is similar to the samples with 2.4 at.%, discussed in Chapter 5.3. If we assume that every

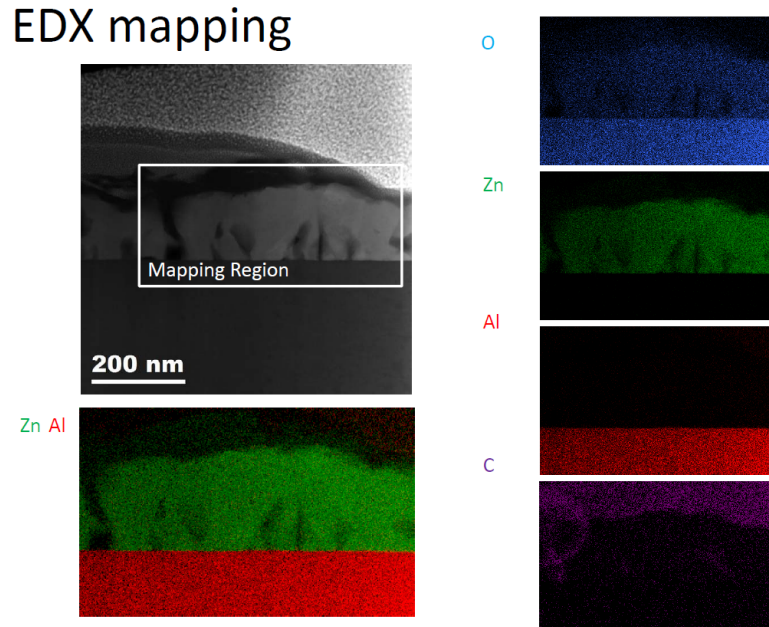


Figure 6.9: EDX mapping of an Al:ZnO thin film grown in pure Ar sputter-gas, with 1 at.% Al.

Al^{3+} ion introduces 1 negative charge carrier in the ZnO lattice, then doping the film with 1 at.% would introduce a charge carrier density of $4.1 \times 10^{20} \text{cm}^{-3}$. The films are thus doped above the Mott criterion for ZnO, ($1.2 \times 10^{19} \text{cm}^{-3}$), which should ensure a behaviour on the metallic side of the metal-insulator transition. From Figure 6.11, we can conclude that the number of charge carriers is constant with temperature at $5 \times 10^{20} \text{cm}^{-3}$. A constant number of charge carriers is again an indication that the film has in fact undergone a Mott transition [80, 189].

We propose that the semiconductive behaviour of $\rho(T)$ is linked to the low density of oxygen vacancies [190]. This is due to the presence of oxygen gas during the thin films growth. However, another possibility is that excess oxygen ions, interstitially incorporated in the ZnO lattice can act as electronegative impurity. Oxygen has a strong electronegativity, which could in turn trap electron charge carriers [7]. The semiconductive

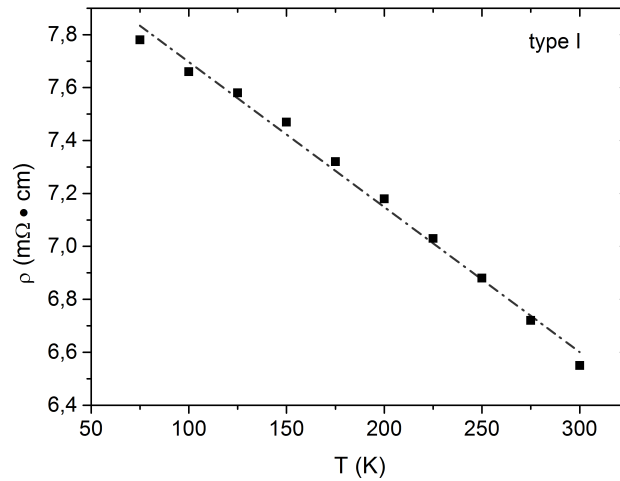


Figure 6.10: Resistivity measurement of a film grown in an Ar/O₂ gas mixture and with an Al-doping percentage of 1 % at. The dashed line is a linear fit with Equation 6.1, where $\rho_0 = 8.25 \text{ m}\Omega\cdot\text{cm}$ and $\alpha = 5.48 \times 10^{-2} \text{ m}\Omega\cdot\text{cm}/\text{K}$ with an R^2 value of 0.99.

behaviour of the Al:ZnO films grown in an Ar/O₂ mixture can, as previously put in Chapter 5.3, be fitted by an empirical linear Equation 6.1. Again, the linearity of the equation only valid in the limited temperature range that was measured.

$$\rho(T) = \rho_0 - \alpha T \quad (6.1)$$

In Figure 6.11, it is clear that the behaviour of mobility and charge carrier density with temperature follows the same metallic like mechanism as described in Chapter 5.3, where it was concluded that due to high doping, the effect of phonon scattering is negligible compared to the impurity scattering. This can again be contributed to the growth in an Ar/O₂ mixture, where the presence of oxygen can have a substantial negative effect on the electronic properties of the Al:ZnO thin film.

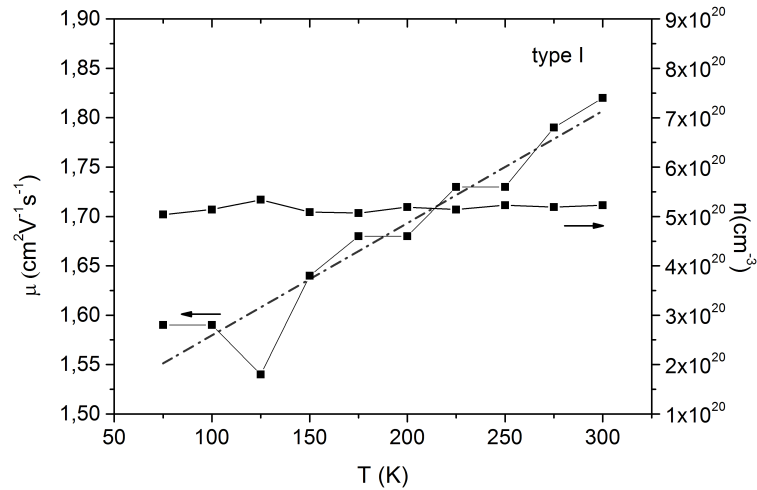


Figure 6.11: Temperature dependence of the charge-carrier mobility μ (left axis) and the change of carrier density n (right axis), of a type I film, grown in an Ar/O₂ gas mixture and with an Al-doping percentage of 1 % at.

6.3.2 Film growth in pure argon

In Al:ZnO films, it was shown before that controlling the oxygen vacancy density in the film is crucial to obtain thin films with a low resistivity and high mobility. The number of oxygen vacancies plays a large role in the formation of charge carriers, since the oxygen vacancies act as a donor in Al:ZnO [190, 191]. It is well known that resistivity of Al:ZnO films, grown in an oxygen rich atmosphere, can be lowered by post-annealing the Al:ZnO films in a hydrogen atmosphere [192, 193]. The hydrogen anneal removes any excess oxygen species out of the film, which can act as a strong electronegative impurity in the film. With the growth of an Al:ZnO thin film in pure Ar we are increasing the oxygen vacancy density, and are reducing any excess oxygen impurities in the film [7, 194]. In Figure 6.12, the temperature dependent resistivity is shown. The film grown in pure Ar clearly behaves metal-like in response to changing temperature with $\partial\rho/\partial T < 0$. As mentioned in Chapter 1.2.2, this is due to Mott tran-

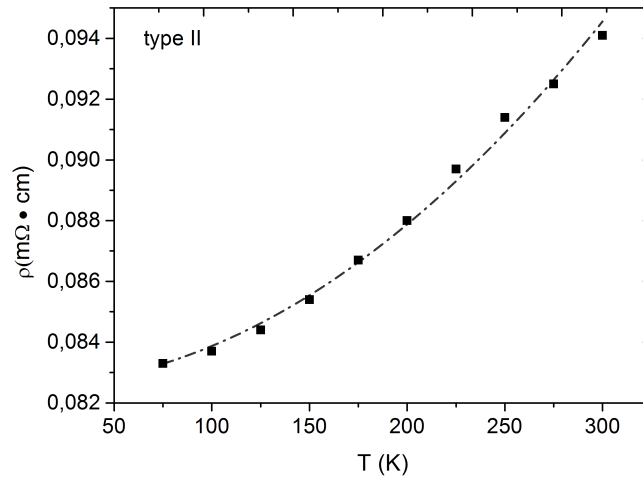


Figure 6.12: Resistivity measurement of a type II Al:ZnO film grown in pure Ar and with an Al-doping percentage of 1 at.%. The dashed line is a fit for the resistivity with Equation 6.2.

sition of the Al:ZnO thin film, which follows from a high impurity doping level. In Figure 6.13, the number of charge carriers is measured to be $1.68 \times 10^{21} \text{ cm}^{-3}$, which certainly satisfies the Mott criterion for metallic-like conductivity and which is more than three times higher compared to type I films [195]. The number of charge carriers exceeds the theoretical limit of the added Al to the ZnO crystal matrix when doping with 1 at.% Al. This is an indication that another electron donor, possibly oxygen vacancies, contribute to the number of charge carriers. Again, the number of charge carriers is constant with changing temperature, another indication for the undergone Mott transition [80, 189]. Since the films behave like a metal, we can use Matthiessen's rule to write down Equation 6.2. Here ρ_0 is the component due to impurity scattering and grain boundary scattering, which are not thermally activated [196]. However, for metal-like degenerate semiconductors, the temperature dependence of the resistivity on phonon scattering is proportional to T^p . In the case of Al:ZnO, the Debye temperature Θ_D , is around 400 °C, which means that we can set the ex-

ponent p as 2 for temperatures below Θ_D [171]. Both in Equation 6.2 and 6.3, ρ_l is the resistivity due to "lattice" or "phonon" scattering.

$$\rho(T) = \rho_0 + \rho_l T^2 \quad (6.2)$$

In the same way, since $\rho \propto 1/\mu$, the mobility can be fitted by Equation 6.3.

$$\mu(T) = \frac{1}{nq} \cdot \frac{1}{\rho_0 + \rho_l T^2} \quad (6.3)$$

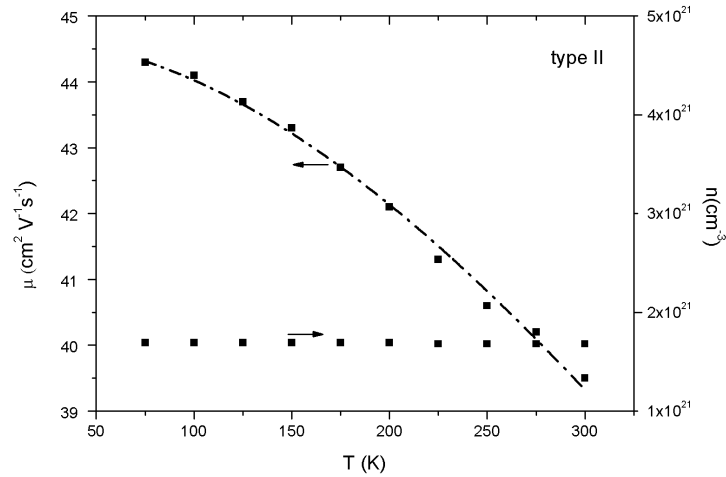


Figure 6.13: Temperature dependence of the charge-carrier mobility μ (left axis) and the change of carrier density n (right axis), of a type II film, grown in a pure and with an Al-doping percentage of 1 % at. The dashed line is a fit of the mobility with Equation 6.3.

6.3.3 Deposition of layered films

Since the layered film consists of a Ar/O₂ grown film with a thick capping layer of a film grown in Ar we expect the same conductive behaviour as in Chapter 6.3.2. From the resistivity measurements in Figure 6.14, and Hall measurements (Figure 6.15) we can conclude this is indeed the case. The nominal room temperature resistivity is however higher, 0.69 mΩ·

cm compared to $0.094 \text{ m}\Omega \cdot \text{cm}$. We can fit the resistivity and mobility data again with Equation 6.2 and Equation 6.3 respectively. The fitting parameters of the mobility and resistivity fits of the three types of films are summarized in Table 6.6. The fitting parameters for both the residual resistivity ρ_0 and resistivity ρ_l , caused by lattice vibrations, are in good agreement for both the resistivity and mobility fitting. The temperature dependent parameter for the resistivity and mobility is $\approx 1 \times 10^{-7} \text{ m}\Omega$ and $\approx 7\text{-}8 \times 10^{-7} \text{ m}\Omega \cdot \text{cm}/\text{K}^2$ for the type II Ar films and type III layered films respectively. The small temperature dependence of the resistivity, compared to a metal, is to be expected from a degenerate semiconductor [196]. The resistivity value is dominated by the temperature independent residual resistivity ρ_0 , which is caused by defect scattering.

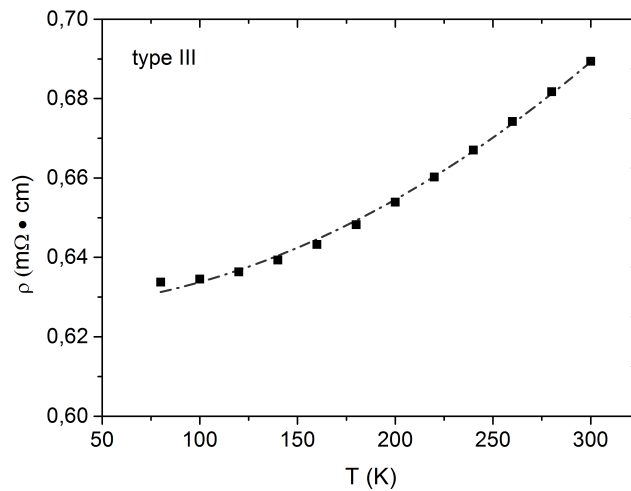


Figure 6.14: Temperature dependent resistivity measurement of a bilayered type III Al:ZnO film. The film was doped with 1 at. % Al.

The fitting parameters of the mobility and resistivity fits of the three types of films are summarized in Table 6.6.

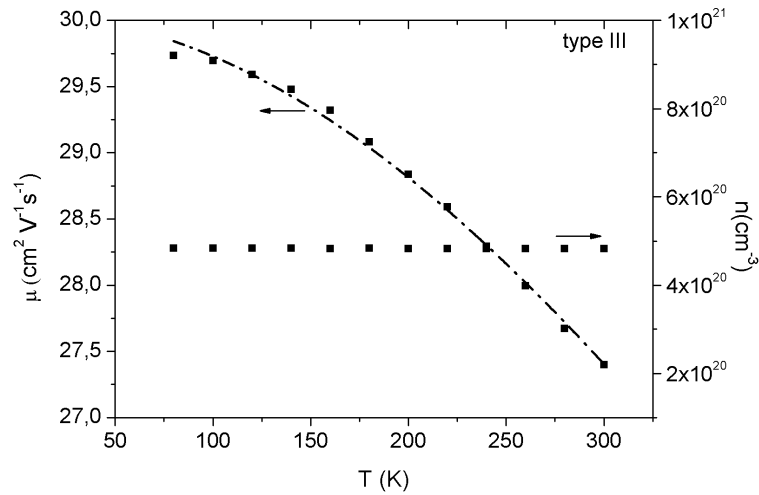


Figure 6.15: Temperature dependence of the charge-carrier mobility μ (left axis) and the change of carrier density n (right axis), of a type III film, grown in an Ar/O₂ gas mixture and with an Al-doping percentage of 1 % at. The dashed line is a fit of the mobility with Equation 6.3.

Table 6.6: Fitting parameters of the three film types: grown in Ar, in Ar/O₂ and bilayer deposition.

Film	Equation	Parameter	Value	R ²
Ar/O ₂	6.1	ρ_0	8.25 m Ω ·cm	0.99
		α	5.48×10^{-2} m Ω ·cm/K	
Ar	6.2	ρ_0	8.25×10^{-2} m Ω ·cm	0.99
		ρ_l	1.34×10^{-7} m Ω ·cm/K ²	
	6.3	ρ_0	7.76×10^{-2} m Ω ·cm	0.99
		ρ_l	1.18×10^{-7} m Ω ·cm/K ²	
Ar/O ₂ +Ar	6.2	ρ_0	0.62 m Ω ·cm	0.99
		ρ_l	6.93×10^{-7} m Ω ·cm/K ²	
	6.3	ρ_0	0.43 m Ω ·cm	0.99
		ρ_l	4.61×10^{-7} m Ω ·cm/K ²	

6.3.4 Layer-by-layer Al:ZnO thin film from solution-based synthesized particles

A film consisting of Al:ZnO nanocrystals, made by layer-by-layer deposition was measured in the Hall setup. A more comprehensive experimental description of the fabrication of these thin films can be found in Chapter 6 of the dissertation of A. Kelchtermans (Hasselt University, IMO - Inorganic and Physical Chemistry) [197]. From Figure 6.16 we can conclude that the temperature dependence of the resistivity is similar to the sputtered films of type I, which were grown in an Ar/O₂ mixture. This means that the film did not exhibit metal-like conductivity, which is necessary to commercialize the production of TCO films. Possibly, the films had enough charge carriers in order to satisfy the Mott criterion. Nevertheless, metal-like conductivity is not easy to obtain in wet-chemically processed Al:ZnO thin films because of the presence of oxygen during the heating process [116]. The room temperature resistivity of the Al:ZnO film was 9.5 mΩ·cm, with a mobility of 9.98 cm²V⁻¹s⁻¹ and a charge-carriers density of 6.53×10¹⁹ cm⁻³. These values are comparable to other layer by layer Al:ZnO thin films with solution synthesized particles in literature [198], however the electronic properties of these films are still below values of sputtered films [199].

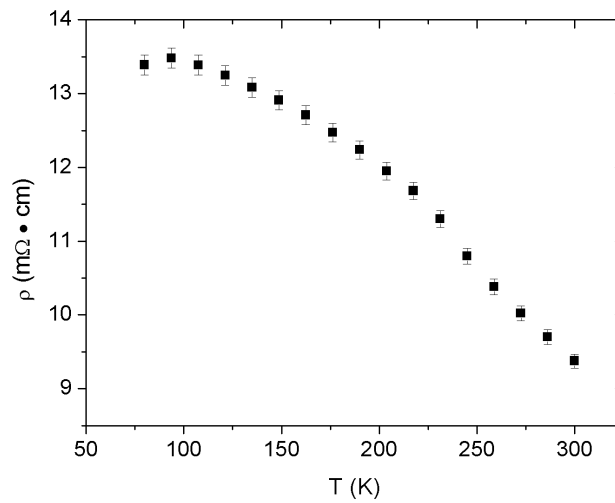


Figure 6.16: Temperature dependence of a layer-by-layer Al:ZnO film.

6.3.5 Magnetoresistance effect

The magnetoresistance measurements were performed on a bilayered type III film with an Al doping concentration of 1 at.%. ZnO films (doped with Al) are also known for their weak negative magnetoresistance effect. Most metals, alloys, and oxides with metal-like conduction show a positive magnetoresistance of typically 1% resistance increase at external magnetic fields of typically 10 Tesla at temperatures below 10 K. This can generally be understood by Kohler's rule, meaning that the effective mean free path of carriers becomes limited under external magnetic field by forcing them to move on (fractions) of Lorentz circles. Negative magnetoresistance is best known in form of the giant (negative) magnetoresistance effect "GMR" in heterostructures of (magnetic) metals [200,201], and from the colossal negative magnetoresistance effect "CMR" in mixed-valency manganese perovskites [202,203]. The negative magnetoresistance is in any case related to a magnetic ordering effect induced by an external magnetic field. For sputtered films prepared from ZnO targets containing 5 wt.% Al₂O₃, Li and co-workers found a normalized resistance drop $\Delta\rho/\rho(B = 0)$ by - 0.32 % at 5 K in a field of 2 Tesla [204]. This agrees well with the data by Liu and Jiang (also sputtering, same doping concentration) who report a drop of the normalized resistance by - 0.19 % at 2.5 K in a 2 Tesla field [205]. The highest drop of $\Delta\rho/\rho(B = 0) = - 6.9$ % was reported until now for pure ZnO films, prepared by laser ablation, at 5 K and a field of 6 Tesla [206]. We point out that neither ZnO nor AZO should exhibit any negative magnetoresistance unless there is a vanishingly small concentration of magnetic impurities such as iron or nickel incorporated in the films. Such impurities can be from the sputtering- or laser-ablation target, or released from the walls of the plasma-deposition chambers. Consequently, the mentioned articles explain data by fitting them to a model initially established by Khoshla and Fisher already in 1970 [207]. The model, developed for the degenerate semiconductor CdS, treats two magnetoresistance contributions: A negative contribution, pre-

vailing at low temperatures and low fields, results from the field-induced reduction of carrier-spin scattering at localized magnetic moments. The positive contribution, noticeable at higher fields, is a pure band structure effect attributed to a field-induced redistribution of carriers over two different conduction bands with different relaxation times.

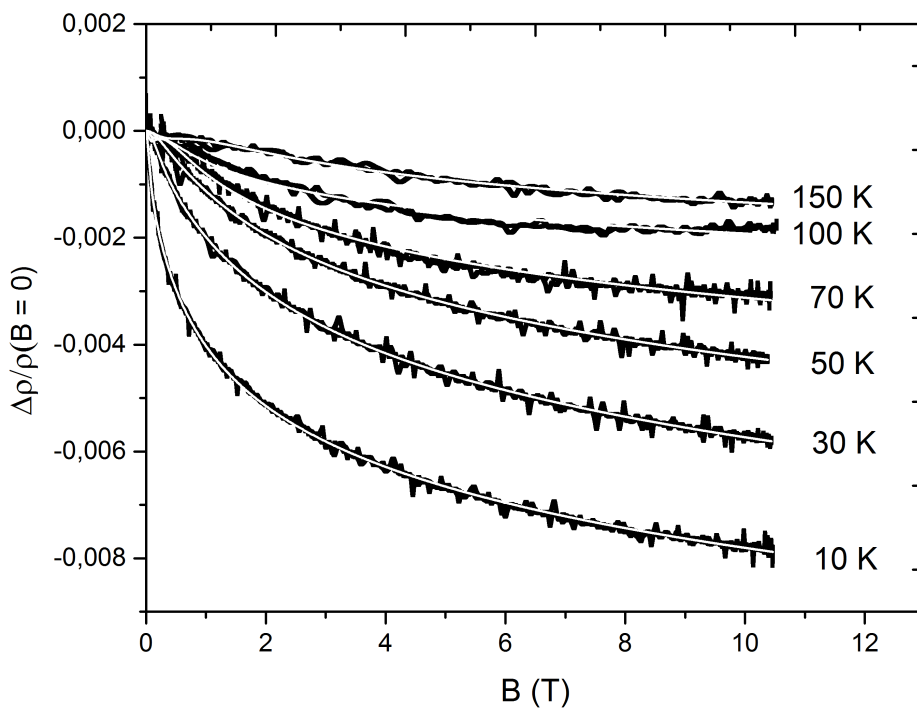


Figure 6.17: Negative magnetoresistance $\Delta\rho/\rho(B=0)$ in the low-temperature region between 10 and 150 K in pulsed magnetic fields up to 10 Tesla. The solid white lines are calculated according to Equation 6.4 as proposed by Koshla and Fisher [207].

The first set of data in pulsed magnetic fields was taken between 10 K and 150 K in field amplitudes limited to 10 Tesla. As shown in Figure 8, the MR amplitude reaches maximally - 0.78 % (10 K, 10 Tesla) and, under the same field, the resistance drop is only - 0.1 % at 150 K. In this

field- and temperature regime there is no indication for a positive MR and the amplitudes we find here are fully within the order identified in earlier work [204–206]. The fit function, according to the model of Khosla and Fisher and discussed in subsequent work, is given by Equation 6.4:

$$\frac{\Delta\rho}{\rho(B)} = -a^2 \ln(1 + b^2 B^2) + \frac{c^2 B^2}{1 + d^2 B^2} \quad (6.4)$$

Within the first (negative) magnetoresistance part, the parameters a and b depend mainly on temperature, magnetization, strength of the localized moments, the exchange integral, and the density of states at the Fermi level. For further details we refer to the earlier work [206, 207]. The parameters c and d in the second (positive) magnetoresistance contribution are functions of the absolute carrier concentration and conductivity. As can be seen from Figure 6, this four-parameter fit is in excellent agreement with the experimental data. The fitting parameters a , b , c , d , and the resulting R^2 values are summarized in Table 6.7. The parameters b , c and d have the unit $1/T$.

Table 6.7: Overview of the fitting parameters for the negative magnetoresistance data shown in Figure 6 according to the model by Koshla and Fisher [207].

Temperature	a (a')	b (b')	b	d	R^2
10 K	0.03 (0.03)	21.36 (12.69)	0.19	5.74	0.999 (0.998)
30 K	0.03 (0.03)	4.52 (3.16)	0.05	1.82	0.999 (0.998)
50 K	0.03 (0.03)	2.77 (1.92)	0.04	1.51	0.998 (0.998)
70 K	0.02 (0.02)	9.74 (1.89)	0.17	4.12	0.993 (0.993)
100 K	0.02 (0.02)	21.03 (2.44)	0.20	5.65	0.971 (0.969)
150 K	0.02 (0.02)	21.03 (0.83)	0.2	1.6	0.987 (0.984)

Hereby, we note that the fitting parameters do not follow a strictly systematic trend with changing temperature. Moreover, data show little variation and also simplified parameter sets can generate fits with almost the same quality. For comparison, we assumed $c = 0$ and thus considered only the negative magnetoresistance contribution. The remaining two-parameters

fits with only a' and b' were almost as good as the full four-parameter fits and the data sets (with a , b , and the resulting R^2) have been added to Table 6.7 (data between brackets). For peculiar sets of the four fit parameters in Equation 6.4, one can observe a transition from negative- to positive- and again to negative magnetoresistance. This rather uncommon situation was observed experimentally for Co-substituted ZnO films, prepared by laser ablation [206]. This gives confidence that the physical picture developed by Koshla and Fisher should at least be valid within certain circumstances [207]. From the excellent agreement between the fit-function and the experimental data shown in Figure 6.17 we can conclude that scattering at magnetic trace impurities is indeed the most probable origin of the weak negative magnetoresistance. For an experimental verification of the high-magnetic field magnetoresistance of our AZO films, we performed measurements in pulsed magnetic fields up to 45 Tesla. The data in Figure 6.18 show again the weak resistance drop below 10 Tesla, which was discussed and rendered with higher precision in Figure 6.17. After a shallow minimum around 10 Tesla, the resistance is clearly increasing with increasing field, and this resembles fully the behaviour of conventional magnetoresistance, according to Kohler's rule for non-magnetic materials.

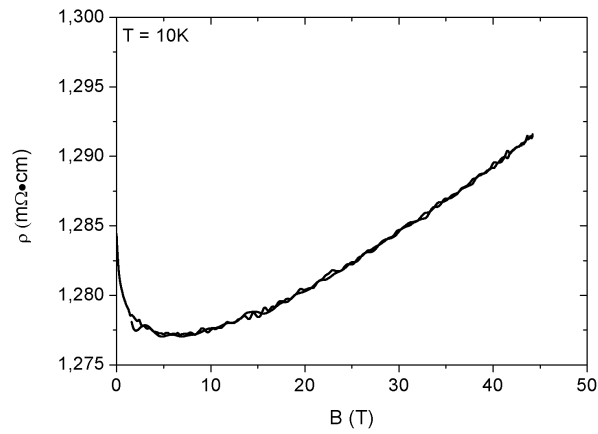


Figure 6.18: High field magnetoresistance measurement, with field strengths up to 45 T at 10 K. After a shallow minimum around 10 Tesla, the resistance is clearly increasing with increasing field, resembling the behaviour of conventional magnetoresistance. The two different curves, which are on top of each other, correspond to the increasing- and the decreasing branch of the magnetic field.

Chapter 7

Conclusion and Outlook to further research

In this thesis, we developed a custom-made sputtering system for the deposition of Al:ZnO thin films. The system was able to pump down to pressures below 1×10^{-6} hPa, as required to deposit films that do not contain any trace elements. Al:ZnO films were prepared by dc-sputtering on sapphire substrates without a magnetron or RF power and the targets were made by mixing different concentrations of Al-ZnO powder and ZnO powder. This way, the doping concentration of Al could be controlled.

As proof of concept, we used a target with only the Al-ZnO powder. These films had a doping concentration of 2.4 at.% Al, which is above the assumed solubility level of Al in the ZnO crystal lattice, as was discussed in Chapter 6.1. The best films were obtained with a substrate temperature of 400 °C and 2.0 hPa Ar pressure with $1-2 \times 10^{-2}$ hPa O₂. The films were composed of densely packed crystallites with a preferential growth along the c-axis direction. The electrical properties are below the best values found in literature, with a room-temperature resistivity of 3.7×10^{-3} Ωcm and a carrier mobility of $6.7 \text{ cm}^2 \text{V}^{-1} \text{s}^{-1}$. Contrary to what is expected for a charge-carrier density above the Mott criterion, the films did not exhibit

CHAPTER 7. CONCLUSION AND OUTLOOK TO FURTHER RESEARCH

metallic like conductive behaviour. Furthermore, the mobility was found to have a thermally activated behavior while the carrier density itself is temperature independent. The temperature dependence of the carrier density suggests that the sample is indeed on the metallic side of a Mott insulator-metal transition. This inconsistency may be attributed to the presence of oxygen in the sputter gas mixture, introducing electronegative oxygen impurities in the film, which act as electron traps. Furthermore, we point out that a thermally activated mobility is not uncommon and occurs e.g. in organic semiconductors where it is explained in a model where charge transport is governed by trapping and thermally-induced release of carriers at localized states in grain boundaries. Regarding the optical transparency in the frequency range of visible light, the films are close to the state-of-the-art with a transparency of 95% although the proposed deposition process is straight forward and no special annealing steps were applied. Nevertheless, for device application, the electronic properties of these films are not yet sufficient.

Subsequently, a doping level of 1 at.% Al was considered as a strategy to improve electronic properties. This ensures that we are on the safe side regarding the solubility of Al^{3+} ions in the zinc oxide lattice and avoid possible formation of insulating phases such as spinel. In order to grow films which contained a minimum amount of interstitial electronegative oxygen traps and to create oxygen vacancy donor states, we decided to deposit the Al:ZnO thin films in pure Ar. These films had exceptional electronic properties, with a minimum resistivity of $0.094 \text{ m}\Omega\cdot\text{cm}$, together with a high room temperature mobility of $40 \text{ cm}^2\text{V}^{-1}\text{s}^{-1}$. Furthermore, these films exhibited a metal-like temperature dependence of the resistivity, a conformation that the films underwent a Mott metal-insulator transition. In spite of the excellent electronic properties, the films had an optical transparency of only 65 % regarding their use in for example solar cell or OLED applications, this is too low.

CHAPTER 7. CONCLUSION AND OUTLOOK TO FURTHER RESEARCH

To overcome this drawback of low transparency, while preserving the electronic properties of the Ar-deposited 1 at.% Al thin films, we proposed to grow a layered film. The first layer was sputtered in an O₂/Ar gas mixture, this layer had very good transmittance, but poor electronic properties since the films did not have a metal-like temperature dependence of the resistivity. On top of this seeding layer, a second, highly conductive layer was deposited with sputtering in pure argon gas. This resulted in a film with low room temperature resistivity of 0.69 mΩ·cm and a high mobility of 27.5 cm²V⁻¹s⁻¹. Again, the films exhibited the necessary metal-like conductivity for TCO films. The optical transparency was 86%, which is a large improvement compared to the single layer Ar grown films. In summary we developed a deposition method which allows the synthesis of Al:ZnO films combining high optical transparency with excellent electronic properties, meaning that the resistivity- and mobility values come very close to the best results published in literature. Furthermore, EDX spectroscopy showed a homogeneous distribution of the aluminium in the Al:ZnO film. HR-TEM images indicated that the films showed a good crystalline structure at the interface with the sapphire substrate.

Given the high crystalline order and chemical purity of these films, we finally evaluated whether the material exhibits any kind of magnetoresistance effects. By measurements in pulsed magnetic fields up to 45 Tesla we found a weak positive magnetoresistance for fields above 10 Tesla, which is a conventional behaviour of metallic- or metallic-like materials. Interestingly there is also a weak, negative magnetoresistance effect in low magnetic field, pointing possibly to the presence of magnetic impurities in such a low concentration that they were not detectable by the analytical methods.

In the future, it is possible to further investigate the oxygen incorporation and the effect on the electronic properties of Al:ZnO films. Therefore, it would be beneficial to perform Hall measurements in an ambient hydrogen

CHAPTER 7. CONCLUSION AND OUTLOOK TO FURTHER RESEARCH

and oxygen atmosphere. Since the bilayer films have electronic and optical properties which are comparable to ITO, we should be able to fabricate organic solar cells and OLEDs with our Al:ZnO films.

List of Figures

1.1	Optical transmission spectra	4
1.2	Energy consumption of the world	7
1.3	Solar cells	11
1.4	The Samsung Smart Window ©	12
1.5	Optical spectrum of a ZnO TCO material.	13
1.6	$\rho(T)$ of amorphous indium oxide thin films	19
1.7	Evolution of band structure in a metal - insulator transition.	21
1.8	Price difference between Zn and In	24
1.9	Crystal structure of ZnO	25
1.10	Possible Al-doping sites for ZnO	25
2.1	Basic sputtering system	30
2.2	The initiation of plasma	31
2.3	Glow discharge in a plasma	33
2.4	Magnetron plasma confinement	34
2.5	Schematic representation of a PECVD reactor	36
2.6	Schematic representation a PLD deposition system.	37
3.1	The sputtering system	41
3.2	Schematic of the vacuum system	42
3.3	Technical drawing of the sputtering cathode	44
3.4	The substrate holder	47

LIST OF FIGURES

3.5 XRD spectrogram of a blank (0002) oriented synthetic sapphire (Al_2O_3) substrate.	48
3.6 The target	51
3.7 XRD spectrum of the Zano-Al powder after sintering at 900 °C for 1 hour.	52
4.1 Van der pauw geometries	56
4.2 Hall bar pattern	58
4.3 Hall measurement system	60
4.4 The hall effect of an n-type semiconductor	62
4.5 A schematic illustration of Bragg's law.	65
5.1 Optimizing the resistivity of Al:ZnO films as a function of the growth temperature.	73
5.2 XRD 2θ -scan of a 90 nm thick Al:ZnO film	74
5.3 SEM micrograph of an Al:ZnO film grown at 400 °C. The scale bar has a length of 500 nm.	75
5.4 AFM image of an Al:ZnO film grown at 400 °C. The scale bar has a length of $10\mu\text{m}$	76
5.5 XPS spectrum with the binding energy of the Zn 3p and Al 2s orbitals.	77
5.6 Resistivity measurement on an Al:ZnO film grown under optimized sputtering conditions.	78
5.7 Hall measurement of an Al:ZnO film grown under optimal sputtering conditions.	79
5.8 Optical transmission measurement of an Al:ZnO thin film	80
6.1 SEM micrograph of a film grown in an Ar/O ₂ gas mixture and with an Al-doping percentage of 1 at.%.	86
6.2 SEM micrograph of a film grown in an Ar/O ₂ gas mixture and with an Al-doping percentage of 1 at.%. The magnification is 200000x. Seeding points for growth of the crystal are seen in the center of the hexagonal crystallites.	86

LIST OF FIGURES

6.3 SEM micrograph of Al:ZnO films grown in pure Ar and with an Al-doping percentage of 1 at.%. The films grown in pure Ar do not show any hexagonal structures at this magnification.	88
6.4 SEM micrograph of Al:ZnO films grown in pure Ar and with an Al-doping percentage of 1 at.%, at a larger magnification the films show hexagonal shaped crystallites compared to Figure 6.3.	89
6.5 θ -2 θ scan of Al:ZnO films grown in pure Ar	90
6.6 SEM micrograph of bilayer Al:ZnO films, with an Al-doping percentage of 1 at.%. Compared to Figure 6.3, the films appears less rough. This could be an explanation for the better transparency of the bilayered Al:ZnO thin films as shown in Table 6.5	91
6.7 Cross-sectional ADF-STEM image of a bilayer Al:ZnO thin film	93
6.8 HR-TEM micrograph of an Al:ZnO thin film grown in pure Ar sputter-gas, with 1 at.% Al.	94
6.9 EDX mapping of an Al:ZnO thin film grown in pure Ar sputter-gas, with 1 at.% Al.	95
6.10 Resistivity measurement of a film grown in an Ar/O ₂ gas mixture and with an Al-doping percentage of 1 % at. The dashed line is a linear fit with Equation 6.1, where $\rho_0 = 8.25 \text{ m}\Omega\cdot\text{cm}$ and $\alpha = 5.48 \times 10^{-2} \text{ m}\Omega\cdot\text{cm}/\text{K}$ with an R ² value of 0.99.	96
6.11 Temperature dependence of μ and n for a type I film	97
6.12 Resistivity measurement of a type II Al:ZnO film grown in pure Ar and with an Al-doping percentage of 1 at.%. The dashed line is a fit for the resistivity with Equation 6.2.	98
6.13 Temperature dependence of μ and n for a type II film	99
6.14 Temperature dependent resistivity measurement of a bilayered type III Al:ZnO film. The film was doped with 1 at. % Al.	100
6.15 Temperature dependence of μ and n for a type III film	101
6.16 $\rho(T)$ of a layer by layer Al:ZnO film	103

LIST OF FIGURES

6.17 Fitted relative magnetoresistance	105
6.18 High field magnetoresistance measurement, with field strengths up to 45 T at 10 K. After a shallow minimum around 10 Tesla, the resistance is clearly increasing with increasing field, resembling the behaviour of conventional magnetoresistance. The two different curves, which are on top of each other, correspond to the increasing- and the decreasing branch of the magnetic field.	108

List of Tables

1	Overzicht van de verschillende Al:ZnO films	xii
2	Overview of the different Al:ZnO thin films.	xviii
1.1	Selected historical TCO references	6
1.2	Binary TCO materials	8
1.3	Overview of Al:ZnO thin films	26
3.1	Different parts of the sputtering cathode.	46
6.1	Measuring Al content in doped ZnO thin films	83
6.2	Deposition parameters for the deposition in Ar/O ₂ mixtures: type I films.	85
6.3	Deposition parameters for the deposition in pure Ar: type II films	87
6.4	Deposition parameters for the thin film growth in selected gases. The first layer is an Ar/O ₂ mixture seeding layer, fol- lowed by a layer grown in pure Ar: type III films.	91
6.5	Average transparency in percent	92
6.6	Fitting parameters of three types of film	101
6.7	Overview of the fitting parameters for the negative magne- toresistance data	106

LIST OF TABLES

Appendix A

Publications and Conference contributions

Publications

1. "Preparation of epitaxial films of the transparent conductive oxide Al:ZnO by reactive high-pressure sputtering in Ar/O₂ mixtures"
M. Van Gompel, B. Conings, K. L. Jiménez Monroy, J. D'Haen, K. Gilissen, M. D'Olieslaeger, M. K. Van Bael and P. Wagner.
Physica Status Solidi A **210** (5), 1013-1018 (2013).
2. "Morphological TEM studies and magnetoresistance analysis of sputtered Al-substituted ZnO films: the role of oxygen"
M. Van Gompel, A. Y. Atalay, A. Gaulke, M. K. Van Bael, J. D'Haen, S. Turner, G. Van Tendeloo, J. Vanacken, V. V. Moshchalkov and P. Wagner.
Physica Status Solidi A, submitted (September 2014).

APPENDIX A. PUBLICATIONS AND CONFERENCE CONTRIBUTIONS

3. "Adding biosensing functionalities to implant materials: heat transfer based characterization of DNA on synthetic sapphire chips"
M.S. Murib, W. S. Yeap, Y. Eurlings, B. van Grinsven, **M. Van Gompel**, H.G. Boyen, L. Michiels, M. Ameloot, R. Carleer, J. Warmer, P. Kaul, K. Haenen, W. De Ceuninck, M. J. Schöning and P. Wagner.
ACS Applied Materials & Interfaces, submitted (September 2014).
4. "Multi-sensor chip for the investigation of different types of metal oxides for the detection of H₂O₂ in the ppm range"
S. Reisert, B. Schneider, H. Geissler, **M. Van Gompel**, P. Wagner and M.J. Schöning.
Physica Status Solidi a **210** (5), 898-904 (2013).
5. "Biological modification of carbon nanowalls with DNA strands and hybridization experiments with complementary and mismatched DNA"
R. Vanswevelt, A. Malesevic, **M. Van Gompel**, A. Vanhulsel, S. Wenmackers, J. D'Haen, V. Vermeeren, A. Marcel, L. Michiels, C. Van Haesendonck and P. Wagner.
Chemical Physics Letters **485** (1-3), 196-201 (2011).

Oral presentations

1. Engineering of Functional Interfaces, Linz, Austria (18-/19-06-2011)
Preparation and characterization of Al-doped zinc-oxide layers: A new transparent electrode material.
M. Van Gompel, K. Schellens, M. K. Van Bael, and P. Wagner.
2. Engineering of Functional Interfaces, Zweibrücken, Germany (16-/17-07-2012)
Preparation and characterization of Al-doped zinc-oxide layers: An alternative to ITO.
M. Van Gompel, K. Schellens, M. K. Van Bael, and P. Wagner.

APPENDIX A. PUBLICATIONS AND CONFERENCE CONTRIBUTIONS

3. Topical Day: ZnO research in Flanders, Antwerp (12-12-2012)
Structural and electronic characterization of Al:ZnO films prepared by dc-sputtering in argon-oxygen mixtures.
M. Van Gompel, M. K. Van Bael, B. Conings, K. L. Jiménez Monroy, J. D'Haen, K. Gilissen, M. D'Olieslaeger and P. Wagner.
4. Engineering of Functional Interfaces, Hasselt (14-/15-07-2013)
Preparation of thin films of the transparent conductive oxide Al:ZnO by reactive high-pressure sputtering in Ar/O₂ mixtures.
M. Van Gompel, J. D'Haen, J. Drijkoningen, M. K. Van Bael and P. Wagner.

Poster contributions

1. Belgian Physical Society, Namur (25-05-2011)
Towards an alternative for ITO: Electrical properties of aluminium doped zinc oxide.
M. Van Gompel, K. Schellens, J. Drijkoningen, M. K. Van Bael and P. Wagner.
2. Engineering of Functional Interfaces, Linz, Austria (18-/19-06-2011)
Preparation and characterization of Al-doped zinc-oxide layers: A new transparent electrode material.
M. Van Gompel, K. Schellens, M. K. Van Bael, and P. Wagner.
3. Belgian Physical Society, Brussels (30-05-2012)
Preparation and characterization of Al-doped zinc-oxide layers.
M. Van Gompel, K. Schellens, M. K. Van Bael, and P. Wagner.
4. Engineering of Functional Interfaces, Zweibrücken, Germany (16-/17-07-2012)
Preparation and characterization of Al-doped zinc-oxide layers: An alternative to ITO.

APPENDIX A. PUBLICATIONS AND CONFERENCE CONTRIBUTIONS

M. Van Gompel, K. Schellens, M. K. Van Bael, and P. Wagner.

5. Engineering of Functional Interfaces, Hasselt (14-/15-07-2013)

Preparation of thin films of the transparent conductive oxide Al:ZnO by reactive high-pressure sputtering in Ar/O₂ mixtures.

M. Van Gompel, J. D'Haen, J. Drijkoningen, M. K. Van Bael and P. Wagner.

Appendix B

Nomenclature

TCO	transparent conductive oxide
LCD	liquid crystal display
ITO	indium tin oxide
AZO	aluminium zinc oxide
SEM	scanning electron microscope
HR-TEM	high resolution - transmission electron microscope
SLG	soda lime glass
BTU	British thermal unit
OLED	organic light-emitting diode
GZO	gallium zinc oxide
CNT	carbon nanotubes
XRD	X-ray diffraction
dc	direct current
rf	radio frequency
CVD	chemical vapour deposition
DCMRS	direct current magnetron reactive sputtering
RFMRS	radio frequency magnetron reactive sputtering
LPCVD	low pressure chemical vapour deposition
PLD	pulsed laser deposition
PVD	physical vapour deposition

APPENDIX B. NOMENCLATURE

CFUBMS	closed field unbalanced magnetron sputtering
PECVD	plasma enhanced chemical vapour deposition
MOCVD	metal organic chemical vapour deposition
IZO	indium zinc oxide
UHV	ultra high vacuum
CF	conflat ®
ISO-KF	international standard institute - klein flange
BNC bus	Bayonet Neill-Concelman bus
PID	proportional-integral-derivative
MW	molecular weight
FWHM	full width at half maximum
FIB	focussed ion beam
HAADF	high-angle annular dark field
EDX	energy-dispersive X-ray mapping
XPS	X-ray photo electron spectroscopy
ICP	Inductive coupled plasma spectroscopy
AFM	atomic force microscopy
ADF-STEM	annular-darkfield scanning transmission-electron microscopy
NIR	near infrared
NMR	nuclear magnetic resonance

Appendix C

Symbol list

E	electric field
m_e	electron mass
\mathbf{v}_t	thermal velocity
k_B	Boltzmann's constant
T	temperature
l	mean free path
τ	relaxation time
\mathbf{a}	acceleration
\mathbf{v}	velocity
$\langle \mathbf{v} \rangle$	average velocity
J	current density
n	electron density
σ	conductivity
μ	mobility
F	force
\mathbf{p}	momentum
ω_p	plasma frequency
m_e^*	effective mass of an electron
ω	frequency
ϵ_0	vacuum permittivity

APPENDIX C. SYMBOL LIST

ϵ_r	relative permittivity
a_0	Bohr radius
a_H^*	adapted Bohr radius
ρ	resistivity
R_s	sheet resistance
R	resistance
I	current
V	voltage
V_H	Hall voltage
B	magnetic field
B	magnetic field strength
t	thickness
V_ρ	voltage difference for calculating ρ
w	width
l	length
τ_l	collision time for scattering by phonons
τ_i	collision time for scattering by impurity imperfections
ρ_l	electronic resistivity caused by thermal phonons
ρ_i	electronic resistivity caused by scattering
μ_h	mobility of positive charge carriers
μ_e	mobility of negative charge carriers
p	positive charge carrier density
μ_l	mobility for scattering by phonons
μ_i	mobility time for scattering by impurities
v_D	drift velocity
R_H	Hall coefficient
d	distance between planes in real space
n	integer
λ	wavelength

Bibliography

- [1] P. Drude, *Annalen der Physik* **306**, 566–613 (1900).
- [2] C. Guillén and J. Herrero, *Vacuum* **84**, 924–929 (2010).
- [3] H. Kim, C. M. Gilmore, A. Piqué, J. S. Horwitz, H. Mattoussi, H. Murata, Z. Kafafi, and D. B. Chrisey, *Journal of Applied Physics* **86**, 6451 (1999).
- [4] K. Bädeker, *Annalen der Physik (Leipzig)* **22**, 749–766 (1907).
- [5] C. G. Granqvist, *Solar Energy Materials and Solar Cells* **91**, 1529–1598 (2007).
- [6] H. Saarenpää, T. Niemi, A. Tukiainen, H. Lemmentyinen, and N. Tkachenko, *Solar Energy Material and Solar Cells* **94**, 1379–1383 (2010).
- [7] U. Özgür, Y. I. Aliviv, C. Liu, A. Teke, M. A. Reshchikov, S. Dogan, V. Avrutin, S. J. Cho, and H. Morkoç, *Journal of Applied Physics* **98**, art. no. 041301 (2005).
- [8] J. W. Lee, N. G. Subtramaniam, J. C. Lee, S. Kumar, and T. W. Kang, *Euro Physics Letters* **95**, art. no. 47002 (2011).
- [9] H. Dixit, R. Saniz, S. Cottenier, D. Lamoën, and B. Partoens, *Journal of Physics: Condensed Matter* **24**, art. no. 205503 (2012).
- [10] M. Matsubara, M. N. Amini, R. Saniz, D. Lamoën, and B. Partoens, *Physical Review B* **86**, art. no. 165207 (2012).

BIBLIOGRAPHY

- [11] R. Saniz, Y. Xu, M. N. Amini, H. Dixit, D. Lamoen, and B. Partoens, *Journal of Physics and Chemistry of Solids* **74**, 45–50 (2013).
- [12] T. Minami, T. Kakumu, Y. Takeda, and S. Takata, *Thin Solid Films* **291**, 1–5 (1996).
- [13] A. J. Leenheer, J. D. Perkins, M. V. Hest, J. J. Berry, R. P. O´hayre, and D. S. Ginley, *Physical Review B* **77**, art. no. 115215 (2008).
- [14] M. J. Zunick, U.S. Patent **2,516,663** (1947).
- [15] L. Hu, D. S. Hecht, and G. Grüer, *Applied Physics Letters* **94**, art. no. 081103 (2009).
- [16] F. Louwet, L. Groenendaal, J. D´Haen, J. Manca, J. V. Luppen, E. Verdonck, and L. Leenders, *Synthetic Metals* **135-136**, 115–117 (2003).
- [17] L. Groenendaal, F. Jonas, D. Freitag, H. Pielartzik, and J. R. Reynolds, *Advanced Materials* **12**, 481–494 (2000).
- [18] D. S. Ginley, H. Hosono, D. C. P. J. Berry, D. P. Cann, T. J. Coutts, K. Ellmer, B. Falabretti, T. A. Gessert, and C. G. G. et al., *Handbook of Transparent Conductors* (Springer, ISBN: 978-1-4419-1637-2, 2010).
- [19] G. Helwig, *Zeitschrift für Physik* **132**, 621 (1952).
- [20] H. A. McMaster, U.S. Patent **2,429,420** (1947).
- [21] J. M. Mochel, U.S. Patent **2,564,706** (1947).
- [22] W. O. Lytle and A. E. Junge, U.S. Patent **2651585** (1951).
- [23] H. F. Dates and J. K. Davis, U.S. Patent **3,331,702** (1967).
- [24] T. Hada, *Thin Solid Films* **7**, 135 (1971).
- [25] J. M. Mochel, U.S. Patent **2,564,707** (1951).

BIBLIOGRAPHY

- [26] L. Holland and G. Siddall, *Vacuum* **3**, 375–391 (1953).
- [27] R. Groth, *Physica Status Solidi* **14**, 69 (1969).
- [28] Furubayashi et al., *Applied Physics Letters* **86**, art. no. 252101 (2005).
- [29] H. Enoki, T. Nakayama, and J. Echigoya, *Physica Status Solidi A* **129**, 181–191 (1992).
- [30] T. Minami, H. Sonohara, S. Takata, and H. Sato, *Japanese Journal of Applied Physics* **33**, L1693–L1696 (1994).
- [31] T. Moriga, Y. Hayashi, K. Kondo, Y. Nishimura, K. Murai, I. Nakabayashi, H. Fukumoto, and K. Tominaga, *Journal of Vacuum Science and Technology A* **22**, 1705–1710 (2004).
- [32] A. J. Nozik, *Physical Review B* **6**, 453 (1972).
- [33] F.T.J. Smith and S.L. Lyu, *Journal of the Electrochemical Society* **128**, 1083 (1981).
- [34] T. Minami, H. Sonohara, T. Kakumu, and S. Takata, *Japanese Journal of Applied Physics* **34**, L971–L974 (1995).
- [35] M. Orita et al., *Japanese Journal of Applied Physics P2* **34**, 1550 (1995).
- [36] M. Orita et al., *Philosophical Magazine B* **81**, 501 (2001).
- [37] H. Ohta, M. Orita, M. Hirano, H. Tanji, H. Kawazoe, and H. Hosono, *Applied Physics Letters* **76**, 1740–2043 (2000).
- [38] J. Phillips and D. Douglas, *Physics for Scientists and Engineers with Modern Physics* (Prentice Hall, 2009).
- [39] A. Reeves and D. Griffiths, *Introduction to Electrodynamics* (Prentice Hall, 1999).
- [40] K. Ellmer, *Journal of Physics D: Applied Physics* **33**, 45–47 (2000).

BIBLIOGRAPHY

- [41] E. Shanthi, A. Banerjee, V. Dutta, and K. L. Chopra, *Journal Applied Physics* **53**, 1615–1621 (1982).
- [42] B. Thangaraju, *Thin Solid Films* **402**, 71–78 (2002).
- [43] L. Castañeda, *Materials Sciences and Applications* **2**, 1233–1242 (2011).
- [44] T. Minami, *Semiconductor Science and Technology* **20**, S35 (2005).
- [45] T. Minami, *MRS Bulletin* **25**, 38–44 (2000).
- [46] H. Un’no, N. Hikuma, T. Omata, N. Ueda, T. Hashimoto, and H. Kawazoe, *Japanese Journal of Applied Physics* **32**, doi: 10.1143/JJAP.32.L1260 (1993).
- [47] T. Minami, *Journal of Vacuum Science and Technology A* **17**, 1765 (1999).
- [48] J. M. Phillips, J. Kwo, G. A. Thomas., S. A. Carter., R. J. Cava, S. Y. Hou, J. J. Krajewski, J. H. Marshall, W. F. Peck, D. H. Rapkine, and R. B. VanDove, *Applied Physics Letters* **65**, doi: 10.1063/1.113052 (1994).
- [49] T. Minami, Y. Takeda, T. Kakumu, S. Takata, and I. Fukuda, *Journal of Vacuum Science and Technology A* **14**, 958 (1997).
- [50] T. Minami, Y. Takeda, S. Takata, and T. Kakumu, *Thin Solid Films* **308-309**, 13–18 (1997).
- [51] H. Kawazoe, M. Yasukawa, H. Hyodo, M. Kurita, H. Yanagi, and H. Hosono, *Nature* **389**, 939–942 (1997).
- [52] A. Kudo, H. Yanagi, H. Hosono, and H. Kawazoe, *Applied Physics Letters* **73**, 220–222 (1998).
- [53] G. Hautier, A. Miglio, G. Ceder, G. M. Rignanese, and X. Gonze, *Nature Communications* **4**, doi: 10.1038/ncomms3292 (2012).
- [54] J. Robertson and S. J. Clark, *Physical Review B* **83**, art. no. 075205 (2011).

BIBLIOGRAPHY

- [55] R. Gillen, S.J. Clark, and J. Robertson, *Physical Review B* **87**, art. no. 125116 (2013).
- [56] O. Lopatiuk-Tirpak, L. Chernyak, F. X. Xiu, J. L. Liu, S. Jang, F. Ren, S.J. Pearton, K. Gartsman, Y. Feldman, A. Osinsky, and P. Chow, *Journal of Applied Physics* **100**, art. no. 086101 (2006).
- [57] S.J. Pearton and F. Ren, *Current Opinion in Chemical Engineering* **3**, 51–55 (2014).
- [58] H. Sato, T. Minami, S. Takata, and T. Yamada, *Thin Solid Films* **15**, 27–31 (1993).
- [59] J. Robertson, P.W. Peacock, M.D. Towler, and R. Needs, *Thin Solid Films* **22**, 96–100 (2002).
- [60] R. Nagarajan, N. Duan, M.K. Jayaraj, J. Li, K.A. Vanaja, A. Yokochi, A. Dreaseke, J. Tate, and A.W. Sleight, *International Journal of Inorganic Materials* **3**, 265–270 (2001).
- [61] J. Müller, B. Rech, J. Springer, and M. Vanecek, *Solar Energy* **77**, 917–930 (2004).
- [62] E. Fortunato, D. Ginley, H. Hosono, and D.C. Paine, *MRS Bulletin* **32**, 242–247 (2007).
- [63] K.C. Lai, J.H. Wang, C.H. Lu, F.J. Tsai, C.H. Yeh, and M.P. Hounq, *Solar Energy Materials and Solar Cells* **95**, 415–418 (2011).
- [64] http://commons.wikimedia.org/wiki/File:Solar_cell.png, Public Domain (2005).
- [65] http://commons.wikimedia.org/wiki/File:Illust_poly_thinfilm.gif, Public Domain (2009).
- [66] E. M. C. Fortunato, P. M. C. Barquinha, A. C. M. B. G. Pimentel, A. M. F. Goncalves, A. J. S. Marques, R. F. P. Martins, and L. M. N. Pereira, *Applied Physics Letters* **85**, doi: 10.1063/1.1790587 (2004).

BIBLIOGRAPHY

- [67] M. Katayama, *Thin Solid Films* **341**, 140–147 (1999).
- [68] Y. Park, V. Choong, Y. Gao, and B. R. Hsieh, *Applied Physics Letters* **68** (1996).
- [69] J. Lewis, S. Grego, B. Chalamala, E. Vick, and D. Temple, *Applied Physics Letters* **85**, doi: 10.1063/1.1806559 (2004).
- [70] F. Nüesch, E. W. Forsythe, Q. T. Le, Y. Gao, and L. J Rothberg, *Journal of Applied Physics* **87**, 7973 (2000).
- [71] A. Hauch, A. Georg, S. Baumgärtner, U. Opara Krasövec, and B. Orel, *Electrochimica Acta* **46**, 2131–2136 (2001).
- [72] D. T. Gillaspie, R. C. Tenent, and A. C. Dillon, *Journal of Materials Chemistry* **20**, 9585–9592 (2010).
- [73] M. A. Kaid, *Egyptian Journal of Solids* **29** (2006).
- [74] X. Zhang, H. Sun, Z. Li, J. Xu, S. Jiang, Q. Zhu, A. Jin, and G. Zakharova, *Journal of the Electrochemical Society* **160**, H587–H590 (2013).
- [75] C. G. Granqvist, *Thin Solid Films* **193**, 730–741 (1990).
- [76] L. Kang, Y. Gao, H. Lua, J. Wang, B. Zhu, Z. Zhang, J. Du, M. Kanehira, and Y. Zhang, *Solar Energy Materials and Solar Cells* **95**, 3189–3194 (2011).
- [77] <http://samsungsmartwindow.wikispaces.com/>, licensed under a Creative Commons (2014).
- [78] P. P. Edwards, A. Porch, M. O. Jones, D. V. Morgan, and R. M. Perks, *Dalton Transactions* **19**, 2995–3002 (2004).
- [79] N. F. Mott, *Review of Modern Physics* **40**, 677–683 (1968).
- [80] C. Kittel, *Introduction to Solid State Physics* (John Wiley and Sons, ISBN: 978-0471415268, 2005).

BIBLIOGRAPHY

- [81] N. F. Mott and M. Kaveh, *Philosophical Magazine B* **47**, 577–603 (1983).
- [82] M. R. Graham, C. J. Adkins, H. Behar, and R. Rosenbaum, *Journal of Physics: Condensed Matter* **10**, doi: 10.1088/0953-8984/10/4/010 (1998).
- [83] J. I. Hamberg and C. G. Granqvist, *Journal of Applied physics* **60**, R123.
- [84] A. Porch, D. V. Morgan, D. M. Perks, M. O. Jones, and P. P. Edwards, *Journal of Applied Physics* **95**, 9 (2004).
- [85] N. F. Mott, *Metal-Insulator-Transition* (Taylor and Francis, London, 1990).
- [86] K. R. Seddon and M. Zaworotko, *Crystal Engineering: The Design and Application of Functional Solids* (Kluwer Academic Publishers, 1999).
- [87] P. P. Edwards and C. N. R. Rao, *The Metallic and Nonmetallic states of Matter* (Taylor and Francis, London, ISBN: 9780850663211, 1984).
- [88] J. G. Lu, S. Fijita, T. Kawaharamura, H. Nishinaka, Y. Kamada, T. Ohshima, Z. Ye, Y. J. Zeng, Y. Z. Zhang, L. P. Zhu, H. He, and B. H. Zhao, *Journal of Applied Physics* **101**, art. no. 083705 (2007).
- [89] T. G. Castner, N. K. Lee, G. S. Cieloszyk, and G. Salinger, *Physical Review Letters* **34**, doi: 10.1103/PhysRevLett.34.1627 (1975).
- [90] X. Blase, E. Bustarret, C. Chapelier, T. Klein, and C. Marcenat, *Nature Materials* **8**, doi: 10.1038/NMAT2425 (1999).
- [91] G. Rupprecht, *Zeitschrift für Physik* **139**, 504–517 (1954).
- [92] D. Xu, Z. Deng, J. Xiao, C. Liang, Z. Pei, and C. Sun, *Physics Letters A* **346**, 148–152 (2005).

BIBLIOGRAPHY

- [93] A. Tanaka, M. Hirata, Y. Kiyohara, M. Nakano, K. Omae, M. Shiratani, and K. Koga, *Thin Solid Films* **518**, 2934–2936 (2009).
- [94] A. Tanaka, M. Hirata, M. Omura, N. Inoue, T. Ueno, T. Homma, and K. Sekizawa, *Journal of Occupational Health* **44**, 99–102 (2002).
- [95] M. E. Blazka, D. Dixon, E. Haskin, and G. J. Rosenthal, *Fundamentals of Applied Toxicology* **22**, 231–239 (1994).
- [96] R. G. Gordon, *MRS Bulletin* **25**, 52–57 (2000).
- [97] G. J. Exarhos and X. D. Zhou, *Thin Solid Films* **515**, 7025–7052 (2007).
- [98] K. Ellmer and R. Wendt, *Surface and Coatings Technology* **93**, 21–26 (1997).
- [99] S. Bose, S. Ray, and A. K. Barua, *Journal of Physics D: Applied Physics* **29** (1996).
- [100] T. Minami, T. Miyata, and Y. Ohtani, *Physica Status Solidi A* **9**, 3145–3151 (2007).
- [101] J. Nishino, *Materials Research Society Symposium Proceedings* **363**, 219–224 (1995).
- [102] D. R. Sahu, S. Y. Lin, and J. L. Huang, *Solar Energy Materials and Solar Cells* **91**, 803–813 (2007).
- [103] A. Anders, S. H. N. Lim, K. M. Yu, J. Andersson, and J. Rosén, *Thin Solid Films* **518**, 3313–3319 (2010).
- [104] K. Schellens, B. Capon, C. De Dobbelaere, C. Detavernier, A. Hardy, and M. K. Van Bael, *Thin Solid Films* **524**, 81–85 (2012).
- [105] M. Kumar, R. M. Mehra, and S. Y. Choi, *Current Applied Physics* **9**, 737–741 (2009).
- [106] A. Ashrafi, *Journal of Applied Physics* **102**, art. no. 071101 (2007).

BIBLIOGRAPHY

- [107] H. McMurdie, M. Morris, E. Evans, B. Paretzkin, W. Wong-Ng, L. Ettinger, and C. Hubbard, *Powder Diffraction* **1**, 76 (1986).
- [108] J. Zhang and W. Que, *Solar Energy Materials and Solar Cells* **94**, 2181–2186 (2010).
- [109] H. Serier, M. Gaudon, and M. Ménétrier, *Solid State Science* **11**, 1192–1197 (2009).
- [110] A. Kelchtermans, K. Elen, K. Schellens, B. Conings, H. Damm, H. G. Boyen, J. D´Haen, P. Andriaensens, A. Hardy, and M. K. Van Bael, *RSC Advances* **3**, 15254–15262 (2013).
- [111] Y. Y. Chen, P. W. Wang, J. C. Hsu, and C. Y. Lee, *Vacuum* **87**, 227–231 (2013).
- [112] S. Jäger, B. Szyska, J. Szczyrbowski, and G. Bräuer, *Surface and Coatings Technology* **98**, 1304–1314 (1998).
- [113] A. A. Alnajjar, *Advanced Condensed Matter Physics* p. doi: 10.1155/2012/682125 (2012).
- [114] R. Hong, X. Jiang, G. Heide, B. Szyszka, V. Sittinger, and W. Werner, *Journal of Crystal Growth* **249**, 461–469 (2003).
- [115] N. Neves, R. Barros, E. Antunes, J. Calado, E. Fortunato, R. Martins, and I. Ferreira, *Journal of the European Ceramic Society* **32**, 4381–4391 (2012).
- [116] J. P. Lin and J. M. Wu, *Applied Physics Letters* **92**, 134103 (2008).
- [117] G. Bräuer, B. Szyszka, M. Vergöhl, and R. Bandorf, *Vacuum* **84**, 1354–1359 (2010).
- [118] C. F. Gallo, *IEEE Transactions on Industry Applications* **IA-13**, 739 (1975).
- [119] P. Wagner, H. Adrian, and C. Tomé-Rosa, *Physica C* **195**, 258–262 (1992).

BIBLIOGRAPHY

- [120] I. Safi, *Surface and Coatings Technology* **127**, 203–219 (2000).
- [121] P.J. Kelly and R. D. Arnell, *Vacuum* **56**, 159–172 (2000).
- [122] J. Musil and S. Kadlec, *Vacuum* **5**, 435–444 (1990).
- [123] F. Adibi, I. Petrov, J. E. Greene, L. Hultman, and J. E. Sundgren, *Journal of Applied Physics* **12**, 8580–8589 (1993).
- [124] B. Window and N. Savvides, *Journal of Vacuum Science and Technology A* **4(2)**, 196–202 (1986).
- [125] B. Window and N. Savvides, *Journal of Vacuum Science and Technology A* **4(3)**, 453–456 (1986).
- [126] B. Window and N. Savvides, *Journal of Vacuum Science and Technology A* **4**, 504–508 (1986).
- [127] Y. Yoshida, T.A. Gessert, C.L. Perkins, and T.J. Coutts, *Journal Vacuum Science Technololgy A, Vacuum Surface Films* **21/4**, doi: 10.1116/1.1586281 (2003).
- [128] N. Yamada, T. Tatejima, H. Ishizaki, and T. Nakada, *Japanese Journal of Applied Physics Part 2* **45/42-45**, L1179 (2006).
- [129] H. C. Lee and O. O. Park, *Vacuum* **80/8**, 880–887 (2006).
- [130] D. Kim, *Journal of Non-Crystalline Solids* **331/1-3**, 41–47 (2003).
- [131] M. H. Ahn, E. S. Cho, and S. J. Kwon, *Vacuum* **101**, 221–227 (2014).
- [132] R. Triboulet, *Progress in Crystal Growth and Characterization of Materials* **60**, 1–14 (2014).
- [133] R. Das and S. Ray, *Journal of Physics D: Applied Physics* **36/2**, 152 (2003).
- [134] E. M. Hopper, Q. Zhu, J. Gassmann, A. Klein, and T. O. Mason, *Applied Surface Science* **264**, 811–815 (2013).

BIBLIOGRAPHY

- [135] E. Fortunato, V. Assuncao, A. Goncalves, A. Marques, H. Aguas, L. Pereira, I. Ferreira, P. Vilarinho, and R. Martins, *Thin Solid Films* **44**, 451–452 (2004).
- [136] K.J. Ahn, J. H. Park, B. K. Shin, W. Lee, G. Y. Yeom, and J. M. Myoung, *Applied Surface Science* **271**, 216 (2013).
- [137] T. Minami, T. Yamamoto, and T. Miyata, *Thin Solid Films* **366/1-2**, 63–68 (2000).
- [138] M. C. Costello, D. A. Tossell, D. M. Reece, and C. J. Brierley, *Diamond and Related Materials* **3**, 1137–1141 (1994).
- [139] Y. Wang, H. Gong, F. Zhu, L. Liu, L. Huang, and A. C. H. Huan, *Materials Science and Engineering: B* **85**, 131–134 (2001).
- [140] S. Sheng, G. Fang, C. Li, S. Xu, and X. Zhao, *Physica Status Solidi A* **203**, 1891–1900 (2006).
- [141] K. Bahroun, H. Bhem, F. Mitschker, P. Awakowicz, R. Dahlmann, and C. Hopmann, *Journal of Physics D: Applied Physics* **47** (2014).
- [142] H. Yanagi, K. Ueda, H. Ohta, M. Orita, M. Hirano, and H. Hosono, *Solid State Communications* **121**, 15–17 (2001).
- [143] D. Ginley, B. Roy, A. Ode, C. Warmsingh, Y. Yoshida, P. Parilla, C. Teplin, T. Kaydanova, A. Miedaner, C. Curtis, A. Martinson, T. Coutts, D. Readey, H. Hosono, and J. Perkins, *Thin Solid Films* **445**, 193–198 (2003).
- [144] S. M. Park, T. Ikegam, K. Ebihara, and P. K. Shin, *Applied Surface Science* **253**, 1522–1527 (2006).
- [145] H. Kim, J. S. Horwitz, S. B. Qadri, and D. B. Chrisey, *Thin Solid Films* **420**, 107–111 (2002).
- [146] P. Gondoni, M. Ghidelli, F. D. Fonzo, V. Russo, P. Bruno, J. Martí-Rujas, C. E. Bottani, A. L. Bassi, and C. S. Casari, *Thin Solid Films* **520**, 4707–4711 (2012).

BIBLIOGRAPHY

- [147] L. M. Wong, S. Y. Chiam, W. K. Chim, J. S. Pan, and S. J. Wang, *Thin Solid Films* **545**, 285–290 (2013).
- [148] J. H. Qi, Y. Li, T. T. Duong, H. J. Choi, and S. G. Yoon, *Journal of Alloys and Compounds* **556**, 121–126 (2013).
- [149] K. Ramamoorthy, C. Sanjeeviraja, M. Jayachandran, K. Sankaranarayana, P. Misra, and L. M. Kukreja, *Current Applied Physics* **6**, 103–108 (2006).
- [150] K. Ramamoorthy, K. Kumar, R. Chandramohan, K. Sankaranarayanan, R. Saravanan, I. V. Kityk, and P. Ramasamy, *Optics Communications* **262**, 91–96 (2006).
- [151] A. Suresh, P. Gollakota, P. Wellenius, A. Dhawan, and J. F. Muth, *Thin Solid Films* **516**, 1326–1329 (2008).
- [152] J. H. Kim, K. A. Jeon, G. H. Kim, and S. Y. Lee, *Applied Surface Science* **252**, 4834–4837 (2006).
- [153] Z. Kántor, E. Papadopoulou, E. Aperathitis, J. L. Deschanvres, K. Somogyi, and I. Szendröd, *Thin Solid Films* **516**, 8136–8140 (2008).
- [154] M. Neumann-Spallart, S. P. Pai, and R. Pinto, *Thin Solid Films* **515**, 8641–8644 (2007).
- [155] A. V. S. and R. M. Mehra, N. Buthrath, A. Wakahara, and A. Yoshida, *Journal of Applied Physics* **90**, 5661 (2001).
- [156] P. Wagner, *Diplomarbeit TH Darmstadt* (1991).
- [157] H. S. Huang, H. C. Tung, C. Chiu, I. Hong, R. Chen, J. Chang, and H. Lin, *Thin solid films* **518**, 6071–6075 (2010).
- [158] L. J. Van der Pauw, *Philips technical review* **26**, 220 (1958).
- [159] Lake Shore Cryotronics Inc., *Lake Shore 7500/9500 series Hall System Users Manual: Appendix A. Technical report.*

BIBLIOGRAPHY

- [160] Y. Komori, S. Sakuma, and T. Okamoto, *Physical Review Letters* **99** (2007).
- [161] J.J. Bissell, C. P. Ridbers, and R.J. Kingham, *Physical Review Letters* **105** (2010).
- [162] T. Klein, Z. Pribulova, R. Piquerel, H. Cercellier, J. Marcus, and C. Marcenat, *Physical Review B* **83** (2011).
- [163] E. H. Hall, *American Journal of Mathematics* **2**, 287–292 (1879).
- [164] D. Schroder, *Semiconductor material and device characterization* (John Wiley & Sons, New York, 1998).
- [165] R. Smith, *Semiconductors* (Cambridge University Press, Cambridge, 1959).
- [166] S. D. Janssens, PhD Thesis, Universiteit Hasselt (2011).
- [167] B. D. Cullity, *Elements of x-ray diffraction* (Addison-Wesley Publishing Company, Inc., 1978).
- [168] J. D. McKinley and J. E. Vance, *Journal of Chemical Physics* **22**, 1120 (1954).
- [169] M. Van Gompel, B. Conings, K. L. Jiménez Monroy, J. D´Haen, K. Gilissen, M. D´Olieslaeger, M. K. Van Bael, and P. Wagner, *Physica Status Solidi A* **210** (2013).
- [170] C. Klingshirn, *Physica Statatus Solidi B* **244**, 3027–3073 (2007).
- [171] M. Nistor, F. Gherendi, N. B. Mandache, C. Herbert, J. Pierriere, and W. Seiler, *Journal of Applied Physics* **106**, art. no. 103710 (2009).
- [172] S. K. Hong, Y. Chen, H. J. Ko, and T. Yao, *Physica Status Solidi B* pp. 803–813 (2002).
- [173] Y. Zhang and W. Wang, *International Journal of Applied Ceramic Technology* **9**, 374–381 (2012).

BIBLIOGRAPHY

- [174] K. F. Cai, E. Müller, C. Drašar, and A. Mrotzek, *Materials Science and Engineering: B* **104**, 45–48 (2003).
- [175] A. Matthiessen and C. Vogt, *Philosophical Transactions of the Royal Society of London*, **154**, 167–200 (1864).
- [176] G. Horowitz and M. E. Hajlaoui, *Synthetic Metals* **122**, 185–189 (2001).
- [177] R. K. Shukla, A. Srivastava, A. Srivastava, and K. C. Dubey, *Journal of Crystal Growth* **294**, 427–431 (2006).
- [178] M. Suche, S. Christoulakis, N. Katsarakis, T. Kitsopoulos, and G. Kiriakidis, *Thin Solid Films* **515**, 6562–6566 (2007).
- [179] R. D. Shannon, *Acta Crystallographica* **A32**, 751–767 (1976).
- [180] M. H. Yoon, S. H. Lee, H. L. Park, H. K. Kim, and M. S. Jang, *Journal of Materials Science Letters* **21**, 1703–1704 (2002).
- [181] K. H. Kim, S. H. Shim, K. B. Shim, K. Niihara, and J. Hojo, *Journal of the American Ceramic Society* **88**, 628–632 (2005).
- [182] T. Tsubota, M. Ohtaki, K. Egushi, and H. Arai, *Journal of Materials Chemistry* **7**, 85–90 (1997).
- [183] J. N. Duenow, T. A. Gessert, D. M. Wood, B. Egaas, R. Noufi, and T. J. Coutts, *Materials Research Society Symposium Proceedings* **1012** (2007).
- [184] X. Zi-Qiang, D. Hong, L. Yan, and C. Hang, *Materials Science in Semiconductor Processing* **9**, 132–135 (2006).
- [185] A. El Manouni, F. J. Manjón, M. Mollar, B. Marí, R. Gómez, M. C. López, and J. R. Ramos-Barrado, *Supperlattices and Microstructures* **39**, 185–192 (2006).
- [186] T. J. Coutts, D. L. Young, and X. Li, *MRS Bulletin* **25**, 58–65 (2000).

BIBLIOGRAPHY

- [187] H. Kim, J. Horowitz, S. B. Qadri, and D. B. Chrisey, *Thin Solid Films* **420-421**, 107–111 (2007).
- [188] G. Luka, L. Wachnicki, B. S. Witkowski, T. A. Krajewski, R. Jakiela, E. Guziewicz, and M. Godlewski, *Materials Science and Engineering B* **176**, 237–241 (2011).
- [189] K. Ellmer and R. Mientus, *Thin Solid Films* **47**, 5829–5835 (2008).
- [190] N. R. Aghamalyan, T. Aslanyan, E. S. Vardanyan, Y. A. Kafadaryan, R. K. Hovsepyan, S. I. Petrosyan, and A. Poghosyan, *Izvestiya NAN Armenii Fizika* pp. 417–426 (2012).
- [191] S. H. Kim, Y. K. Moon, D. Y. Moon, M. S. Hong, Y. J. Jean, and J. W. Parkt, *Journal of the Korean Physical Society* **49**, 1256–1259 (2006).
- [192] B. Oh, M. Jeong, D. S. Kim, W. Lee, and J. Myoung, *Journal of Crystal Growth* **281**, 475–480 (2005).
- [193] H. C. and Y. H. Jeong and C. B. Park, *Transactions on Electrical and Electronic Materials* **10** (2009).
- [194] Y. B. Xiao, S. M. Kong, E. H. Kim, and C. W. Chung, *Solar Energy Materials and Solar Cells* **95**, 264–269 (2011).
- [195] R. V. Muniswami Naidu, A. Subrahmanyam, A. Verger, M. K. Jain, S. V. N. Bhaskara Rao, S. J. Jha, and D. M. Phase, *Electronic Materials Letters* **8**, 457–462 (2012).
- [196] A. K. Das, P. Misra, R. S. Ajimsa, A. Bose, S. C. Joshi, D. M. Phase, and L. M. Kukreja, *Journal of Applied Physics* **112**, 1–6 (2012).
- [197] A. Kelchtermans, *Dissertation (Universiteit Hasselt): Synthesis and in-depth characterization of Al-doped ZnO nanoparticles as building blocks for TCO layers* (2014).
- [198] K. Tarasov and O. Racourt, *Journal of Nanoparticle Research* **13**, 6717–6724 (2011).

BIBLIOGRAPHY

- [199] K.E. Lee, M. Wang, E.J. Kim, and S.H. Hahn, *Current Applied Physics* **9**, 683–687 (2009).
- [200] M. N. Baibich, J. M. Broto, A. Fert, F. N. Vandau, F. Petroff, P. Eitenne, G. Creuzet, A. Friederich, and J. Chazelas, *Physical Review Letters* **61**, 2472–2475 (1988).
- [201] G. Binasch, P. Grünberg, F. Saurenbach, and W. Zinn, *Physical Review B* **39**, 4828–4830 (1989).
- [202] R. von Helmolt, J. Wecker, B. Holzapfel, L. Schultz, and K. Samwer, *Physical Review Letters* **71**, 2331–2333 (1993).
- [203] P. Wagner, I. Gordon, L. Trappeniers, J. Vanacken, F. Herlach, V.V. Moshchalkov, and Y. Bruynseraede, *Physica Review Letters* **81**, 3980–3983 (1998).
- [204] Z. Q. Li, D. X. Zhang, and J. J. Lin, *Journal of Applied Physics* **99** (2006).
- [205] X. D. Liu and E. Y. Jiang, *Solid State Communications* pp. 394–397 (2006).
- [206] M. Gacic, G. Jakob, C. Herbort, H. Adrian, T. Tietze, S. Brück, and E. Goering, *Physical Review B* **75**, art. no. 205206 (2007).
- [207] R. P. Koshla and J. R. Fischer, *Physical Review B* **75**, 4084–4097 (1970).

